Understanding and Optimization of InN and high Indium containing InGaN alloys by Metal Organic Chemical Vapor Deposition

Von der Fakultät für Elektrotechnik und Informationstechnik der Rheinisch-Westfälischen Technischen Hochschule Aachen zur Erlangung des akademischen Grades eines Doktors der Ingenieurswissenschaften genehmigte Dissertation

vorgelegt von

Master of Science in Physik
Öcal Tuna
aus Kars, Türkei

Berichter:
Prof. Dr.-Ing. Michael Heuken
Univ.-Prof. Dr.-Ing. Rainer Waser

Tag der mündlichen Prüfung: 18.07.2013

Contents

1 Introduction

It is hard to imagine the modern electronics such as computer chips, mobile phones, solar cells, light emitting diodes (LEDs) without crystalline semiconductors. Most of the efforts in epitaxial film technology was dedicated in the direction of the II/VI as well as III/V compounds of GaAs and GaP until the breakthrough in GaN based materials discovered by Shuji Nakamura at Nichia Chemical [1, 2, 3]. The discovery dates back to early 1990's and covers the first high brightness blue LEDs and LDs based on Ga-rich InGaN [1]. This technological breakthrough, as well as the less toxic and more abundant properties of III-nitrides compared to GaInAs and GaInP [4, 5, 6], led to considerable scientific research on nitride based semiconductors worldwide. Today, group III-nitride materials are extensively used to produce highly efficient and long lasting LEDs that are indispensable for backlighting in displays, traffic lights, white lighting and photodetectors[7, 8]. Moreover, advanced GaN/$Al_xGa_{1-x}N$ high power microwave transistors are today commercially available [9] and are being applied to low noise amplifiers and RF power control [10]. One of the big advantages of the III-nitrides (GaN, AlN and InN) is that full solar spectrum can be covered through alloying binary materials. The bandgap of GaN lies in the ultraviolet (UV). In order to shift it to the infrared and deep UV ranges one needs to incorporate Indium (In) or Aluminum (Al) in an alloy with GaN. By rising Al or In content in AlGaN or InGaN, respectively, bandgap can be varied in a large range from 0.65 eV (InN) to 6.2 eV (AlN) which can be seen in Fig. 1.1.

Among the III-nitrides semiconductors (Ga,Al,In) N, InN is the most attractive one due to having the narrowest bandgap, the lowest electron effective mass [11] and there-

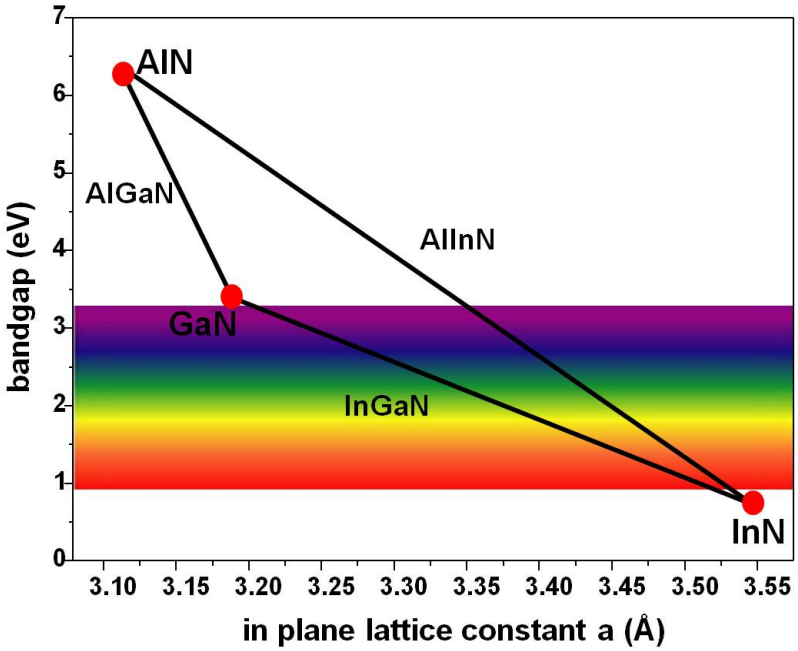

Figure 1.1: Bandgap of binary InN,GaN and AlN and their ternary alloys versus in-plane lattice constants (no bowing assumed).

fore high electron mobilities (μ)[12] and high saturation (drift) velocity (V_{sat}) [13]. Room temperature peak drift velocity was calculated by O'Leary *etal.* and a high peak drift velocity of 6.0x10^7 cm/s for applied electric field of 22.5 kV/cm [14] was obtained. Later on, assuming a doping concentration of $10^{17}cm^{-3}$ and a crystal temperature of 300K, it was shown that transient electron transport occurs in InN based devices with an extremely high speed and with a cut off frequency of 2.5 THz for 0.1 μ thick layers[15]. In the referenced study, it was suggested that InN based HFET (High Field Effect Transistors) can operate at higher microwave frequencies. Moreover, for low doped and dislocation free InN, a maximum room temperature electron mobility of 14000 cm^2/Vs was calculated by Palyakov *etal.* [16]. As a summary, all these results suggest the importance of InN in high current and high frequency applications where high charge carrier and high V_{sat} are desired.

The most drastic breakthrough for InN was the measurement of real bandgap of 0.65 eV [17] instead of previously accepted bandgap value of 1.9 - 2.1 eV [18]. This revision in

bandgap makes the InGaN more important since one can cover the whole solar spectrum by only changing In composition in InGaN layer. Ga-rich InGaN is typically used in blue, green and white LEDs, laser diodes and transistors. Moving to In-rich region in InGaN alloy will bring great advantages as consequence of reducing band gap. By varying the fraction of In, emission in different wavelengths i.e. red, green and blue range, could be achieved from the same material.

Despite these positive properties, InN is the least studied material owing to difficulties of growing high quality single crystalline thin InN films. Many problems of InN and InGaN, associated with structural, optical and electrical properties, are poorly understood and need to be addressed. The large lattice mismatches between InN and InGaN epilayers and any substrate material result in a high density of dislocations. Moreover, as grown InN and In-rich InGaN materials exhibit very high residual background electron concentrations, typically in the range of 10^{18}-10^{21} cm^{-3}. In addition, due to the Fermi level position with respect to charge neutrality layer (CNL), a surface electron accumulation is present near the surface region of both n- and p-type InN and In-rich InGaN alloys. This creates several challenges such as difficulties in the measurement of the type of bulk conductivity and the reliable bulk carrier concentration. Growing In-rich InGaN layers and the formation of phase separation are additional problems that need to be solved. The comparison of quality of InN and InGaN layers grown using the metal organic chemical vapor deposition (MOCVD) and molecular beam epitaxy (MBE) methods indicate that growth with MOCVD is the more challenging method due to the high dissociation temperature of NH_3 with respect to the low decomposition temperature of InN. Relatively high N over pressure and weak bonding energy between In and N are additional problems. However, from the point of view of mass production, MOCVD has huge advantages compared to MBE. Thus, it is essential to be able to grow high quality of these materials by MOCVD.

This study focuses on the detailed investigation of MOCVD growth and optimization of n- and p-type-doped InN and InGaN with different In contents. In chapter 2, the properties and challenges of the growth of InN and In-rich InGaN is summarized. Brief description of the standard characterization techniques and a detailed explanation of the

nonstandard techniques used are given in chapter 3. Chapter 4 focuses on the growth and in-situ and ex-situ characterization results of GaN templates used for the InN and InGaN epitaxy. In chapter 5 the influence of the most important MOCVD growth parameters (such as temperature and V/III ratio) on InN growth is studied. Optimum MOCVD growth conditions with respect to structural, electrical and optical properties are evaluated. Optical methods are considered for the electrical characterization and these methods are proposed so as to avoid the influence of surface carrier accumulation on the electrical characterization results. Chapter 6 covers the growth and study of various In content InGaN layers. Here, a new approach to growing In-rich InGaN layers is proposed. The approach is based on growing a thin InN layer beneath the InGaN layers and enhancing the In concentration by In migration from InN layer to InGaN layer. In addition, a detailed investigation of surface electronic properties is described and a shift in the Fermi level position with respect to the charge neutrality layer at different In contents is shown to be realized. This is followed by chapter 7 which deals with the growth and optimization of Mg-doped In- and Ga-rich InGaN layers. The influence of Mg-doping rate on the change of the conductivity type is studied and required Mg-doping rates for p-type conductivity of InN and InGaN are defined. Finally, chapter 8 summarizes this work.

2 Basics of group III nitride semiconductors and unique properties of InN and InGaN

2.1 Material properties and crystal structure of group III nitrides

The unique properties of group III-nitrides, such as good thermal, mechanical and chemical stability, make them more promising than the other types of semiconductors like Si and GaAs. The nitride semiconductors are found in three different crystal structures, namely wurtzite (hexagonal), zincblende (cubic) and rocksalt. The substrate used defines the type of the crystal structure. Among these, the wurtzite structure is the most thermodynamically stable one. This study focuses on layers with wurtzite structure. The selected properties of group III-nitrides in wurtzite structure and of trigonal sapphire are listed in Table 4.1. The wurtzite crystal structure of group III- nitrides is defined by two independent lattice parameters of 'a' and 'c'. A drawing of the crystal structure of InN is shown in Fig. 2.1. The 'a' is the edge length (in-plane lattice constant) of the basal hexagon which is perpendicular to the crystallographic direction identified by the Miller index (0001) and 'c' is the height of the hexagonal prism (out-of-plane lattice constant) which is parallel to the (0001) direction. The structure consists of two hexagonal close-packed sub-lattices with an ABAB stacking sequence. Each lattice layer is shifted by 5/8 unit cell lengths c with respect to the previous one[19]. The

Table 2.1: Selected material properties of group III nitrides and lattice mismatches of InN with GaN, AlN and Sapphire. a/c lattice parameters, α thermal expansion coefficient, E_g bandgap energy, ρ density, LM lattice mismatch

Properties	Unit	InN[24, 25, 26, 27, 28]	GaN[20, 26, 27, 28]	AlN[29, 26, 27, 28]	Sapphire[29]
a/c (300K)	nm	0.3545/0.5703	0.3189/0.5185	0.3112/0.4982	0.476/1.299
ρ	$g.cm^{-3}$	6.81	6.07	3.29	3.98
$E_g(300K)$	eV	0.64	3.44	6.14	10
Melting point	K	2146	2791	3487	2323
α (a/c) 10^{-6}	K^{-1}	3.82/2.75	3.43/3.24	4.35/3.48	7.3/8.1
LM with InN	%	0	11	14	-25

geometry of the atomic bonding is tetrahedric, i.e. each atom has 4 nearest neighbors of the other atom-type. One of the tetrahedric bonds is parallel to the c-axis and the lattice parameter is defined as u = $(c/a)^2$. For hexagonal InN films; u = 3.77 nm[20] (see Fig. 2.1). The in-plane lattice constants of the group III materials lead to lattice mismatches, the amounts of which are determined by Equ. 2.1

$$Latticemismatch = \frac{a_{film} - a_{substrate}}{a_{substrate}} x100 \tag{2.1}$$

Larger lattice mismatch leads to higher misfit dislocation densities which hamper the growth of high quality layers and reduce the optical and electrical properties[21]. The lattice mismatch between InN and the other group III nitrides (AlN, GaN) and sapphire are listed in Table 2.1. InN has the lowest lattice mismatch of about 11% with GaN. Therefore, all investigated layers were grown on GaN-on-sapphire templates. The growth of epitaxial films is not only suffering from the lattice constant differences, which leads to lattice mismatch between substrates and layers, but also from the mismatch due to the thermal expansion coefficient differences. If the thermal mismatch is too high, the layer will crack during cooling down from high growth temperatures to room temperature[22, 23].

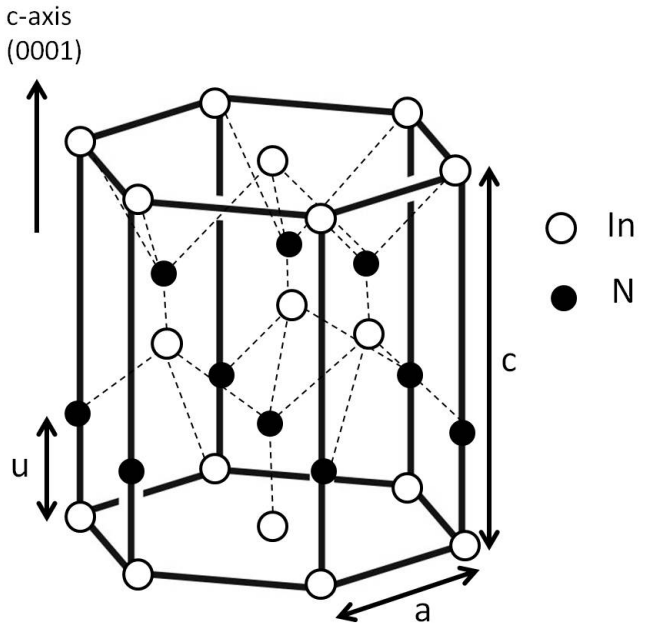

Figure 2.1: Wurtzite structure of InN crystal with its lattice constants 'a' and 'c'. The open spheres are In atoms and the smaller closed spheres indicate N atoms.

2.2 Defects in III-V epitaxy

In epitaxial materials, the position of atoms or molecules are supposed to be repeating with fixed distances determined by the unit cell parameters. However, the arrangement of atoms or molecules in most crystalline materials is not perfect. The regular patterns are interrupted by crystallographic defects. Here possible defects in crystals will be summarized. Defects can be divided into different groups like point, planar, bulk and line defects. Vacany, interstitial and antisite defects are defined as point defects. A schematic illustration of point defects is shown in Fig. 2.2. Vacancy defects are lattice sites which would be occupied in a perfect crystal, but are vacant. Antisites defects are atoms that occupy a site in the crystal at which there is usually not an atom. A nearby pair of a vacancy and an interstitial is often called a Frenkel defect. Antisites occur in an ordered alloy or compound when atoms of different type exchange positions. Complexes can be formed between different kinds of point defects. For example, if a vacancy encounters an impurity, the two may bind together if the impurity is too large

for the lattice. Grain boundaries, which are defined as planar defects, occur where the crystallographic direction of the lattice abruptly changes. This usually occurs when two crystals begin growing separately and then meet. Voids are small regions without atoms and can be thought of as cluster of vacancies and it is in the category of the bulk defects.

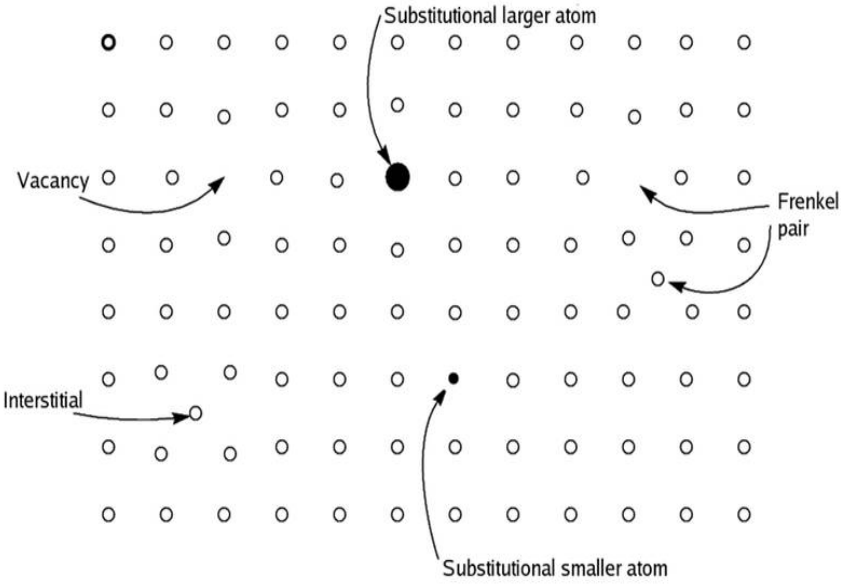

Figure 2.2: A schematic illustration of point defects (After [30]).

The misalignment of atoms in the crystal lattice is called as linear defects/dislocations. There are two important dislocations in this category: edge dislocation and screw dislocation. The mixture of these two dislocations is called a mixed dislocation. These kind of dislocations are generally observed in highly mismatched epitaxial layers. For instance, InN growth on GaN introduces a lattice mismatch of 11% which leads to island-like growth and therefore no coalescence occurs. Due to the island-like nature of the growth, InN crystallites can be misoriented with respect to the underlying GaN. The misorientation occurs in two different ways: tilted and twisted[30]. Tilt can be defined by the crystalline surface normal being non-parallel to the surface normal. Twist is defined by the crystal being rotated in the basal plane relative to the substrate [30, 31]. Tilt and twist are associated with screw- and edge-type dislocations, respectively. Fig. 2.3 displays a drawing of the edge- and the screw-type dislocations. The edge and screw-

type dislocations are characterized by Burgers vectors b, which help to describe the size and the direction of the main lattice distortion caused by a dislocation[32]. The Burgers vector can be found by drawing a loop around the dislocation line and noticing the extra inter atomic spacing needed to close the loop. The Burgers vectors are shown by blue lines in Fig. 2.3. Tilt is identified by dislocation with a Burgers vector out of the basal plane and it results in a screw component threatening dislocations. The strain fields from these dislocations distort the on-axis planes and therefore broaden on-axis (0002) rocking curve measurements. Conversely, twist in the InN mosaic is formed with dislocations exhibiting Burgers vector in the basal plane[32]. Pure edge-type threading dislocations fall in this category. The off-axis planes are disrupted by edge-type dislocations and FWHM of off-axis rocking curves, such as (10-12) and (30-32), are broadened by the presence of such dislocations[32, 30].

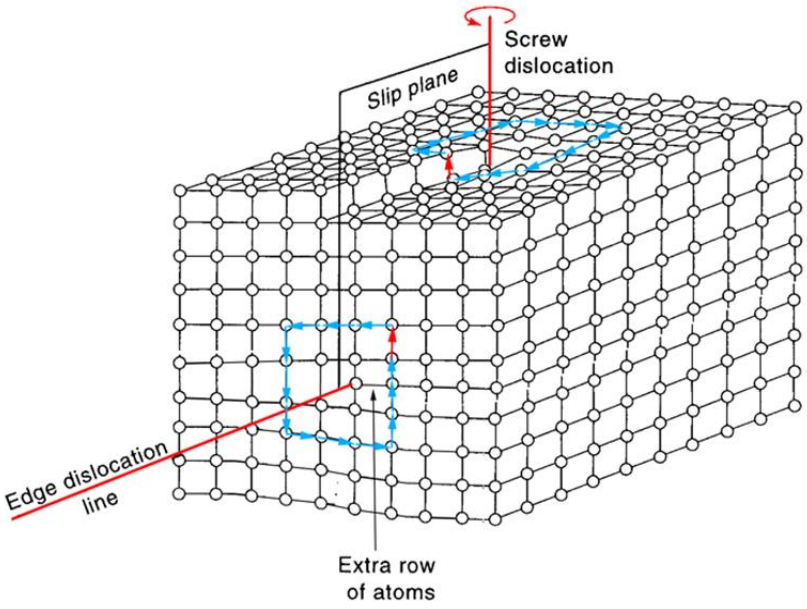

Figure 2.3: A schematic of the edge and the screw dislocations. Blue lines show Burgers vector [after[33]].

2.3 Unique properties of InN

2.3.1 Revision of optical bandgap energy of InN

Early studies of InN growth by reactive sputtering yielded polycrystalline films with bandgap energies about 1.9-2.0 eV [34, 35, 36, 37]. Optical absorption measurements were performed on polycrystalline InN, GaN and InGaN alloys grown by electron beam plasma technique by Osamura *et al.*[36, 37]. A large bandgap about 1.95 eV was reported for InN. In addition, InN grown by radio frequency (RF) sputtering was extensively studied by Tansley, Foley *et al.*[17, 38, 39, 40, 41]. The highest room temperature electron mobility of 2700 cm^2/Vs with a lowest electron concentration of $5x10^{16}$ cm^{-3} and a bandgap in the range of 1.9 eV was reported by authors. However, these state-of-the-art electrical results could not be reproduced[42]. On the other hand, many other investigations revealed that the polycrystalline InN films have very low electron mobility of less than 100 cm^2/Vs with a very high background carrier concentrations in the range of 10^{19}-10^{21} cm^{-3} [17, 43]. The large bandgap of 1.9 eV had been accepted for a long time and referred as the bandgap of InN until single crystalline high-quality InN films were grown by more sophisticated techniques like MBE and MOCVD[44, 45, 46, 47, 48, 49, 50]. The first evidence of the narrow bandgap was reported by Inushima et al.[49]. The InN layers were grown by MBE and it was demonstrated that the fundamental absorption edge of the InN layers was about 1 eV[49]. After this breakthrough, the small bandgap of InN (smaller than 1 eV and even as small as 0.64 eV) was reinforced by other researchers[50, 51, 52, 53]. By using various characterization techniques like optical absorption, photoluminescence and PLE spectroscopy, the bandgap of MBE grown InN was reported as 0.9 eV[46]. In order to further confirm the small bandgap and to figure out the influence of In, InGaN alloy with different In contents were grown. A decrease in bandgap with increasing In content in InGaN was realized. A bandgap of 0.7 eV was obtained for InN[51]. At the moment, the available state of the art (to the best of the knowledge of the author) MBE-grown undoped InN has a bandgap of 0.64 eV at room temperature. An electron concentration in the low 10^{17} cm^3 range and a mobility as high as 2250 cm^2/Vs were measured using the Hall effect technique[52, 53].

After an extensive research on the optical properties of InN, the previously reported large bandgap was revealed to be wrong. This lead to the question of why the polycrystalline InN layers showed a bandgap in the range of 1.9-2.1 eV. In highly degenerate structures, the state filling from the bottom of the conduction band to higher energies, known as Burstein-Moss shift which prevents the measurement of actual bandgap of the material, has been proposed as the reason of the measured large bandgap of InN[54, 55]. Burstein-Moss effect states that degenerate carrier concentration results in occupied states from the bottom of the conduction band to larger energies, which is preventing the optical transition from the bottom of the conduction band to the top of the valance band[48, 54]. The first thing that comes to mind as a reason of the large bandgap value measured is oxygen atoms contaminating the InN layers during sputtering growth and thus behaving as donors. Oxygen atoms donate their electrons and as a consequence of Burstein-Moss shift[56] the bandgap increases. However, it was also reported that even though there is a wide range variation of carrier concentration 10^{16}-10^{21} cm^{-3} as shown in Fig. 2.4[50, 57, 58], polycrystalline InN layers yielded a large bandgap of about 2 eV. Figure 2.4 contains results of the single crystalline InN films showing bandgap values of mainly less than 1 eV and the bandgap has a remarkable dependence on the carrier concentration. Comparing the discussions, it can be inferred that the single crystalline and the polycrystalline films have very different natures. Davydow et al.[51] have annealed InN layers in oxygen atmosphere in order to figure out the influence of oxygen on InN bandgap. The authors stated that annealing the InN layers in oxygen atmosphere leads to formation of optically transparent alloys of InN-In_2O_3.With about 20% oxygen concentration, the bandgap of those alloys reach approximately 2 eV[51]. The evidence suggests that in addition to the Burstein-Moss shift, the formation of oxinitrides, which have larger bandgap than InN, might be a reason of the larger bandgap of polycrystalline InN[51].

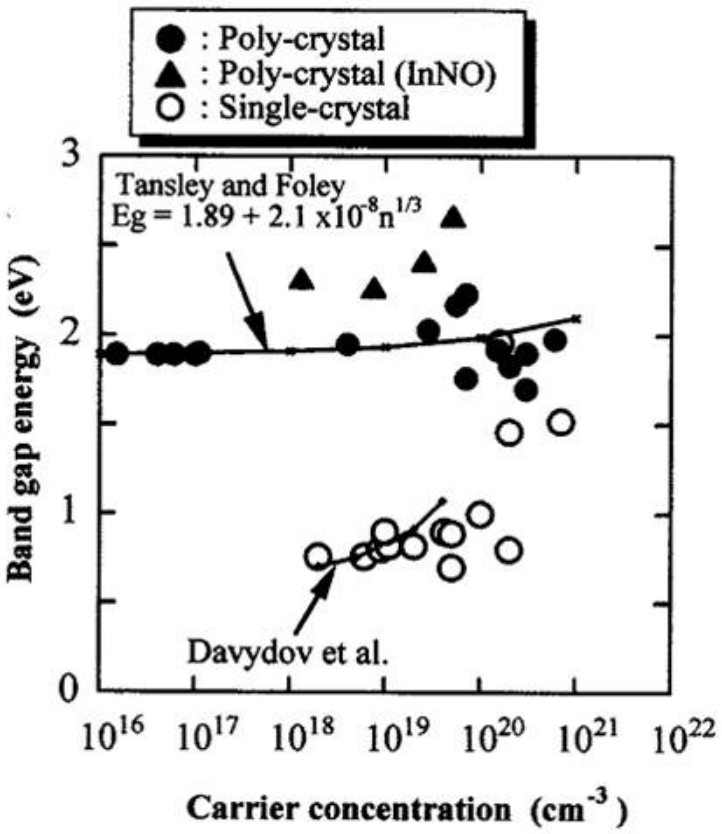

Figure 2.4: Bandgap energy of InN versus carrier concentration [after[50]].

2.3.2 Narrow bandgap energy and high electron affinity

The bandgap is defined as the smallest separation between the valence band maximum and the conduction band minimum. It is known that InN has a direct bandgap which means there is no separation in momentum space between the valence band maximum and the conduction band minimum [52]. MBE grown high-quality InN has a bandgap of 0.64 eV and an intrinsic electron concentration of about $3x10^{17}$ cm^{-3}[52, 53]. The narrow bandgap of InN is explained based on the interaction between orbitals of In and N atoms[59]. Figure 2.5a shows conduction and valance band energies of III-N and In-V compounds with respect to charge neutrality layer. b shows atomic orbital energies for constituent cations and anions[59]. Very small difference between the cation p orbitals makes the interaction between the cation d orbitals and the N 2p orbital a

dominant factor in determining the valance band variation in the III-Ns (see Fig. 2.5b). The interaction has been modeled by the tight biding model[60, 61]. The model states that the shift in valance band maximum on moving from AlN to InN is a consequence of p-d repulsion between 2p-valance band states and the shallow In 4d orbital. The shift of the valance band of GaN as compared with AlN indicates the influence of the p-d repulsion. The repulsion is stronger for InN and therefore a larger shift in valance band of InN is observed. This is due to the larger separation between Ga 3d and N 2p orbitals. Since Al has no occupied d-levels, there is no p-d repulsion pushing the VBM to higher energies[59, 62]. The variation in CBM of the III-Ns is explained with the anti-bonding state of the cation s-orbitals and N 2s-orbitals[61]. Due to the small variation in s-energies of III-V compounds (Al, Ga and In), the energy of the N 2s state and its weight in the CBM are dominating the level of conduction band minimum (CBM). As shown in Fig. 2.5b, the N 2s orbital energy (-18.5 eV) is much lower than the s orbital energies of any other elements. This is the main reason of the exceptionally low CBM in InN. Fig. 2.5c shows the variation of the band gap energies of the direct bandgap semiconductors. One can deduce from the image that the bandgap energy of InN is decreasing with decreasing the period of anions. This leads to the breakdown of the common-cation rule which states that for isovalent, common-cation (anion) semiconductors, the direct gap at the Γ-point increases as the anion (cation) atomic number decreases[63, 26].

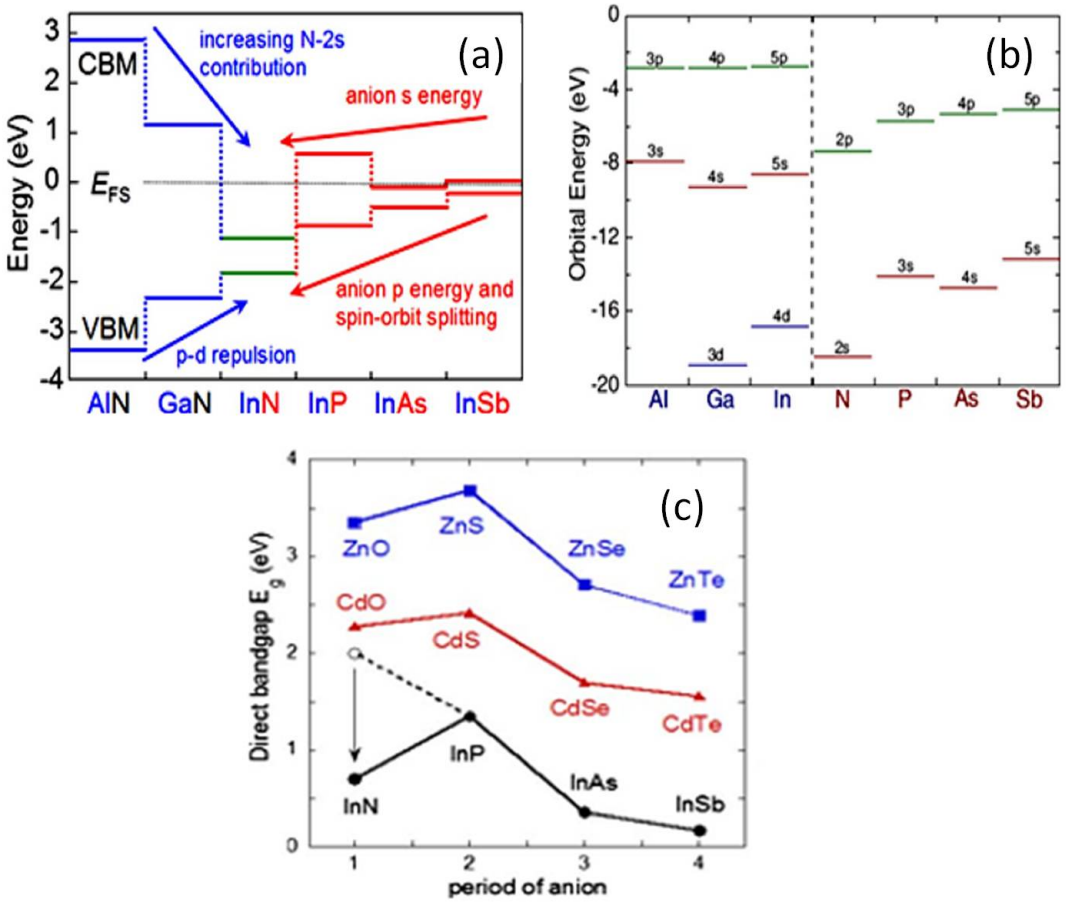

Figure 2.5: a) Atomic orbital energies of group III and V elements. b) Conduction and valance band edges of related group III-V semiconductors with respect to E_{FS}. c) The breakdown of the common-cation rule in Zn-VI, Cd-VI and In-V semiconductors. (Adapted from[59])

The very low conduction band minimum energy in InN causes not only the narrow bandgap but also the extraordinarily high electron affinity of the InN. Electron affinity is the energy difference between the conduction band minimum and the vacuum level. InN has the largest electron affinity (5.5-5.8 eV) in all group III-V semiconductors[64, 65, 66, 67]. For instance, the electron affinities for GaN and AlN are 4.1 eV[68] and 0.6 eV[69], respectively. The unique properties of InN, like low conduction band minimum and consequently very large electron affinity impact directly the electronegativity (acceptor) or the electropositivity (donor) of the native defects in InN. This property can be

understood within the Amphoteric Defect Model (ADM) developed by Walukiewicz et al.[70, 71]. The theory states that the energies of the defects are not sensitive to the locations of the valance and the conduction bands but thay rather are defined relative to the vacuum level. In addition, defects are able to behave either as donors or as acceptors depending on the surface Fermi energy (E_{sF}). In other words, an energy transformation from donor (acceptor) to acceptor (donor) takes place depending on the surface Fermi energy position E_{sF} with respect to the charge neutrality level (E_{CNL})[72, 73]. E_{CNL} indicates the energy level at which the formation energies of donors and acceptors are equal. E_{CNL} is also defined as the Fermi level stabilization energy (E_{FS})[70, 72] and branch point energy[59, 63, 74, 75, 76]. The charge neutrality level is found by taking a weight average of the conduction and valence band over all of k-space[77, 78]. For GaN and AlN, the E_{CNL} lies in the gap, but for InN, due to the very low conduction band minimum energy, it is above the conduction band[77]. The E_{CNL} energy in the InN is about 1.2 eV[59] above the conduction band minimum (CBM) as demonstrated in Fig. 2.6a. According to the ADM, if the surface Fermi energy level is greater than the charge neutrality level ($E_{sF} > E_{CNL}$) the native defects behave as acceptors. If, on the other hand, $E_{sF} < E_{CNL}$ is true, the native defects behave as donors. In other words, for $E_{sF}>E_{CNL}$ ($E_{sF}<E_{CNL}$) the formation energy of native acceptor (donor) defects is lower than that of donor (acceptor) formation energy[70, 71]. For the case of InN, as shown in Fig. 2.6a, the E_{CNL} position is above the E_{sF} level which means that the formation energy of donor-type native defects is lower i.e. any defect (or donor-type surface states) emit their electron into the conduction band. Therefore, a number of donor-type surface states will be unoccupied, and hence positively charged[76, 79, 80, 81, 82]. In order to maintain charge neutrality, the band near the surface bends and an equal amount of negative charge accumulates on the surface (see Fig. 2.6b). This behavior is a consequence of the intrinsic properties of the semiconductor. All semiconductors tend to be electrically neutral if there is no external field applied[82]. Therefore, semiconductors with surface accumulation or depletion layers compensate by forming equal opposite charges within near-surface region, called the surface space charge region. The surface space charge region forms by band bending

within the surface.

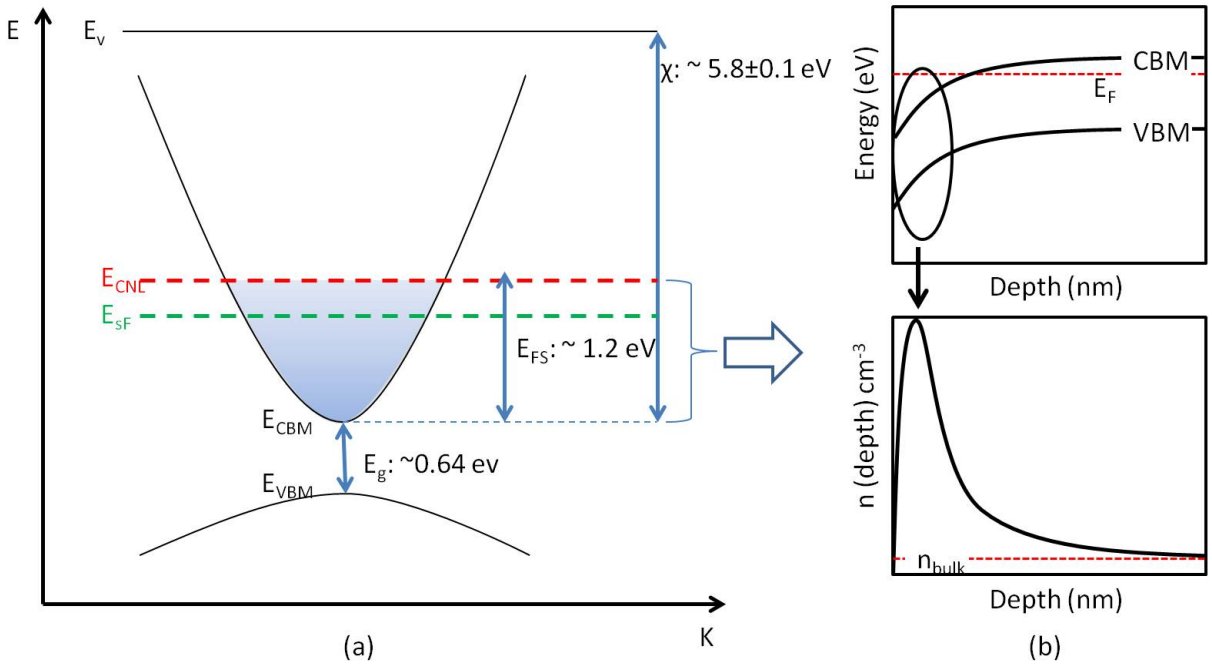

Figure 2.6: A schematic representation of a) CBM, VBM, E_{CNL} and E_{sF} energy levels of InN with respect to Vacuum level (E_v). b) Band bending and corresponding surface electron accumulation within the surface of InN.

Here, band bending phenomenon is described for n-type semiconductors and systematically shown in Fig. 2.7. In the case of n-type materials, when the surface states are negatively charged, a positive space-charge region is therefore required to maintain charge neutrality. This is achieved by an upward bending of the bands in order to decrease the electron concentration at the surface with respect to the bulk values, resulting in depletion of electrons at the surface. If there are a sufficient number of negatively charged surface states, the band bending required to maintain charge neutrality can be so severe that the Fermi level at the surface moves below the middle of the direct band gap and a p-type surface layer of holes forms which is separated from the n-type bulk region by a depletion layer. This is termed as an inversion layer. In the situation where the Fermi level at the surface is located exactly at the CNL, there are on average no charged surface states, and so there is no band bending. This is referred to as the

flat-band case[83].

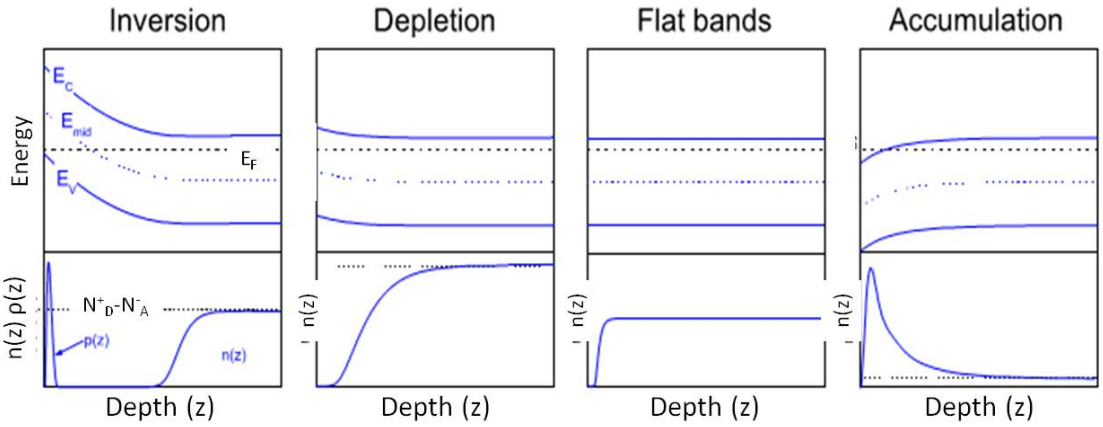

Figure 2.7: Band bending and surface space charge profiles for inversion, depletion, flat-bands and accumulation layers (Figure adopted from [83]).

2.4 Unintentional background carrier concentration in InN

The possible defects and sources contributing to the high surface electron accumulation and high background electron concentration will be discussed below. As mentioned, due to the very low CBM energy and pinning of the CNL in the conduction band, any native point defect tends to behave as a donor, resulting in a high carrier concentration. Because of this property, the structural quality of InN, which is influenced by the point defects, is very critical for the carrier concentration. In addition to the point defects, there are many other origins which have been proposed as donors leading to an increase in carrier concentration[84, 85, 86, 87, 88, 89, 90, 91, 74, 92, 93, 94, 95, 96, 97]. Stamplf et al.[84] performed first-principles density-functional calculation and realized that Oxygen (O) has the lowest energy in n-type InN. Therefore, O, which occupies the N site (O_N), is believed to be an important source of the high background carrier concentration in InN. This result was experimentally supported by Masahiro et al.[85]. Some polycrystalline InN layers were grown on quartz and glassy carbon by MBE and an O concentration in the range of 1-6% was measured. The authors realized that the increase in O concentration from 1% to 6% leading to an increase of optical bandgap from 1.55 to 2.27 eV and claimed that InN with 1.9 eV consists of 3% O in the layer.

Anderson et al.[86] asserted based on first-principle calculations that hydrogen (H) is the main source of the high background carrier concentration in InN. It was found out that H behaves as a shallow single donor when it is interstitial or as a double donor when it substitutes N atoms (H_N). As an interstitial impurity in InN, H strongly bonds to N, causing a breaking (or at least weakening) of an In-N chemical bond[98]. Similar theoretical results were achieved by Limpijumnong et al. [87]. Some experimental findings reinforced this evidence[88, 89, 90, 91]. For instance, Pettinari et al.[90] have extensively studied the influence of H on the carrier concentration of InN by exposing InN layers to H and annealing them in vacuum afterwards. After thermal annealing, a decrease in the carrier concentration to the similar value observed for the as-grown sample suggests the existence of H related donor species. This is contradictory to the behavior of H in AlN and GaN. As known, H is stable as a donor in p-type and as an acceptor in n-type materials and always decreasing the prevailing conductivity[26, 74]. Wu et al. argued, based on the Hall effect and Secondary Ion Mass Spectroscopy (SIMS) measurement results, that H and O alone cannot fully account for the free electron concentration in unintentionally n-type InN[92]. InN layers with different carrier concentrations in the range of 10^{17}-10^{20} cm^{-3} were investigated by Wu et al.[92] H and O concentrations , which were measured by SIMS, are in the range of 10^{18} cm^{-3}. It was discussed by authors that the low values of H and O impurities cannot be the only reason of the carrier concentration of mid 10^{20} cm^{-3}. Therefore, the role of native defects[93, 94] and N[95, 96, 97, 99, 100] as well as In[101] vacancies have a significant effect on the high background carrier concentration. Tuomisto et al.[101] recently proved that In vacancies, which act as acceptors in InN, have tendencies to form complexes with donor-type defects on the N sublattice, such as O_N or N vacancy (V_N) and have an indirect contribution to the carrier concentration[98]. As will be shown in this study, low temperature growth of InN promotes the formation of N vacancies which are forming complexes with In vacancies. Due to the energy level of the complexes with respect to CNL, they are behaving as donors and increase the carrier concentration in InN layer. Tansley and Foley also speculated that the N vacancy might be the defect responsible for natural n-type character of InN[99, 42]. According to their study, both experiment and theory, pointed to a triplet

of donor states associated with the nitrogen vacancy. Some other basic growth studies for example, a study on MOCVD grown InN grown with increasing NH_3/TMIn molar ratio and another one with enhanced NH_3 decomposition at high temperature results in lower electron concentrations and higher mobility, reinforcing the idea that N vacancies are the main reason of the high background electron concentration in InN[83, 99, 95]. Stampfl et al.[84] reported that the nitrogen vacancy is found to be the lowest energy native defect in InN, acting as a potential source of compensation in p-type material. In addition to the possible donors mentioned above, extended defects such as dislocations have been proposed as significant donors[93, 94, 102, 103, 104, 105, 106]. Piber et al.[93] measured and simulated the film thickness dependence of carrier concentration of high quality InN films grown by MBE. Their model is based on the following assumptions: a homogeneous background of donor impurities, a constant surface sheet density due to surface accumulation and dislocations whose density declines exponentially away from the InN/buffer layer interface. The results are schematically shown in Fig. 2.8. The first assumption for the simulation/calculation was that the dislocations do not contribute to the free-electron density and only the combination of background donors from impurities and the extreme electron accumulation at InN surfaces were considered (Fig. 2.8 dashed line). It was found out that the impact of those two parameters was insufficient to reproduce the measured film thickness dependence of the free-electron density measured by Hall effect (Fig. 2.8 scattered circle symbols). However, when dislocations surrounded by positively charged nitrogen vacancies (V_{N+}) were also included in to the model, an agreement was obtained between the calculated and experimental thickness dependence of the free-electron concentration (solid line in Fig. 2.8). The Inset in Fig. 2.8 shows the contribution of regions on the carrier concentration of InN, which will be discussed later in this section. Moreover, Takei et al.[102] employed first-principles calculations to investigate the electronic structure of edge type dislocations in InN. It was found that dangling-bond states of In atoms localized in the dislocation core are located above the conduction-band bottom and thus supply electron carriers to the conduction band of bulk InN. These results were also experimentally supported. For instance, Wang et al.[103] observed a decrease in carrier concentration with decreasing

edge dislocation density. Lebedev et al.[105] reported that crystal defects have a strong effect on the electron concentration and mobility of the carriers.

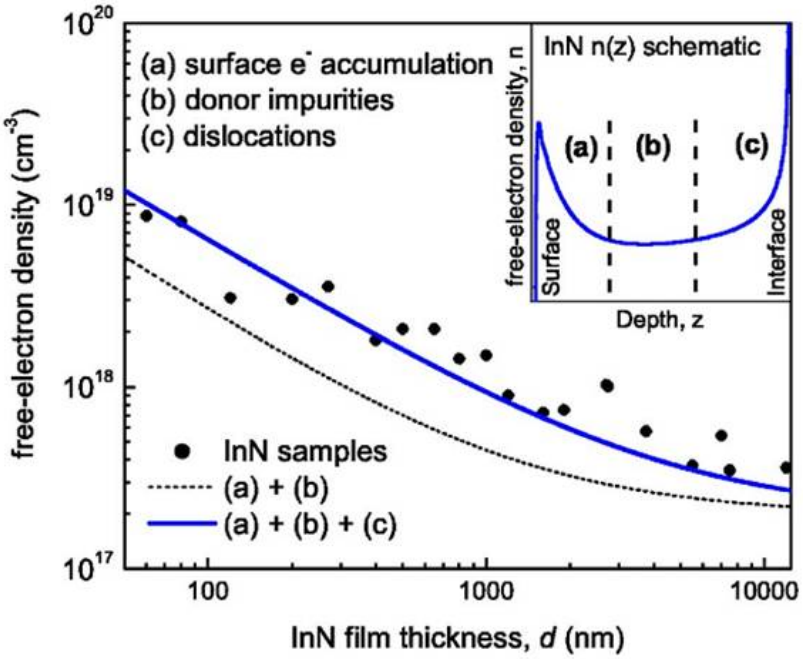

Figure 2.8: Free-electron density in InN as a function of film thickness. Dots show the experimental results. Dashed and solid blue lines show results of modeling. Dashed curve includes background electron density due to impurities and surface e- accumulation. Blue solid line is similar with dashed one but additionally free electrons from positively charged dislocations were included. The inset illustrates the inhomogeneous electron distribution through the InN layer. Figure adapted from ref.[93]

After summarizing the donor sources in InN, it is worth clarifying the effects of the different regions, namely the surface, bulk and interface regions of the buffer, on the carrier density in InN. The theoretical explanation of the existence of the surface electron accumulation was already given. Experimentally, large electron accumulation was demonstrated by Mahboob et al. by high resolution electron energy loss (HREEL) spectroscopy[76]. Authors observed a 40 meV shift on plasmon peak position to lower frequencies as the energy of the probing electrons was increased from 15 to 60 eV. This

is a direct consequence of higher surface plasmon frequency and hence evidence for the existence of an electron accumulation layer at the InN surface. Due to the surface accumulation, electron density as high as 10^{20} cm^{-3} occurs on the surface[81, 107]. Based on the Thomas-Fermi screening length[62], the electron accumulates within the less than 10 nm from the surface. Considering these realities it can be inferred that the measured conductivity is mainly affected by the surface accumulation. Therefore, in order to avoid this effect, the measurement method used to determine the carrier density in these kind of materials is important. The wide area between the surface and the interface can be called as bulk [see Fig. 2.9]. Defects and/or impurities, which are supposed to be uniformly distributed through the InN, are the donor sources in this region. The third region contributing to the carrier density is interface between InN layer and buffer layer. Due to the large lattice mismatches of InN with buffer layers, a very high density of dislocations form at the interface as a result of strain relaxation. As explained before, the dislocations behave as donor and contribute to the conductivity. The dislocation density is exponentially declining by going away from interface and consequently the carrier density is decreasing. The influence of regions (surface, bulk and interface) on carrier density is schmatically demonstrated in Fig. 2.9.

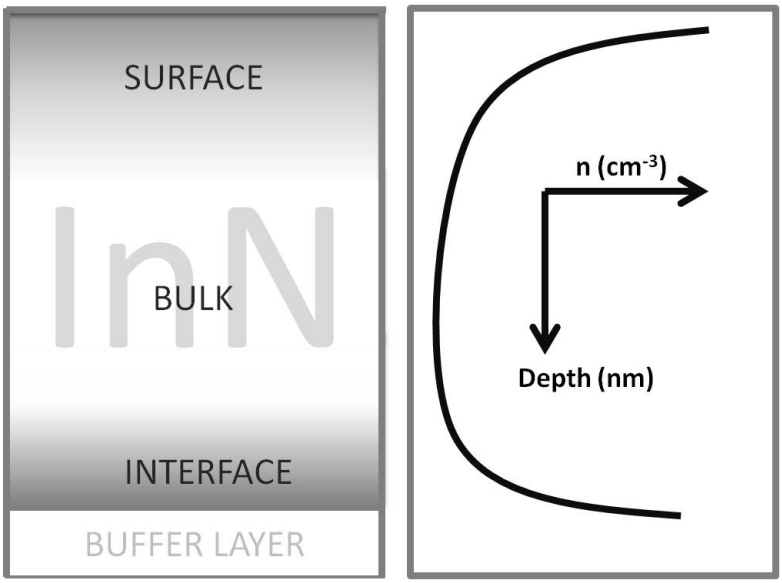

Figure 2.9: Schematic illustration of the influence of different regions in the film on the carrier density.

2.5 Challenges for MOCVD growth of InN and In-rich InGaN layers

Among the III-nitrides, the growth of InN is the most challenging due to several reasons which will be explained below. First, very high equilibrium vapor pressure of nitrogen over InN, which is several orders higher than either GaN or AlN [58], requires growing InN at low temperatures. Figure 2.10 demonstrates the equilibrium N_2 pressure over nitrides (AlN, GaN and InN) and their melting points[108]. At 1 bar InN start dissociation at about 550 ^{o}C while AlN and GaN are thermodynamically stable until temperatures of 1000 ^{o}C and 2300 ^{o}C, respectively. This sets an upper limit for the growth of the InN[20]. It has been shown by several authors that the growth temperature region of InN is in between 500 ^{o}C - 650 ^{o}C[50, 100, 109]. At lower and higher temperatures the growth is facing different problems. The big issue is the temperature stability of NH_3. At low temperatures the decomposition of NH_3 is limited and therefore the growth is suffering from lack of reactive N atoms in the reactor[110]. As a consequence, In droplets are forming on the surface[110]. The shortage of the reactive N atoms causes not only the formation of In droplets on the surface but also some other problems in the growth kinetics and the film properties, such as low growth rate, high background carrier concentration due to N vacancies, low mobility and reduced optical efficiency[101]. In addition, due to the reduced migration of deposited materials at low temperature, the crystal quality of InN decreases, which influences all of the other material properties of InN[107]. On the other hand, even though high growth temperature would enhance the decomposition of NH_3, it also brings some challenges in InN growth. For instance, at high temperatures InN decomposes easily due to the very low In-N-bonding energy. Moreover, H, which forms as a consequence of NH_3 decomposition, etches InN[111, 112]. The thermodynamic role of H in InN was studied by Koukitu et al.[111]. It was found out that H in the growth system results in a decrease in the InN deposition rate. The restricted growth temperature region makes the other MOCVD growth parameters like V/III and growth pressure important. A high input V/III ratio is thought to be a solution to overcome the lack of reactive N atoms [113], enhance the

growth rate and avoid the In droplets on the surface. However, one should keep in mind that, if high V/III ratio is used at high growth temperature region, the growth would be limited by H etching. Therefore, it is suggested that the high V/III ratio should be used at low/middle growth temperature of InN[114]. The influence of the growth pressure on InN growth has not been studied in detail yet. However, it is believed to be a critical parameter as well[50]. At high growth pressure, as an outcome of the reduced distance between the molecules and therefore scattering rate is increasing. This leads to an increase in NH_3 decomposition and therefore in the amount of reactive N atoms in the reactor. In addition, at high growth pressures, N dissociation from the layer can be suppressed[115].

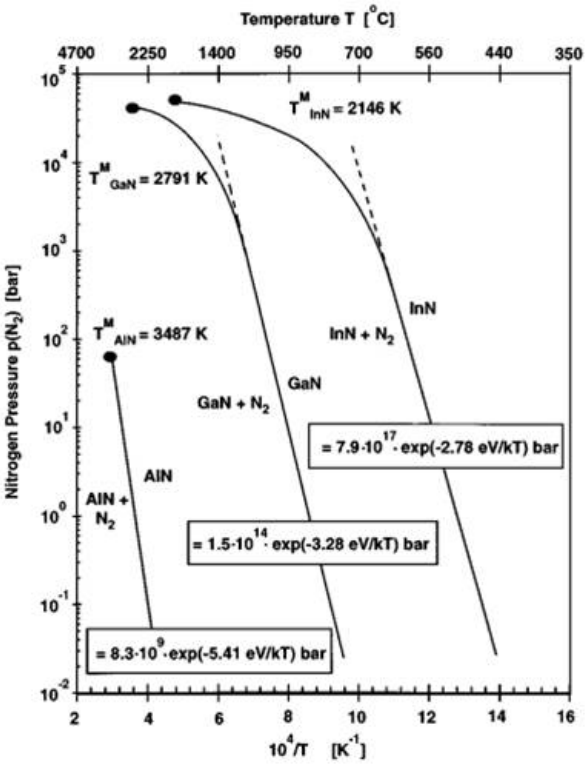

Figure 2.10: Equilibrium N_2 pressure over InN, GaN and AlN and melting points T^m (Adapted from ref.[108]).

The main challenge of the $In_xGa_{1-x}N$ growth is the solid phase miscibility gap caused by the large inter atomic spacing between InN and GaN[116]. The temperature de-

pendence of the binodal and spinodal lines in the InGaN system was calculated by Stringfellow et al. The resulting image is shown in Fig. 2.11[116]. The binodal line is the boundary between the set of conditions in which it is thermodynamically favorable for the system to be fully mixed and the set of conditions in which it is thermodynamically favorable for it to phase separate. The region under the spinodal line consists solution of two or more components can separate into distinct regions (or phases) with distinctly different chemical compositions and physical properties. At a growth temperature of 800 ^{o}C, the solubility of In in GaN was found to be less than 6%. If LED in the green, yellow and red range of the spectrums and solar cell spectrum are considered, one can easily deduce that the phase separation in InGaN might be a significant problem. Some data points shown in Fig. 2.11 are from MBE grown In-rich InGaN layers studied by Weber et al.[117]. All $In_xGa_{1-x}N$ layers (X_{In}: 0.34-0.78) lie within the miscibility gap calculated by Stringfellow et al.[116]. This indicates the existence of two different phases in InGaN layers. The second issue with InGaN is to grow In-rich layers. There are some attempts to enhance the In incorporation. The easiest way is to decrease the growth temperature but at the cost of lesser crystal quality of the InGaN. The second way, which is proposed by the authors, is to insert a thin InN interlayer beneath the InGaN. The results of this approach will be discussed in chapter 6. InGaN layers with about or less than 20% In are pseudomorphically strained to the underlying layer[118]. It was argued that biaxial strain helps to avoid the formation of phase separation. However, over a critical thickness where the layer starts to relax, phase separation occured[119, 120].

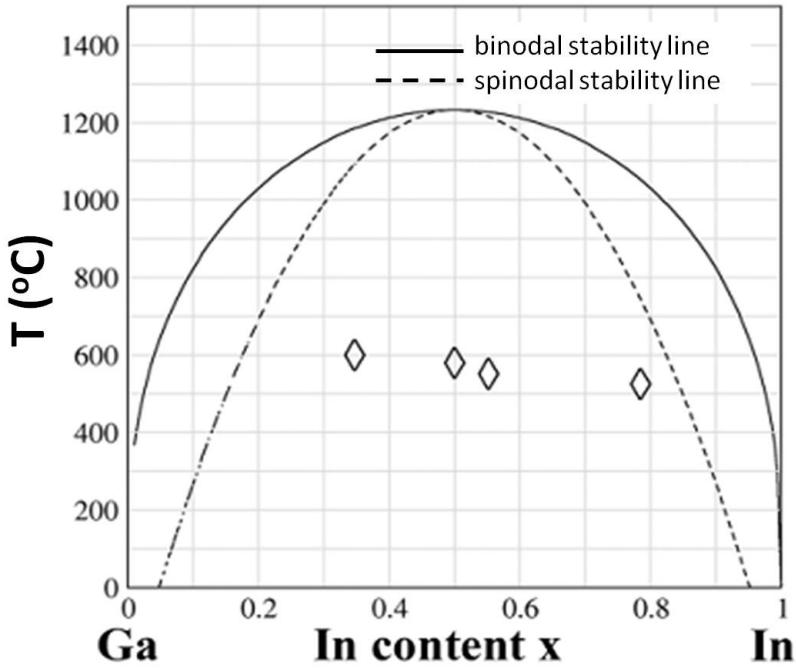

Figure 2.11: Binodal (solid) and spinodal (dashed) curves for the $In_xGa_{1-x}N$ (after Stringfellow et al.[116] and Weber et al.[117]).

2.6 The difficulties of p-type doping and electrical characterization of InN and In-rich InGaN

Realization of p-type materials is very important due to the requirements of p-n junctions for many applications in semiconductor technology. The tendency of being either n- or p-type doping in semiconductor is judged by examining the positions of charge neutrality level (E_{CNL}) and surface Fermi level (E_{sF}) with respect to conduction and valance band positions[121]. By considering the Amphoteric Defect Model (ADM) discussed before, defects and impurities can either be a donor or an acceptor, depending on the location below or above the E_{CNL}, respectively[70, 71, 72, 73]. Since the E_{CNL} for GaN is below the E_{sF}, surface states behave as acceptors. Thus, the realization of p-type GaN is not very difficult but achieving very high hole concentration in GaN is challenging due to the strong binding energy of holes in GaN[122, 123]. In the case of InN and In-rich InGaN, realization of p-type is more difficult because of the surface accu-

mulation layer and the high background electron concentration. In order to compensate the high background electron concentration, a large amount of Mg acceptors is needed during growth. The Mg atoms either sit on the In places or behave as intersitial in the crystal leading to a decrease in the quality of the layer. Moreover, it is known for highly Mg-doped GaN that an excess of Mg atoms produces deep donors and consequently reduce the free hole concentration[124, 125, 126]. This result has been attributed to the formation of compensating defect complexes like Mg-V_N[124, 125, 126]. Therefore, a careful optimization of the growth parameters, especially the Mg/III ratio, is required for achieving and controlling p-type conductivity. All of this makes the growth process very difficult, but the difficulties do not end there. The determination of the type of conductivity of Mg-doped InN and In-rich InGaN is very challenging. Due to the surface electron accumulation, with conventional single field Hall effect measurements, one can only measure negative conductivity even if the layer is doped with Mg acceptors and consists of a p-type layer buried underneath the surface accumulation[127]. The basic idea of the Hall measurement is that a current must be applied through a material perpendicular to the magnetic field and the sign of the potential in the third perpendicular direction gives an idea about the majority carrier type[128]. For Mg doped InN, it is believed that there is a p-type buried layer beneath the surface inversion layer. Due to the electron inversion and the p-type buried layer, an insulating depletion layer is believed to form in between those two layers. This insulating layer forms a large barrier for the electric field to go through the bulk layer and measure the conductivity type by Hall effect[129]. Another method which has been used in literature is the variable field Hall effect measurement[130, 131]. With this technique, a variable magnetic field up to 1000 Tesla can be applied for the Hall measurement[130]. The capability to measure the carriers with low mobility is the basic idea behind this technique. The importance of the method can be understood if one considers the mass of the hole which is about 10 times larger than the mass of the electron[131]. The authors have used the variable field Hall effect method, but they have not considered the existence of an insulating layer between the surface accumulation layer and the bulk. It is clear that there are two different approaches to the carrier mechanism in InN and In-rich InGaN. The reliability

of these approaches are still under debate. The third method is the C-V measurement. Using this technique an electrolyte is used as a contact material instead of metal contacts. Since the C-V measurement is a common method for the characterization of materials with an inversion layer, it can successfully be applied to InN and In-rich InGaN[90, 95, 102, 103, 104]. Details of the C-V technique will be explained in chapter 3 section 3.3.2 and the experimental results will be analyzed in chapter 7.

3 Epitaxial growth technique and methods of characterization

This chapter focuses on the brief description of the epitaxial growth technique and the characterization and calculation methods which were used during this study. Since many characterization techniques were employed, detailed explanation will be given only for non-standard techniques.

3.1 MOCVD and In-situ characterization

All epilayers investigated in this study were grown in an AIXTRON 3x2" Close-Coupled-Showerhead (CCS) reactor. The system is equipped with a 3x2" or a 1x4" susceptor namely; the deposition can be performed on three times two inch (3x2") substrates or one time four inch (1x4") substrate in the same run. As substrates, 2" GaN-on-sapphire templates were used. The deposition system is equipped with in-situ characterization tools which are LayTec EpiTT-Curve and Argus. With a LayTec tool, the reflectance as well as surface temperature was recorded. For the reflectance measurements, the in-situ tool is equipped with two light sources with the wavelengths (λ) of 405 nm and 950.4 nm. The basic working principle is based on the interaction of the light with the growing films. Depending on the transparancy of the film at the wavelength of the incoming light, light can either be absorbed or partly reflected by the films. If the growing film is transparent (at least partly transparent) at the wevelength of the incoming light, when the light of a certain wavelength strikes the layer, one part of the light reflected at the

surface, another part penetrates into the layer. The penetrated part of the light will partly be reflected at the interface between layer and substrate. The reflected beam will travel back to the layer surface and partly will be reflected and partly leave the sample and so on. At the end of this repeating transmission and reflection process, the overall intensity of the reflected light is given by superposition of all reflected beams. Depending of the phase difference between the reflected beams, constructive or destructive interferences will occur. This, therefore, is leading to an intensity modulation of the reflected light, which is so called Fabry-perot oscillations. The phase difference and thus the intensity of the reflected light depends on the thinkness of the growing layer as well as on the optical contants of a material and the wavelength of the light. If the phase difference between two beams is equal to an even number of the half wavelength, constructive interferences and therefore, a maximum reflectence forms. For the destructive interferences, a minumum reflectence occur when the phase difference is equal to an odd number of the half wavelength. For the surface temperature measurement, pyrometry, which measures directly on the wafer surface on the growing layer, is used. The method is based on the fact that at any temperature above absolute zero all bodies emit electromagnetic radiation, the so-called thermal radiation. Therefore it should be possible to derive the temperature of a body by measuring the intensity of this radiation. In order to determine the temperature of a body from its incandescence intensity, the emissivity has to be known. In addition, especially in heteroepitaxy, the emissivity changes during processing. Therefore, a simultaneous measurement of the reflectivity of the sample is indispensable to perform the correct measurement. for further information see ref.[132]. The data from these measurements are measured by a photo diode. The data, which is achieved via the photo-diodes, are collected by a computer and using a material database, output curves consisting of Fabri-Perot oscillations and temperature, were achieved. The resulting curves are called in-situ characterization results. The period of the Fabry-Perot oscillations can be used to measure the thickness and growth rate of the layer. For that, the temperature dependent refractive index of the film (n_f) is required. The thickness (d) of the film corresponding to one period of oscillation is

given by Eq. 3.1,

$$d(nm) = \frac{\lambda}{2\cos(\theta)n_f} \tag{3.1}$$

where θ is the angle of incidence between laser beam and the normal to the substrate surface. Considering the time for one full oscillation, the growth rate accordingly full layer thickness can be extracted with high precision. In order to determine the layer thicknesses and growth rates of GaN, the oscillations obtained at the wavelength of 905.4 nm were considered. In this study, only the thickness of GaN layers was determined using this method because in order to use this method appropriately for the calculation of layer thickness, at least one full Fabry-Perot oscillation is necessary. However, due to the very low growth rate of InN and InGaN films, one full Fabry-Perot oscillation was not observed. In addition to the layer thickness evaluation, this method provides information about the layer morphology. For instance, with increasing roughness of the growing layer, the amplitute of the Fabry-Perot osciallations is decreasing. The deposition temperature was measured by a thermocouple located on the bottom side of the susceptor. The heater located under the susceptor contains three zones which are called as zone A, B and C. Each zone is connected to a seperate power supply. In order to maintain homogeneous surface temperature over the surface of the 2" wafer, different percentages in powers were employed on different zones. Argus, which is equipped with six diodes, was used for surface temperature measurement. Diode 1 and diode 6 read the temperature from the center and edge of the wafer, respectively. The other four diodes read the temperature in between the center and the edge. The outcome of these six diodes helps to measure the temperature difference between the center and the edge of the wafer. The temperature difference (if there is) can be minimized by adjusting the applied power percentage for the heater zones. For the growth of the layers, standard precursors were used. Trimethylgallium (TMGa), triethylgallium (TEGa) and trimethylindium (TMIn) were used as sources of Ga and In, respectively. TMGa used for GaN growth but for InGaN growth TEGa was employed. The reason of choosing TEGa as a source of Ga for InGaN is that TEGa consists less C atoms in the chemical structures compared to the number of the C atoms in TMGa sturucture and

therefore less C impurities form in the growing layer. Ammonia (NH_3) was employed as N source. As carrier gas, H_2 or N_2 were introduced. For InN and InGaN growth, N_2 carrier gas, while for GaN growth H_2 was used. The doping sources for n-type and p-type conductive layers were silane (SiH_4) and Biscyclopentadienylmagnesium (Cp_2Mg), respectively. Other growth parameters like growth temperature, growth pressure and V/III ratio will be given for the corresponding layers in the related chapters.

3.2 Standard characterization techniques

The structural quality of the layers was investigated by means of X-ray diffraction (XRD). For the measurements a Panalytical X'Pert Materials Research Diffractometer was used. The system comprises a 2-crystal Ge (220) monochromator and a X-ray mirror in the incident beam path. The wavelength of the X-ray source is 0.15406 nm. As a non-destructive method, crystalline phases of the materials as well as strain state, grain size, phase composition, and information about defect structure can be deduced by XRD. The line width (full width at half maximum (FWHM)) were measured by performing rocking curve measurements (ω-scans) in the symmetric (on-axis) (0002) and the asymmetric (off-axis) ((10-12), (30-32)) diffractions. The FWHM results were considered to interpret the crystal quality of the layers. The diffracted beam during rocking curve measurement was collected in an open detector configuration. Depending on desired resolution, the diffracted beam can be narrowed by inserting a 1 mm receiving slit in front of the detector. (This method will not yield real FWHM values and therefore, the values should not be considered for the interpretation of the crystal quality). Using on- and off-axis FWHM values, dislocation densities were deduced which will be explained later in this chapter. The alloy compositions of the InGaN samples were estimated based on the peak positions in XRD ω-2θ scans and the employed simulation using X'PERT EPITAXY software. The separation between substrate (in our case GaN) and InGaN peaks gives an idea about In composition. By this method, typically c lattice constant is measured. It is know that the change in lattice constant is correlated with In content in InGaN[133] and therefore, this method is providing reliable results about In composition in the InGaN alloys. However, to estimate In content accurately, the relaxation state

of InGaN layers origined from lattice mismatch must be introduced into simulation. Therefore, the relaxation status of the layers were estimated by employing reciprocal space mapping (RSM) measurements on (10-15) diffraction. The relative position of InGaN and/or InN peaks in RSM according to the GaN peak provides information about the strain state (relaxation status) of the layers. The relaxation status of the layers was considered during the simulation of ω-2θ scans, i.e., for the determination of In content in InGaN. Using RSM, phase separation can also be deduced.

Additionally, In contents of InGaN samples were determined by Rutherford backscattering (RBS) measurement. Random RBS spectra were taken with 1.4 MeV He ions and the thicknesses were estimated from the spectra at each position using the RUMP code. For more information please see at ref.[134, 135].

A detailed structural characterization was carried out by employing transmission electron microscopy (TEM) using a JEOL 2010FEG TEM system. The TEM system was operated at 200kV. Bright field imaging along [11-20] axis was taken from the cross section of the InN layers.

Atomic force microscopy (AFM) was used for surface morphology investigations of the layers. DualScope 95 SPM was used with tapping mode. There are three different scanning modes associated with AFM measurement. The first one is contact mode in which mode the tip is in contact with the surface and the image is formed by repulsive forces between tip and surface. The second one is in non-contact mode. In this mode the tip oscillates above the surface and the image is obtained from the attractive forces between the tip and the sample. The third mode, which is considered for AFM measurement in this study, is tapping mode. In this mode, the tip touchs the surface for small periods of time.

Optical investigation was carried out by photoluminescence (PL) spectroscopy. PL measurements at various temperatures and excitation levels were carried out using emissions of a continuous-wave (CW) helium-cadmium laser (λ= 325 nm, I_{exc} = 0.004 - 1.2 W/cm^2), a pulsed nitrogen laser (λ = 337.1 nm, I_{exc} = 1.34 - 285 kW/cm2) and the second harmonic of a Ti-sapphire laser (λ = 390 nm, I_{exc} = 300 kW/cm^2) as excitation sources. For investigation of PL at low temperature (LT), the samples were placed into a

closed-cycle helium cryostat CCS-150. PL emission was registered using an optical fiber and a spectrometer with a CCD camera. Unless otherwise stated, all PL measurements were performed at LT.

Differential transmission (DT) technique was used to evaluate carrier lifetimes at room temperature. As a pulsed laser source, Ti:sapphire femtosecond laser delivering 800 nm pulses of 120 fs duration at 1 KHz repetition rate was used. The output of the laser was split into equal parts and used to pump two optical parametric amplifiers (TOPAS) providing 120 fs pulses at wavelength continuously tunable between 1200 nm to 2400 nm. The wavelength of pump beam was set at 1000 nm (1.24 eV). The output of the other TOPAS was used an optically delayed probe beam at 1900 nm wavelength (0.65 eV). Transmitted intensity of the probe pulse with/without pump was measured by commercial InGaAs detector. The carrier lifetime (τ) is evaluated from the exponential decrease of DT measurement results.

Sheet carrier concentration and hall mobility values of InN layers were measured by Hall measurement using a Bio Rad HL550 system. Measurements were performed on 1 cm^2 pieces of the samples using 300 G as a magnetic source. The standard four-point van der Pauw Hall measurements were used. Without using any metal as contact material, ohmic contacts were successfully achieved due to the material properties of InN. Capacitance-Voltage (C-V) measurements were used to determine the conductivity type (majority carrier type) and acceptor concentration in Mg-doped $In_xGa_{1-x}N$ layers with In content $X_{In} \leq 18\%$. In order to perform C-V measurements on Mg-doped $In_xGa_{1-x}N$ layers, p-n diodes were fabricated as follows. The ohmic contacts for the p-type material ($In_xGa_{1-x}N$:Mg) were deposited by electron beam evaporation using 50 nm Ni/ 200 nm Au. Subsequently, contact annealing at 495 ^oC under N_2 atmosphere was carried out. To be able to contact the n-type GaN, a recess was performed using a chlorine-based reactive ion etch process. Gas flow rates for $BCl_3/Cl_2/N_2$ were 8/32/5 sccm. -70 V DC bias, 300 W ICP power and 0.5 Pa chamber pressure were used for etching process. As ohmic contact material, Ti/Al/Ni/Au (15 nm/100 nm/40 nm/50 nm) was used without post-deposition annealing. Before these processing steps, in order to activate Mg, $In_xGa_{1-x}N$ layers were annealed in N_2 atmosphere. The definite

annealing time including heating up and cooling down is 60 minutes which matches about 30 minutes annealing time at 750 ^{o}C. However, In-rich Mg-doped $In_xGa_{1-x}N$ (30%, 50%, 79% In) layers were annealed at a lower temperature of 565 ^{o}C for 30 minutes annealing time. X-ray photoemission spectroscopy (XPS) measurements were performed using an Omicron SPHERA spectrometer at the University of Warwick, UK. The samples were probed with a photon beam of energy hλ= 1486.6 eV produced by a monochromated Al Kα X-ray source. The IR reflection from $In_xGa_{1-x}N$ samples was measured using a Bruker Vertex 70v Fourier transform IR spectrometer (FTIR). The reflection spectra were recorded for an incident and reflected angle of 11^o to the surface normal. Detail information about XPS and FTIR can be found in Ref.[121].

3.3 Non-standard characterization techniques

3.3.1 Positron Annihilation spectroscopy (PAS)

Positron annihilation spectroscopy (PAS) is an effective method for investigation of vacancy type defects in semiconductors. As its name suggests, it is a spectroscopy of photons emerging from the annihilation of positrons with electrons[136]. As the positrons hit a material, they are immediately thermalized. The thermalized positrons diffuse into the material and annihilate with electrons, either from freely diffusing state or from a trapped state (at a defect site i.e. vacancy defect) (see Fig. 3.1). This annihilation process occurs mainly through the emission of two 0.511 MeV γ-photons in nearly opposite directions that carry away energy and momentum of the annihilating e^+-e^- pair which is called Doppler shift[137]. The Doppler shift of the individual γ-photons line will contribute to an overall broadening of the annihilation photo peak; this is often called Doppler broadening[138] (see Fig. 3.2). Due to the positrons thermalized quickly at the very beginning of the collision, the momentum of the electrons participating in the annihilation will be dominated on the Doppler shift therefore this method is an effective one to estimate the electron distribution through the layer.

With deep understanding of Doppler broadening spectrum (annihilation), vacancy concentrations as well as vacancy type with their chemical environment can be deter-

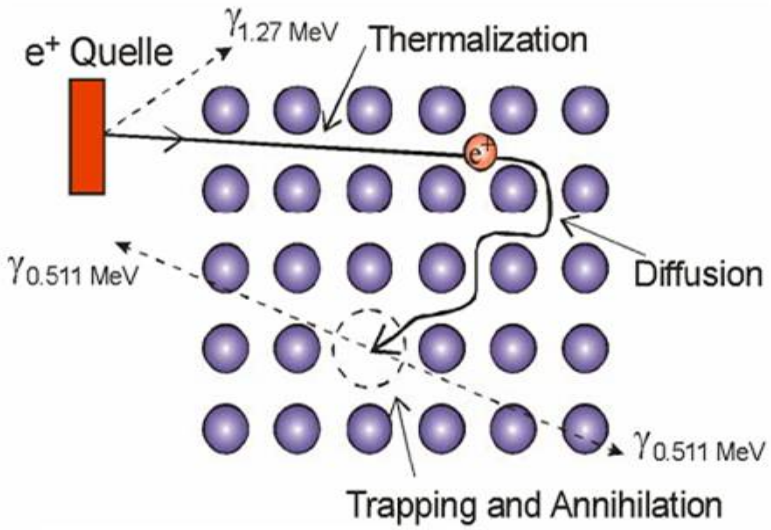

Figure 3.1: Schematic illustration of positron annihilation experiments using a slow-positron beam [after ref[139]].

mined. Usually the spectrum is divided into two parts; the first one is the middle and the second one is the tail part of the spectrum. These parts are shown in Fig. 3.2 and are characterized with shape parameters S and W, respectively. The former parameter - S - is experimentally determined as the relative area of the central part of the line shape to the total peak area. The latter - W - parameter expresses the relative contributions of the peak tails to the total peak area[140]. Doppler broadening has direct impact on the S-parameter in a way that S-parameter is higher if relative contribution of lower-momentum electrons to positron annihilation is enhanced. In other words, an increase in S-values reflects the enhanced positron traps at the open-volume defects i.e. vacancy type defects[140]. However, the W parameter becomes greater if contribution of the core electrons with higher momenta tends to increase. The S-parameter is measured as a function of positron beam energy (E) (will be shown in chapter 5). The energy can be converted to the estimated depth by using Equ. 3.2[138]:

$$d(nm) = \frac{AE^r}{\rho}(keV)/(gm/cm^3) \tag{3.2}$$

Where, A and r are widely used empirical parameters[141] and ρ is the mass density of

the studied material.

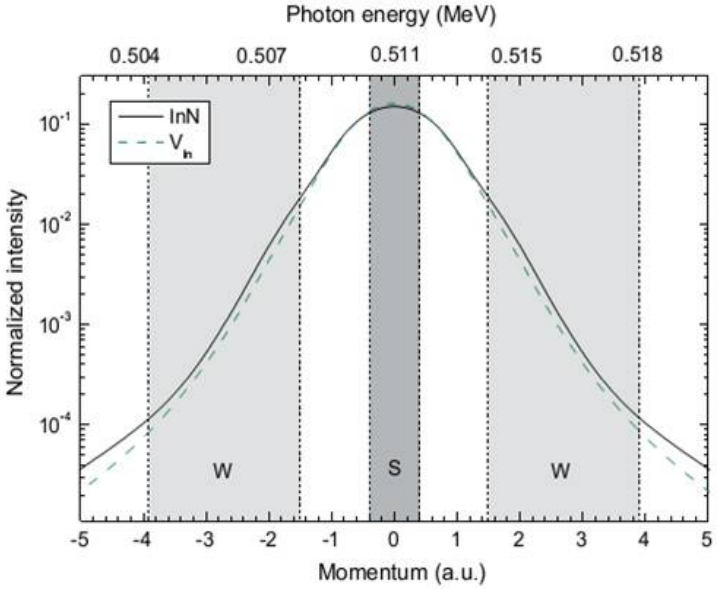

Figure 3.2: Spectrum of the Doppler-broadening (adapted from ref[137]).

The S and W parameters individually do not give any clue about the annihilation sites. Therefore these parameters are usually normalized to a reference value corresponding to a defect-free value of the material under investigation. The normalized value can then be compared between different samples and experimental arrangements. In this study, Positron annihilation measurements were performed using a variable energy (0.5-38keV) slow positron beam. The 0.511MeV e-p annihilation g-radiation was recorded with two Ge detectors with a Gaussian resolution function of 1.24 keV. The lineshape of the Doppler broadened annihilation peak was analyzed using the conventional valence (S) and core (W) annihilation parameters with respect to the reference points for InN, GaN and V_{In}. These reference points were determined using defect free samples (very high quality samples). More information can be found in reference[142].

3.3.2 Electrochemical C-V measurement (ECV)

Capacitance-Voltage (C-V) measurement is a convenient and non-destructive method for determination of doping profile in a semiconductor using a p-n junction or Shottky contact[127]. Shottky contact on semiconductor can be made by using metal

contacts[143, 144]. However, metal contacts fail to form Shottky contacts with semiconductor with a large surface carrier (electron) accumulation (like InN and In-rich InGaN and even Mg-doped InN and In-rich InGaN), but ohmic contacts can be made easily. By using a proper electrolyte, a Shottky contact can be made on this kind of semiconductor as a consequence of electric charge redistribution between the electrolyte and semiconductor. This method is called as electrochemical C-V (ECV) measurement. The surface carriers diffuse into the electrolyte resulting in a depletion of carriers at the surface of the semiconductor. Consequently, the semiconductor-electrolyte interface acts as capacitor of capacitance C, and the width of the depletion layer can be changed by applying an external voltage to the interface. If reverse bias is used, the depletion width is increased until breakthrough occurs, thus the capacitance is decreased. In the case when a forward bias is used, the depletion width decreases until current starts flowing, thus capacitance is increased. With this method not only basic C-V measurement but also depth dependent C-V measurement can be performed. For depth dependent C-V measurement, an electrolyte is used to make the barrier and to remove material electronically so both processes can be carried out in the same electrochemical cell and controlled electronically, using automatic equipment to perform the repetitive etch/measure cycle and generate a profile plot[145]. (In this study etching was not performed). The theory of the measurement is different for n- and p-type semiconductors. For n-type semiconductor electron-hole pairs (e^--h^+) are formed by illuminating the interface with UV light. Light creates e^--h^+ at the surface of the semiconductor. If these holes diffuse to the surface they may release valance atoms of semiconductor surface atoms by recombination. The electrons, on the other hand, flow to the semiconductor contact. If all valance electrons of a semiconductor are removed, the ionized atom cores can be dissolved into the electrolyte fluid. However, for p-type semiconductor, holes may be conducted from the semiconductor contact to the surface by applying forward bias[146]. As it is clear from these explanations, the theories are valid only for pure n- and p-type semiconductors but not for semiconductors with surface accumulation. The junction forms on this kind of semiconductor are not like electrolyte/semiconductor anymore but electrolyte/metal. In this case, a double layer model should be considered even if it is

not exactly matching with this kind of material system. More information about the double layer model can be found in references[147, 148, 149]. Despite these difficulties, ECV measurement can be used to investigate the electronic properties of semiconductors with surface carrier accumulation. The acceptor or donor concentration can be deduced by Mott-Schottky (M-S) equation (Equ. 3.3) and indirectly by Mott-Schottly plot[145]. The inverse square of capacitance versus voltage gives the Mott-Schottky plot [C^{-2} vs V]. As can be inferred from Mott-Schottky equation (Equ. 3.3), sign of the slope (dC^{-2}/dV) in the Mott-Schottky plot defines the carrier type. The positive or negative sign of the slope indicates the majority carrier concentration. If the slope is negative (positive), electrons (holes) are the majority carriers in the semiconductor.

$$N = \frac{-2}{e\epsilon_0\epsilon_r A^2 \frac{d(\frac{1}{C^2})}{dV}} \tag{3.3}$$

where, e is electron charge, ϵ_0 and ϵ_r are vacuum permittivity and dielectric constant of the material, respectively, A is measured area, N is carrier concentration, $d(1/C^2)/dV$ is the slope of the Mott-Schottky plot. The depletion depth (W_d) is calculated by Equ. 3.4:

$$W_d = \sqrt{\frac{2(\phi - V)\epsilon_0\epsilon_r}{qN}} \tag{3.4}$$

where ϕ is built in potential, V is applied voltage and q is charge of the electron.

All ECV measurements were performed using a Wafer Profiler CVP21 equipment. The used measurement setup is demonstrated in Fig. 3.3. As an electrolyte 0.1 mol/litre sodium hydroxide (NOH) solution was used. The electrical contact between the wafer and the two terminals, which are supplying the current, was enhanced by GaIn eutectic. Before wetting the surface, I-V curve was checked to ensure that the contact shows ohmic character. After that, 1 mm^2 area was wetted and I-V curve was rechecked to ensure that the contact exhibits Schottky-like character. The rest potential between the electrolyte and a saturated calomel electrode (SCE) (reference electrode) was measured. The rest potential belongs to the leakage and the surface morphology of the semiconductor. Sealing rings shown in Fig. 3.3 prevents the electrolyte leakage[146].

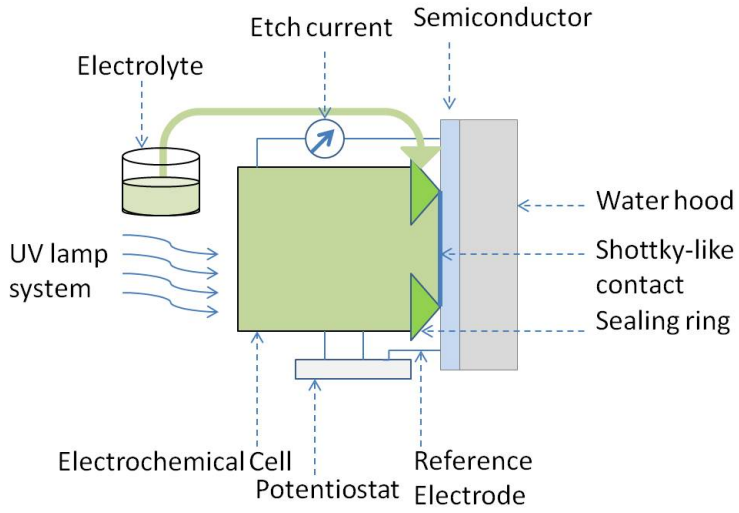

Figure 3.3: Measurement setup used for ECV characterization. Small area on the surface wetted with electrolyte via a sealing ring and the interface act as Schottky-like contact. For etching of n-type semiconductor, an UV lamp system is used to create electron-hole pair on the surface.

3.3.3 Raman Spectroscopy (Longitudinal Phonon-Plasmon Coupling)

Raman scattering is a standard optical characterization technique for studying various aspects of solids such as lattice properties (information on stress, crystal quality), electronic properties (carrier concentration, hall mobility), and magnetic properties. Raman scattering has many advantages when compared with other spectroscopic techniques: it is in principle non-destructive, contactless, and requires no special sample preparation such as thinning or polishing. Moreover, it is fast and enables measurements with high spatial resolution. Raman scattering occurs essentially as a result of modulation of the electronic polarizability which is induced by various elementary excitations in solids such as phonons and plasmons. In the case of Raman scattering by phonons, the scattering efficiency is higher in covalent crystals than in ionic crystals, because in covalent crystals the valence electrons are less localized and larger fluctuation of the polarizability can be induced by lattice vibration. From this viewpoint, nitride semiconductors are suitable for Raman scattering studies, since the chemical bonding is a mixture of covalent and ionic bonding[150]. Based on the group theory, there are eight sets of phonon modes

(E_2 (high), E_2(low), A_1(LO), A_1(TO), E_1(LO), E_1(TO), and $2B_1$) exist in hexagonal wurtzite structure[150, 151]. In the simplest geometry, Raman scattering is produced and measured in the z(x x)$\overline{z}$ backscattering configuration. In this notation, z represents the direction of propagation of the incident laser in the (0001) direction, $\overline{z}$ represents the direction of propagation of the scattered light after energy relaxation in the (000-1) direction, x represents the polarizations of the electric field of the incident and scattered photons respectively[152]. In this experimental configuration, which was used during study, only two E_2 (high) modes and the A_1 (LO) mode are allowed phonons modes of InN. Information on stress and crystal quality can be extracted from the E_2 (high) phonon frequency and linewidth[150, 151, 153]. If a measured frequency of E_2 (high) mode is higher than the reference value, it can be considered as an evidence of a compressive strain in the film. Regarding the linewidth, the narrower the linewidth the better the crystal quality. While E_2 (high) mode is used for the investigation of crystal quality, due to its polar character, the A_1(LO) mode can be considered for estimation of bulk carrier concentration[150]. In polar semiconductors, collective excitation of free carriers (plasmon) can interact with longitudinal-optic (LO) phonons (optical lattice vibrations) via longitudinal electric field. As a result of this interaction instead of a pure plasmon and a pure LO-phonon, two coupled modes appear which have mixed plasmon-phonon character (LOPC$\pm$ or LPP$\pm$). The LPP mode consists of upper- and lower-frequency branches donated as LPP+ mode and LPP- mode[154, 155, 156]. LPP$\pm$ mode frequencies were calculated by solving the equation for longitudinal excitation, $\epsilon(\omega)$=0 (equ. 3.5) which was proposed by Irmer[154] and Vagra et al.[156]. Here $\epsilon(\omega)$=0 is the dielectric function written by phonon and plasmon contributions neglecting the damping terms.

$$\epsilon(\omega) = \epsilon_[1 + \frac{\omega_L^2 - \omega_T^2}{\omega_T^2 - \omega^2 - i\omega\Gamma} - \frac{\omega_P^2}{\omega(\omega + i\gamma)}] \tag{3.5}$$

Where ω_T and ω_L are the uncoupled A_1 (TO) and A_1 (LO) with the frequencies of 450 cm^{-1} and 590 cm^{-1}[62], respectively. ϵ_∞ of 6.7 is the optical dielectric function[62] and Γ and γ are phonon and plasmon damping constants. ω_p is the plasmon frequency

(blue curve in Fig. 5.14a) which is defined as:

$$\omega_P = \sqrt{\frac{4\pi ne^2}{\alpha_\infty m^*}} \tag{3.6}$$

where, m*=0.54mo the effective mass of the electron and n is the free carrier concentration. For the evaluation of LPP+ and LPP-, damping terms Γ and γ were neglected because eliminating the damping allows to read the carrier concentration directly from the position of the A_1(LO) (i.e. LPP+ mode)[154, 155, 156]. The variations of LPP± mode frequencies with respect to carrier concentration are shown in Fig. 5.14a. The results of the calculation will be discussed in chapter 5 section 5.2.4.

3.4 Calculation of defect density using XRC FWHM values

Models, which were developed by Srikant et al.[31] and Lee et al.[157] for the crystal growth of highly mismatched films, were used for the evaluations of dislocation densities[62]. For calculation, the FWHM of on- and off-axis orientations were measured by XRD ω-scans on both symmetric (0002) and asymmetrics ((10-11), (10-12), (30-32)) diffractions. By extrapolating the FWHM values of the increasingly off-axis rocking curves to 90^o(with the on-axis rocking curve defined as the tilt angle Γy) according to Equ. 3.7, values for the twist and tilt angles were determined.

$$\Gamma = \sqrt{(\Gamma_y cos\chi)^2 + (\Gamma_z sin\chi)^2} \tag{3.7}$$

In Equ. 3.7, Γ is the FWHM at an angle χ, Γ_y (the tilt angle) is the on-axis (0002) rocking curve FWHM and Γ_z (the twist angle) is the extrapolated FWHM value for a rocking curve rotated 90^o to the surface normal. The resulting Γ_y and Γ_z were used to calculate the dislocation densities with screw character (using tilt angle Γ_y) and pure edge character (using twist angle Γ_z) according to Equ. 3.8:

$$\rho_s = \frac{\Gamma_y^2}{1.88c^2} \qquad and \qquad \rho_e = \frac{\Gamma_z^2}{1.88a^2} \tag{3.8}$$

in which ρ_s and ρ_e are the screw and edge dislocation densities, respectively. c and a are the relevant Burgers vectors (the InN c lattice constant of 5.693 Å for dislocation

with screw character and the InN a lattice constant of 3.533 Å for pure edge dislocation) and 1.88 is a TEM calibration constant for InN[62].

4 Substrates for InN and InGaN epitaxy

Due to the low lattice mismatche between InN and GaN (see Table 2.1 chapter 2), GaN grown on sapphire was selected as a template for InN and InGaN epitaxy. This chapter focuses on the basics of MOCVD of GaN on sapphire and gives a discussion of the structural and the morphological characterization results.

4.1 Growth of GaN structures

The growth of GaN was done on 2" c-plane sapphire substrate using MOCVD. The entire growth process was monitored by in-situ characterization techniques. The structure of the GaN templates is shown in Fig. 4.1. The growth parameters for each sequence are listed in Table 4.1. In-situ monitoring data; reflectivity and growth temperature against time, are shown in Fig. 4.2. The growth starts with a HT bake of the sapphire in order to clean up the surface (by removing upper-most monolayers) prior to the growth. This step was carried out in an H_2 atmosphere at surface temperature of 1090 ^oC for 300 seconds. The second step is a nitridation. The goal of this step is to remove the oxide layer on the sapphire surface and to form a thin AlN layer. The AlN layer helps to reduce the in-plane lattice mismatch from 16% (between GaN/sapphire) to 2.5% (between GaN/AlN)[20, 158, 159]. For the nitridation, a flow of 250 sccm of NH_3 was introduced in the reactor and the wafer was nitridized for 60 seconds. Following this, GaN nucleation layer was grown at low-temperature of 550 ^oC. Due to the low growth temperature, an amorphous GaN layer (cubic phase) is deposited on the surface. During this step, seeds are formed on the surface and grow laterally until the coalescence

occurs. The nucleation density can be controlled by changing V/III ratio (varying group-III supply) and growth temperature[160, 161]. During nucleation, 0.52 μmol/min TMGa and 81.5 μmol/min NH_3 were used. Following nucleation, the temperature was ramped to 1035 ^oC in order to crystallize the amorphous GaN nucleation layer. High temperature exposure of the nucleation layer leads to the transformation of the nucleation layer into hexagonal (0001) GaN islands and to a roughening of the films by forming an island-like textures[160]. This step is so called recrystallization. The surface morphology resulting from the recrystalization mechanism is critical for HT-GaN films[162]. Due to the roughening of the surface, a decrease of the surface reflectivity is observed. After the recrystallization, three stacks of GaN layers are grown at high temperatures (see Fig. 4.1. The high temperature growth of the GaN enhances the mobility of the reactive species on the surface and therefore high quality GaN layers are obtained. At the initial stage of the growth, the film undergoes a coalescence phase, during which a transition from a three-dimensional (3D) growth to a two-dimensional (2D) growth occurs. Although some dislocations penetrate from the low-temperature growth region to high-temperature one, many of them are elongated through the 3D to 2D transition and stopped at the interfaces between the GaN layers stacks.

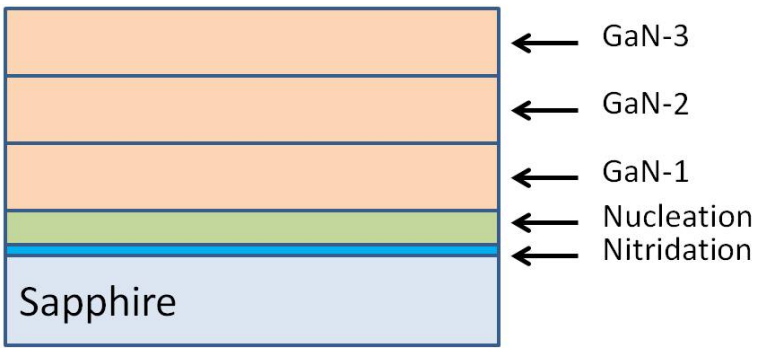

Figure 4.1: The layer structure of GaN templates used for the InN and InGaN epitaxy.

Table 4.1: Summary of the GaN growth parameters.

Layer	Surface Temp.	Growth pressure	V/III	Carrier gas	Time
	^{o}C	mbar	-	-	seconds
Desorption	1090	100	-	H_2	300
Nitridation	550	900	-	H_2	60
Nucleation	550	900	3267	H_2	500
GaN1	1035	900	716	H_2	1200
GaN2	1050	600	1140	H_2	2100
GaN3	1050	400	1140	H_2	5400

4.2 XRD rocking curve and AFM surface morphology of GaN templates

Here the on- and off-axis XRD rocking curve results, which are correlated with the dislocation densities, will be discussed and the surface morphology investigation by AFM will be presented. Figure 4.3a shows the rocking curve results for (0002) and (10-12) diffractions. A very sharp and narrow symetric (0002) peak with a FWHM value of 225 arcsec together with relatively less intens and broader asymmetric diffraction (10-12) peak with a FWHM of 310 arcsec were measured. These results indicate a very good crystal quality for the GaN layer. Figure 4.3b shows the surface morphology of a GaN layer as seen by AFM. The atomic steps and the very low RMS roughness of 0.4 nm on a 5x5 μm^2 scan area are also demonstrating the good-quality of the GaN layer. The other GaN templates used in this study are characterized by similar results.

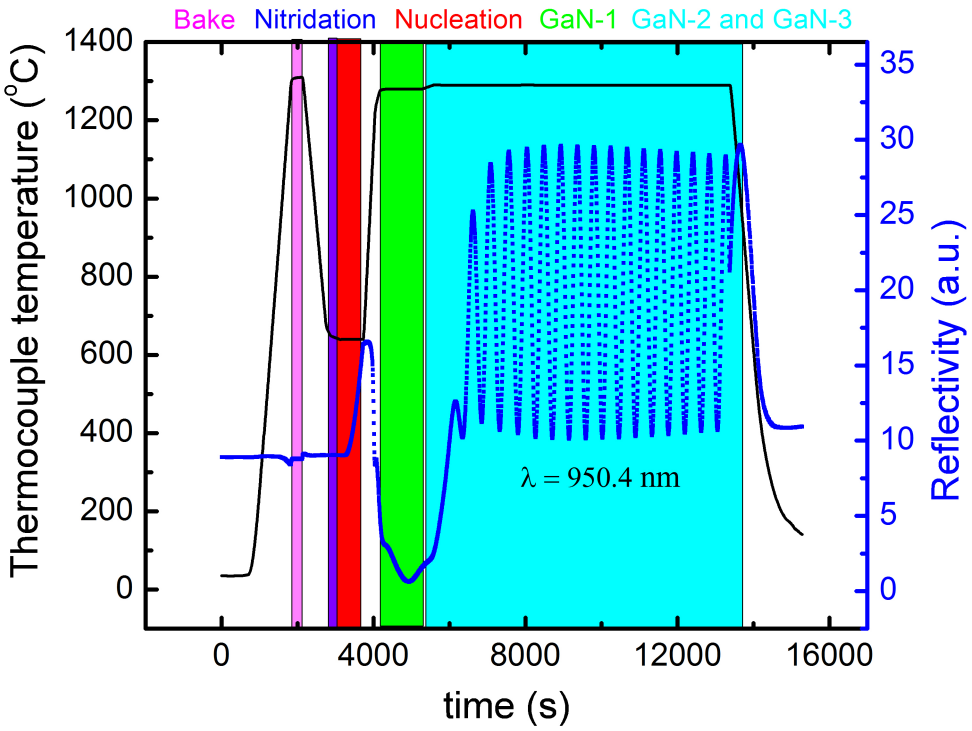

Figure 4.2: Reflectivity and temperature variations against time.

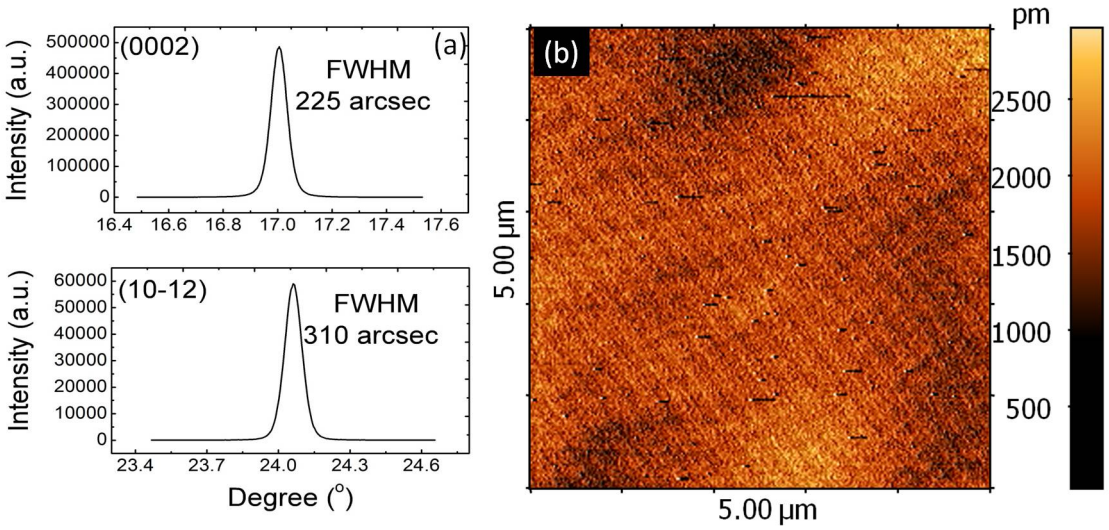

Figure 4.3: a) XRD ω-scans for the diffractions of (0002) and (10-12) and b) surface morphology of a GaN layer as seen by AFM.

5 Effect of growth temperature and V/III ratio on InN epitaxy

This chapter comprises a structural, morphological, electrical and optical investigation of thick InN films grown on GaN-on-sapphire templates. The chapter will be divided into two sub-sections. In the first one, the epitaxial InN grown at different growth temperature and characterization results are discussed. After that, the effect of V/III ratio (nitrogen-to-Indium flux ratio) on the growth process and the layer properties of InN is examined.

5.1 Growth and characterization of InN grown at different temperature

A series of InN layers was grown on undoped Ga-polar GaN templates. The growth of GaN-on-sapphire templates was explained in the previous chapter. The growth process and layer structure for InN are demonstrated in Fig. 5.1, respectively. In order to avoid the degradation of the GaN surface, NH_3 was kept open during temperature ramping to InN growth temperature. After reaching the InN growth temperature of 500 - 565 ^oC, temperature stabilization ('TS') time of 200 sec. was applied ((Fig. 5.1)b) to reduce the effect of temperature overshooting. After that, a TMIn flow of 1.2 μmol/min was employed together with an NH_3 flow of 223 μmol/min. Corresponding V/III ratio is 145k. Growth pressure was set to 600 mbar. All InN growth ('G') runs were carried out in N_2 ambient on 4 μm thick GaN templates (Fig. 5.1b). N_2 carrier gas is known

to be compulsory due to the etching effect of H_2 on InN[111]. The effect of growth temperature on the InN properties is studied by analyzing four different layers grown at different growth temperatures of 500, 520, 550 and 565 ^oC. All other growth parameters (mentioned above) were kept constant. The layer thicknesses of InN and GaN are 330 nm (165 nm/hr) and 4 μm (1.4 μm/hr), respectively.

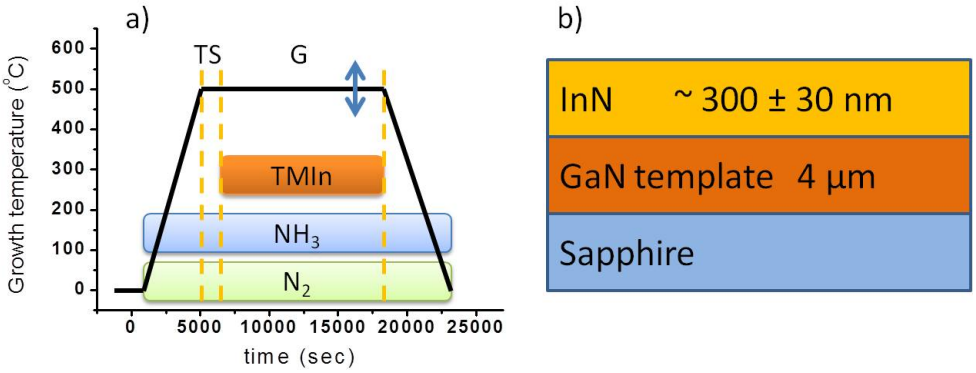

Figure 5.1: a) Deposition process for InN films including temperature stabilization (TS) and main layer growth (G). The sign (↕) depicts variation of temperature from sample to sample. b) Layer structure.

5.1.1 The effect of growth temperature on structural properties and morphology of InN layers

Figure 5.2a) displays HRXRD ω - 2θ measurement results of InN layers. A vertical shift of the single scans was employed to make the image clearer. The expected diffraction peaks corresponding to InN (0002) and GaN (0002) can be seen in each profile. In addition, at low and at high growth temperatures, a peak corresponding to the (10-11) reflection of metallic In appeared between InN and GaN peaks. The detected peak is an indication of In droplets on the surface. The existence of droplets can be confirmed by pictures from optical microscopy as shown in Fig. 5.2b. While at low temperature of 500 ^oC particles seen as white spot are observed on the surface, at a temperature of 550 ^oC, these particles disappeared (Fig. 5.2b). Increasing the growth temperature from 500 ^oC to 550 ^oC obviously helps to prevent In droplet formation which is caused by a lack of reactive N atoms in the reactor. With temperature increase to 550 ^oC,

the NH_3 decomposition is enhanced and the formation of In droplets on the surface can be avoided. But with further increase in temperature to 565 ^{o}C, In droplets could be observed again (Fig. 5.2a). This can be explained by N desorption at high growth temperature, leaving metallic In on the surface

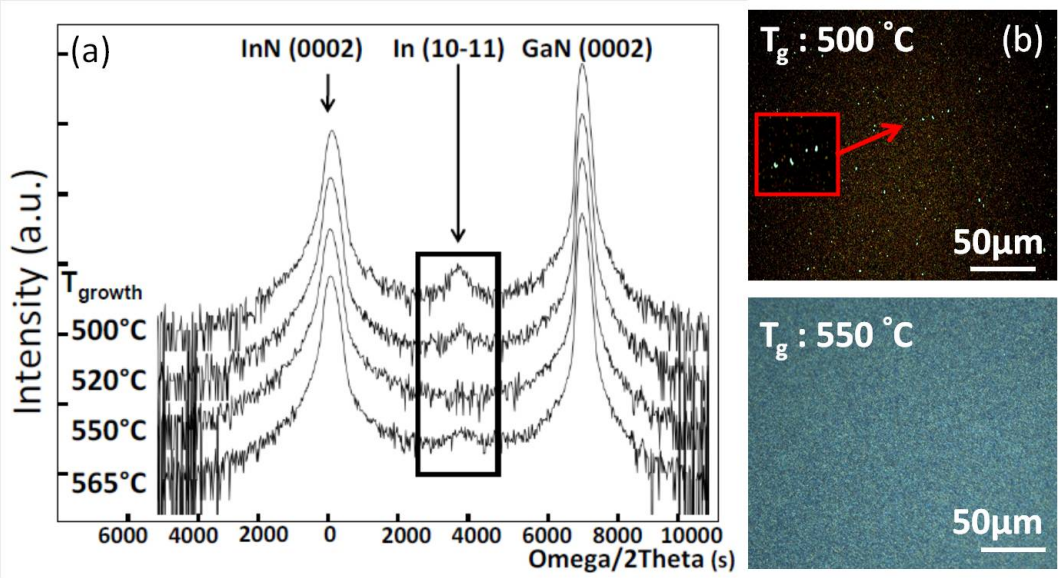

Figure 5.2: a) HR-XRD ω - 2θ scans of temperature series including the InN (0002), In (10-10) reflections. b) Optical microscopy images of InN grown at 500 and 550 ^{o}C.

Figure 5.3a shows the surface morphology of InN/GaN films grown at different growth temperatures of 500, 520 and 550 ^{o}C. The surface RMS values of these films are 18, 12 and 33 nm for a scan size of 5 x 5 μm^2. All the films investigated here yield grainy uncoalesced morphology and lateral grain size is observed to change with growth temperature. At lower growth temperature of 500 ^{o}C, the diffusion of the reactant species is relatively slow which leads to the formation of small grains with dense structure. Higher growth temperature enhances the diffusion of reactants. Therefore, the individual island size is increased. As a result, the density gets lower. It is believed that the increased island size at the beginning of the growth leads to an undesired rough surface morphology due to enhanced diffusion of ad-atoms at high temperature [163]. In SEM (Fig. 5.3b) images, one can see that the increase in growth temperature from

500 to 550 ^{o}C enhances the gathering of small grains but full coalescence does not occur. This is supported by the TEM investigation as well. In Fig. 5.3c, a cross-section bright view TEM result of InN film grown at 550 ^{o}C is shown. Apparently, InN growth follows the Volmer-Weber growth mode[164] for which three dimensional growth takes place with hexagonal InN pyramids covering the GaN surface. At the beginning of growth the nuclei form as islands which are predominantly shaped as faceted hexagonal pyramids[164]. Even though the islands impinged upon each other after a long growth time, full coalescence is not observed (Fig. 5.3c bottom part of TEM image). This is corresponding to a low lateral growth rate of islands and a large lattice mismatch of 11% between InN and GaN. Moreover, it is explained by Abhislek et al.[165] that the surface of faceted In-polar InN islands tend to grow preferably at a specific orientation due to the polarity of nitrides which also hampers coalescence (for more information refer to[165]). At 565 ^{o}C, a peeling off (or layer delamination) is observed in the SEM images (Fig. 5.3b). Peeling off can be explained with a loosing of contact between film and substrate. This phenomenon is well known for GaN, too[166]. For the case of GaN growth, the peeling off occurs between layer and substrate during cooling down due to thermal expansion coefficient differences[166]. However, in the case of InN, peeling off can occur during growth due to the larger lattice mismatch between InN and the substrate. The large mismatch of 11% between InN and GaN leads to a relaxation by formation of misfit dislocations at the very initial stage, which corresponds to less than a monolayer according to the People-Bean's model, of the growth[167]. The large compressive strain caused by the large lattice mismatch released its energy by formation of misfit dislocations. This results in a weak interface bounding strength with high defect density and therefore a weak interface adhesion. Due to the coalescence of the grains and due to the defective interface, the film delaminates by crack formation along the interface as shown in the TEM image in Fig. 5.3c[168, 169]. Some pores with maximum length of about 500 nm labeled by green arrows are seen in this image. It is obvious that the InN layer on the pore areas is identical with the InN on the GaN without any pores. By considering this, it can be inferred that the long pores are caused by the combination of small cavities during preparation of the samples for TEM measurement.

Because of the long pores at the interface and the weak atomic bond strength of InN, film delamination occurs after a critical thickness value[170].

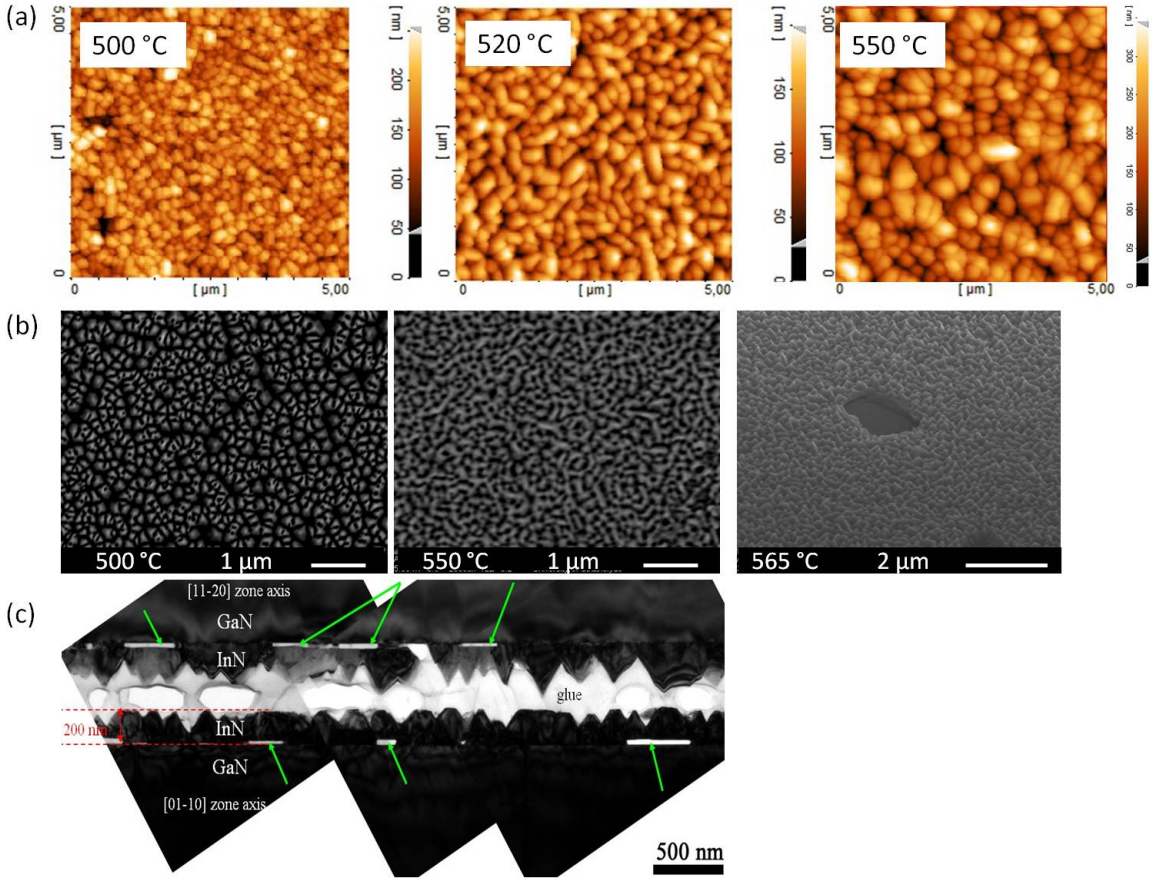

Figure 5.3: a) Surface morphology of InN/GaN layers grown at temperatures of 500, 520 and 550 ^{o}C. (b) SEM plan view images of InN/GaN layers grown at 500 and 550 ^{o}C (samples tilted 45^{o}), the layer grown at 565 ^{o}C tilted 49^{o}. (c) TEM image of the sample grown at 550 ^{o}C.

5.1.2 Defect density calculation by XRD measurement results

In this part, the effect of growth temperature on dislocation density will be discussed based on the Srikant theory explained in chapter 3 section 3.4. For the calculation of dislocation density, full-width at half-maximum (FWHM) values of InN layers in both on- and off-axis orientations were measured by rocking curve scans (ω-scans). The inset

of Fig. 5.4(a) contains ω-scans of (0002), (10-12) and (30-32) diffractions of the sample grown at 500 ^{o}C. It is seen that the on-axis (0002) rocking curve peak is much narrower than the other two off-axis, (10-12) and (30-32), rocking curve peaks. This confirms that the dominant dislocations in InN have an edge component which is usual for a system with large in-plane lattice mismatch. Figure 5.4a displays the extrapolation of the FWHM values from the on-axis rocking curve at 0^o inclination angle to the increasingly off-axis rocking curves to 90^o. The extrapolations were carried out based on the Equ. 3.7. The Γy and Γz points which are corresponding to the an angle of 0^o and 90^o in ω-scans give the tilt and twist angle, respectively. These values were considered for the determination of dislocation density using Eq. 3.8. Variation of the number edge and screw type dislocation densities as a function of growth temperature is shown in Fig. 5.4b. The increase in growth temperature above 500 ^{o}C leads to a decrease of Γz which corresponds to a decrease in edge dislocation density from 1.57x10^{11} cm^{-2} to 7.41x10^{10} cm^{-2}. The decrease in the number of edge-type dislocations can be attributed to the increase of adatom mobility which enhances the lateral growth rate. The lateral growth leads to less grain boundaries by forming larger grains due to island coalescence[62]. Formation of large grains and island coalescence at high growth temperature can be clearly seen in AFM images in Fig. 5.3a. On the contrary, a fluctuation in Γy values is observed with temperature variation. The lowest Γy value is measured at a growth temperature of 520 ^{o}C and therefore, the lowest screw dislocation density of 2.03x10^9 cm^{-2} is obtained at this growth temperature. For both lower (500 ^{o}C) and higher (550 ^{o}C) growth temperatures, an increase of Γy are found. Correspondingly, an increase in screw dislocation density to 5.36x10^9 cm^{-2} and 1.15x10^{10} cm^{-2}, respectively, is found.

5.1.3 Electrical properties of InN and surface electron accumulation

It is well known that regardless of deposition technique, InN and In-rich heterostructures have a large background n-type carrier concentration and a very high surface electron accumulation[76]. The origin of the surface accumulation was extensively analyzed in chapter 2 and some results will be discussed in chapter 6. In this section electrical

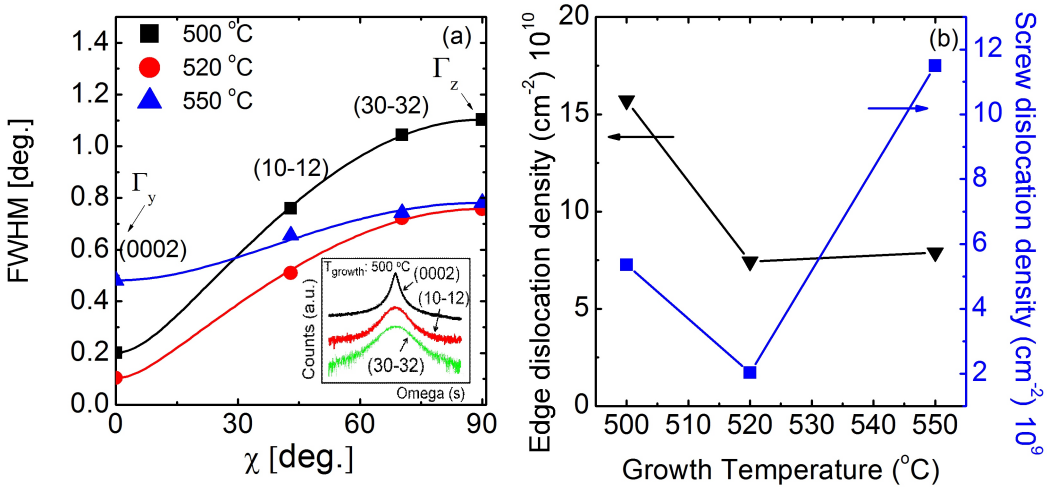

Figure 5.4: Inset (a) On- and off-axis rocking curves for the samples grown at 500 ^{o}C. (a) Resulting curves of Eq. 3.8 using the FWHM values of rocking curve for the samples grown at different substrate temperatures. (b) Edge and screw dislocation densities variation as a function of growth temperature.

characterization using the conventional Hall Effect measurement and an evidence of surface electron accumulation by ECV measurement results will be briefly presented. Room temperature Hall measurements utilizing the four point probe contact method were carried out. Without using any contact material, ohmic behavior was observed due to the large surface electron accumulation. The thickness of the layers, determined by SEM, is about 300±30 nm (155±5 nm/hr). Figure 5.5a shows the variation of the sheet density and Hall mobility of the InN layers as a function of growth temperature. Figure 5.5b demonstrates the carrier concentration profile on the surface of InN. The theory for the calculation for the carrier concentration and depth using ECV measurement results can be found in chapter 3. With increasing substrate temperature from 500 ^{o}C to 550 ^{o}C, a decrease in sheet density from 4.6x10^{14} cm^{-2} to 1.32x10^{14} cm^{-2} and corresponding bulk carrier concentration from 13.3x10^{18} cm-3 to 4.1x10^{18} cm^{-3} is observed. In conjunction with this, an increase in carrier mobility from 536 cm^{2}/Vs to 1200 cm^{2}/Vs is achieved. The origin of high background carrier concentration is usually explained by H and O impurities[84, 86]. In addition, N vacancies can be blamed for the high background carrier concentration. It has been reported that an enhanced decom-

position of NH_3 is likely to reduce the nitrogen vacancies and henceforth a decrease in the background electron concentration[95, 96]. Indications about decreasing numbers of N vacancies in the interface region between InN and GaN, measured by positron annihilation spectroscopy (PAS), are found[142]. A detailed investigation and results will be described in the next section. The recorded increase in carrier mobility can be explained by a decreasing carrier concentration and hence fewer charged carrier scattering centers[171, 172, 173, 174, 175]. The sharp decrease in mobility to 570 cm^2/Vs at 565 ^oC is attributed to the layer delamination. Any kind of defects which can distort the mean free path of electrons can decrease the mobility. Layer delamination leads to additional defects formation in the crystal and hence less mobility due to enhanced scattering of the carriers from the defects. Similar behavior was observed by Ablishek et al.[176] as well. A gradient of carrier concentration from 10^{21} to 10^{19} cm^{-3} is observed within a depth of 1.5 nm in ECV measurements (Fig. 5.5b). This proves the existence of a surface electron accumulation. Sheet carrier concentration can be calculated by integrating the carrier concentration over depth as explained in chapter 3. As a result of calculations, sheet carrier concentrations (donor concentration) of 2.16x10^{13} cm^{-2} and 1.73x10^{13} cm^{-2} for 500 ^oC and 550 ^oC are obtained, respectively. The difference between the surface carrier concentrations determined by Hall and ECV techniques can be a consequence of interface electron accumulation which also effects the Hall effect measurement. Large lattice mismatch between InN and substrate, which is caused to the formation of the dislocations at the interface, results in carrier accumulation at the interface[79].

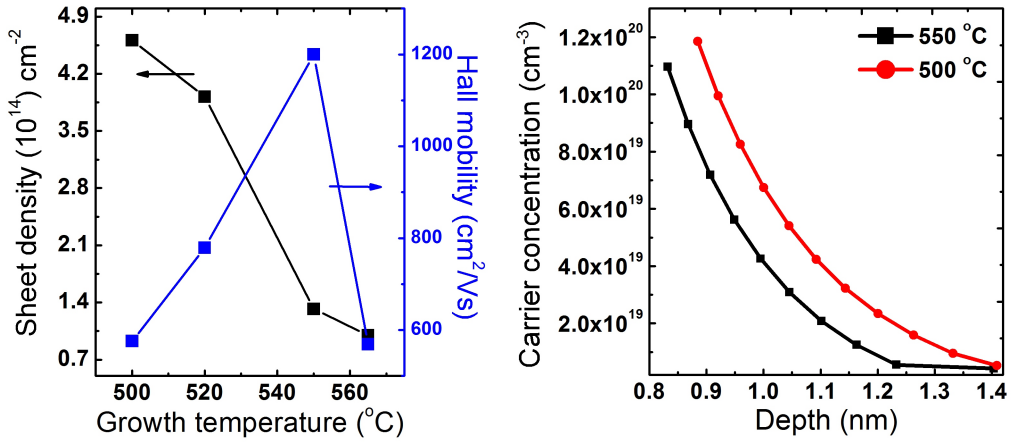

Figure 5.5: a) Room temperature Hall effect measurements results of InN layers. b) ECV of InN layers grown at 500 and 550 °C.

5.1.4 Study of vacancy type defect by PAS

Hydrogen impurities, defects, interstitials as well as N vacancies are believed to be some donor sources responsible for high background carrier concentration in MOCVD-grown InN layers[177, 178, 179, 180, 137]. Due to compulsory low growth temperature of InN, cracking efficiency of NH_3 is too low to supply enough reactive N atoms to avoid the formation of N vacancies in the InN layers. In this part, the role of growth temperature on the incorporation of point defects in InN layers will be presented. The results will be described based on two main parameters of S and W extracted from Doppler broadening measurement. The S parameter is defined as the ratio of counts in a central region of the photo peak to the total counts in the peak. Therefore it has a direct relation to the Doppler broadening. In other words, the S parameter provides information about the annihilation fraction of the positrons by vacany type defects. The W parameter which is extracted from the wing region of the Doppler spectrum can be used to examine the contributions from core electrons in Doppler broadening. More information is given in Chapter 3. Variation of S-parameters as a function of the implantation energy (SE) extracted from the Doppler broadening spectrums is shown in Fig. 5.6a. The characteristic values for the InN and GaN lattice are displayed for comparison. At low implantation energy i.e. low mean penetration

depth, positrons annihilate at the surface of the material. The increase in implantation energies to 3 keV enhances the penetration of positrons deeper into the film and therefore contributions caused by surface are avoided. As a result, an approach of peak position to the characteristics S-parameter of InN is observed. The definition of characteristics values of the InN and GaN are described in chapter 3. Since the peak position at 3 keV is close to the characteristics value of InN, it can be inferred that in the bulk there is no vacancy trapping detected. However, a strong rise in the intensity of the peak is noticed as the implantation energy is increased from 2.5 to 7.5 kV. At around 7.5 keV, corresponding to a mean implantation depth of 150 nm, a maximum intensity of the correspondingly maximum S-parameters is obtained. This is caused by the trapping of positrons at vacancy-type defects at the interface[142, 137]. Interestingly, there is no increase in the intensity of the peak from the sample grown at 550 ^{o}C. This suggests a decrease in the concentration or in the sizes of vacancies with increasing substrate temperature to 550 ^{o}C. With further increase of the implantation energy above 10 keV, the SE profiles of all the samples approache directly the characteristic values for GaN (Fig. 5.6a) which means the positrons penetrate into the GaN template. In order to define the character of the vacancy defects observed in the positron annihilation measurements, we take a look at the SW-plot in Fig. 5.6b in which the measured W-parameters of each sample are plotted as a function of the S-parameters. The S and W parameters are normalized to the characteristic (defect-free) value of GaN. The characteristic values for the InN and GaN lattice, and the V_{In}[181], are displayed for comparison. A clear shift of the W - S plot (a magnification of the most relevant area is included as inset in Fig. 5.6 (b)) from V_{In} (dashed line)[181] is observed for the samples grown below 550 ^{o}C. The experimental results are compared with the theoretical calculations studied by Rauch et al.[137] who figured out that the deviation from the In vacancy line (V_{In}) is caused by In vacancies. The amount of deviation gives a clue about the number of N vacancies which form a complex with In vacancies. The calculation result indicates that In vacancies form a complex with an average of 2 - 3 N vacancies[137]. A similar tendency i.e. the amount of deviation from V_{In} line is depending on the number of N vacancies forming complexes with In vacancies,

has been obtained for GaN[182, 183] and InN:Mg[184]. These results confirm that the observed increase in electron concentration with decreasing growth temperature can be explained by an increased incorporation of nitrogen vacancies, indicated by an increasing S-parameter and the deviation of the measured points from the V_{In}-line.

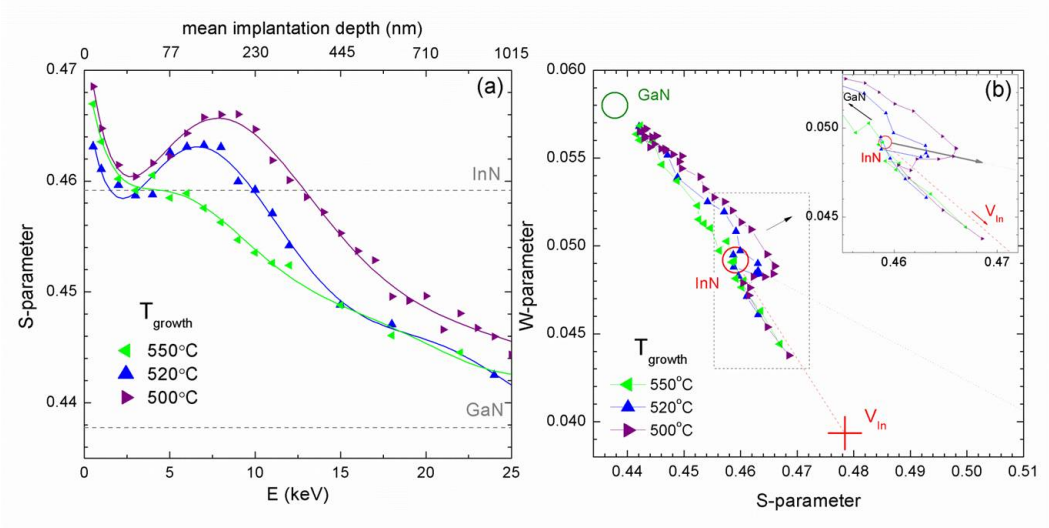

Figure 5.6: a) S-parameter of different InN layers as a function of the positron implantation energy/mean implantation depth. Characteristic values of the InN and GaN lattices are displayed for comparison. b) Line shape analysis of the recorded S and W parameters of the investigated set of samples. A magnification of the most relevant area is included as inset, in which the characteristic SW point of the near-interface region of each sample is displayed enlarged. Reference values for GaN, InN, and VIn are shown for comparison.

5.1.5 Low temperature photoluminescence characterization of InN layers

As described in chapter 1, earlier studies indicated a large band gap of 1.9 eV. This assumption was based on PL results of the InN films grown by sputtering[34, 35, 36, 37]. However, PL of MBE and MOCVD grown single crystalline InN films indicate much narrower bandgaps of 0.65-0.8 eV. The slight variation in band gap from sample to sample is depending on the background carrier concentration[50]. This section focuses

on the optical properties of InN layers grown at different temperatures. Figure 5.7a shows the low temperature (20K) photoluminescence spectra of InN layers. Here, a 632.8 nm laser was used as the excitation source and the PL spectra were monitored using a monochromator with PbS/PbSe Hamamatsu photodiode detector. The electrical signal from the photodetector was registered using lock-in techniques. The sample grown at 550 ^{o}C shows a much higher PL intensity than the other two samples grown at lower temperatures. The recorded wavelength of 1570 nm corresponds to a band gap of 0.78 eV. This peak position is virtually constant for layers grown at different temperatures. However, a strong decrease in PL intensity is observed for the samples grown at lower temperature. A shoulder in the emission at longer wavelength is also clearly detectable. The origin of the shoulder is not clear but it might be caused by structural defects[163, 185]. This assumption is supported by the broad FWHM values of the PL peaks which reflect structural non-uniformity of the InN films. The large background carrier concentration and the surface electron accumulation hamper the determination of accurate band gap energies of InN. To avoid the effect of back ground electron concentration, further improvement of growth conditions and reduction of dislocation density are required. The investigation of carrier recombination mechanism is another important subject. Figure 5.7b presents the differential transmission decay of InN layers grown at 500 and 550 ^{o}C under an excitation energy density of I=15 μJ/cm^2. The description of the measurement techniques can be found in chapter 3. An exponential decay in differential transmission was observed. From this decay an average carrier lifetime is extracted. An increase in carrier life time from 27 ps to 86 ps was observed as the growth temperature was increased from 500 ^{o}C to 550 ^{o}C. The reduction in the number of the N vacancies with increasing the growth temperature can be attributed to the increase in carrier life time. The recorded carrier life time of 86 ps at room temperature is comparable with state of the art InN layers grown by MBE[186]. This result is analogous to the increase in electron mobility with decreasing carrier concentration (Fig. 5.5a).

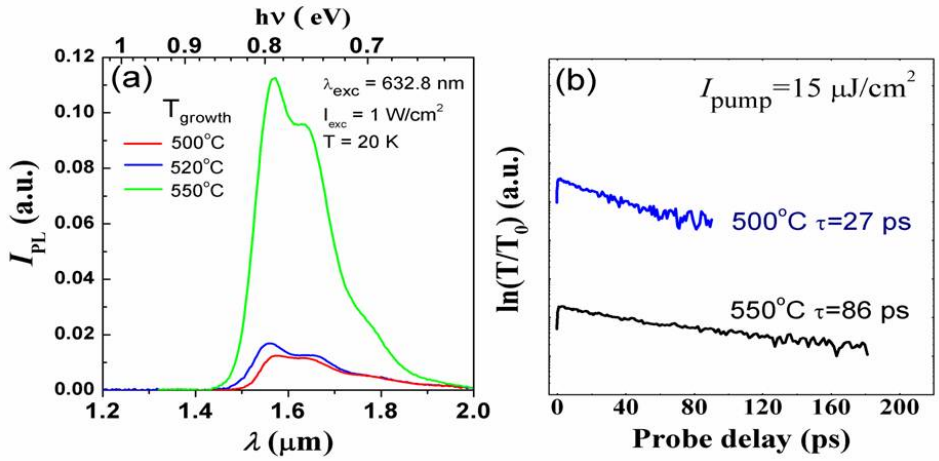

Figure 5.7: a) LT PL spectrum of InN layers. b) Differential transmission of InN layers grown at 500 and 550 ^{o}C (τ refers to calculated carrier life time).

5.2 Growth and characterization of InN grown at different V/III ratio

Limitations in the growth temperature window for InN imposed by the high decomposition temperature of NH_3 and the reduced adsorption of In atoms at high temperature, put an additional importance on other growth parameters like V/III ratio and growth pressure. In this section close attention is paid to the investigation of the influence of different V/III ratios on the structural, electrical and optical properties of InN layer. A series of InN layers was grown on un-doped Ga-polar GaN templates. V/III ratios of 53k, 73k, 80k and 111k were employed keeping all the other growth parameters, i.e. growth temperature of 520 ^{o}C, growth pressure of 600 mbar and NH3 flow of 3 l/min, constant. Only TMIn flow was varied from sample to sample. In general, group V (NH_3) partial pressure is varied to investigate the effect of V/III ratio[187, 188]. In this research, the goal of changing group III (TMIn) partial pressure is to study the effect of excessive In on the formation of In droplets and the other properties of InN. N_2 was used as carrier gas. The thickness of the layers is in the range of 220 nm - 250 nm (110 - 125 nm/hr). The growth process and layer structure for InN is very similar to the one described in section 5.1.

5.2.1 Effect of V/III ratio on InN structural properties and surface morphology

Figure 5.8a illustrates XRD ω-2θ scans of InN layers. The InN (0002) and GaN (0002) peaks are seen clearly and the separation between these two peaks indicates that the InN peaks are fully relaxed. Relaxation of the InN layer is further confirmed by RSM of asymmetric (10-15) XRD reflections. The RSM of an asymmetric reflexes (10-15) for the sample grown at a V/III ratio is shown in the inset of Fig.Fig. 5.8a. The relaxation status of a film can be deduced by comparison of the Q_x values of a layer with respect to a buffer. If an 'a' lattice constant of a layer grown on a buffer is equal to the 'a' lattice constant of the bulk of the same film, it can be inferred that the layer grown on a buffer is fully relaxed. In this work, 'a' lattice constant values of the InN layers were calculated using the RSM of the asymmetric (10-15) XRD reflections. Values in the range of 0.3543 - 0.3547 were found for 'at' lattice constant for InN layer. These values are similar with the 'at' lattice constant for bulk InN (see table 2.1) and therefore, it can be concluded that the InN layers, investigated in this work, are fully relaxed with respect to the buffer layer. As explained before, the large mismatch of 11% between InN and GaN is attributed to this relaxation. A crystalline In droplet (In (10-11)) peak in between InN and GaN peaks starts to appear with decreasing V/III ratio and the intensity of which is rising with further decreasing of V/III ratio. The formation of In droplets is also seen in optical microscope image shown in Fig. 5.8b. One can see the whitish particles which refer to In droplets (as seen before as well) on the sample grown at lower V/III ratio. But there is no indication of these particles on the sample grown at higher V/III ratio (see Fig. 5.8b). Formation of In droplets can be attributed to the lack of reactive N atoms owing to the low growth temperature of 520 ^{o}C. Surface morphology images of InN taken by AFM are displayed in Fig. 5.9. No big difference in RMS values are noted from the images, except for the sample grown at the lowest V/III ratio = 68k. For the first three samples (V/III ratio between 73k - 111k) RMS values are in between 18-19.4 nm. For the sample grown at V/III ratio of 68k, the RMS value increased to 22.4 nm. The observed difference might be due to the thickness of the layer. Due to the uncoalesced grains on the surface, as the film thickness increase,

the roughness of the film increases.

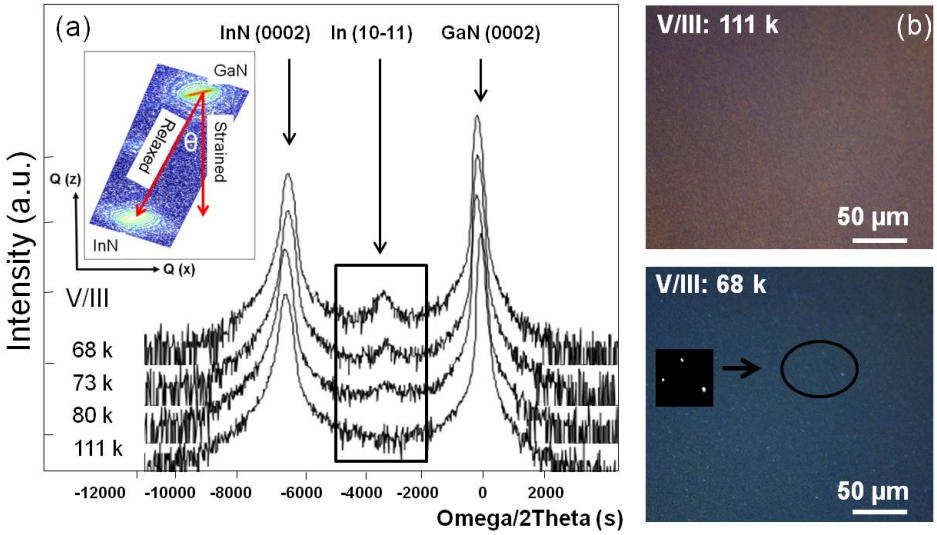

Figure 5.8: a) HR-XRD ω-2θ scans of InN series with V/III variation. b) Optical microscope images of InN layers grown under V/III ratio of 68k and 111k. Black circles on bottom image of (b) mark In droplets.

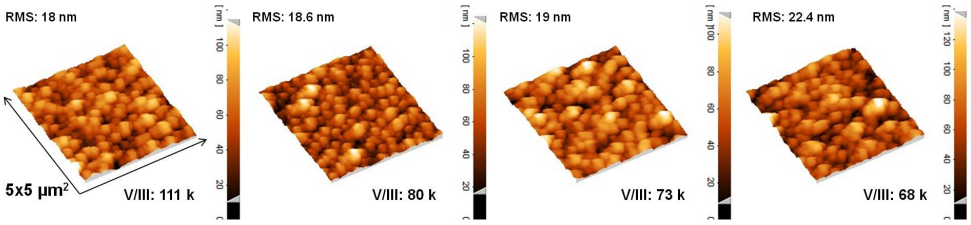

Figure 5.9: AFM images showing surface morphology of InN layers. V/III ratios and RMS values are inserted in the image.

5.2.2 Defect density calculation by XRD

The purpose of this section is to calculate and describe the influence of V/III ratio on dislocation densities. All calculations were performed based on the theory by Srikant et al.[31]. The inset of Fig. 5.10a displays ω-rocking curve measurement results for the sample grown at V/III ratio of 111k. For the sake of simplicity, ω-rocking curve results of only one sample are given. A sharp peak with low FWHM value of 348 arcsec is detected from on-axis (0002) diffraction scans. The off-axis diffractions of

(10-12) and (30-32) yield much broader FWHM values of about 2900 and 4300 arcsec, respectively. The observed difference is not surprising for highly mismatched structures as in our case InN on GaN (11% lattice mismatch). Fig. 5.10a shows the symmetric and asymmetric rocking curve results (symbols) including the fitting curves (solid line) based on Equ. 3.7. proposed by Srikant et al. The variation of the calculated screw and edge dislocation densities as a function of V/III ratio is displayed in Fig. 5.10b. The screw dislocation density which is associated with the tilt between sub-grains and the underlying substrate is in the range of 4.6x10^8 cm^{-2} - 6.2x10^8 cm^{-2}. A small increase in screw dislocation density is observed with decreasing V/III ratio. However, the edge dislocation density which is associated with twist of domains shows an opposite behavior, thus a decrease in edge dislocation density from 2.1x10^{11} cm^{-2} to 1.0x10^{11} cm^{-2} is observed with decreasing V/III ratio from 111k to 73k. The relatively high density of edge dislocation can be associated with the low growth temperature of 520 ^oC. Low growth temperature suppresses the migration of adatoms therefore small grains with high density are forming on the surface. Due to the weak bonding of InN to GaN, these grains are twisted which leads to high edge dislocation density[62]. The decrease in edge dislocation density with decreasing V/III ratio to 73k can be explained by the growth in In-rich region. This results in an enhanced lateral growth rate because an In-adlayer is formed on the surface which enhances the mobility of In atoms; therefore, the number of individually twisted domains is lower. A further decrease in the V/III ratio to 63k leads to an increase in the off-axis X-ray rocking curve values and an accordingly higher edge type dislocation density of 1.35x10^{11} cm^{-2}. The reason for that is not well understood yet.

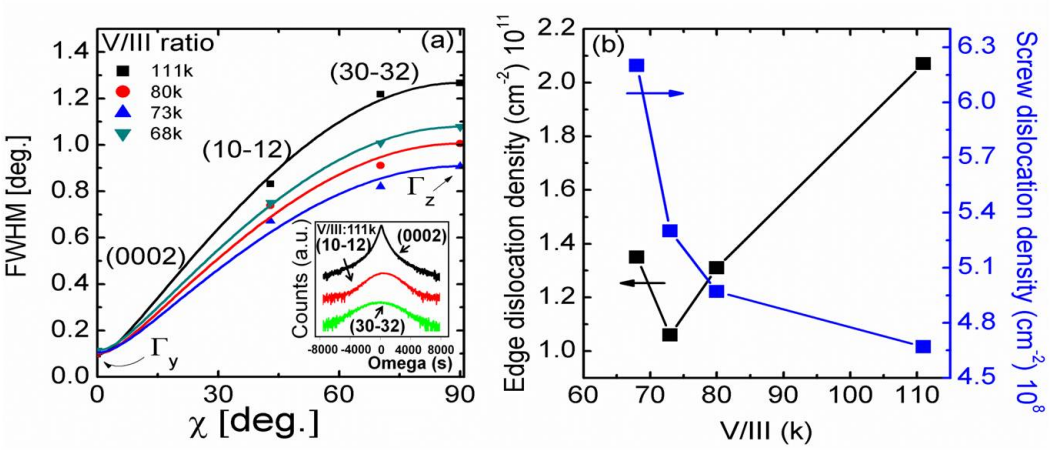

Figure 5.10: Inset (a) On- and off-axis rocking curves for the sample grown at V/III ratio of 111k. (a) Resulting curves of Eq. 3.8 using the FWHM values of rocking curves for the samples grown at different V/III ratios. (b) Variation of edge and screw dislocation densities as a function of V/III ratio.

5.2.3 LT photoluminescence and cathodoluminescence characteristics

In this part, the influence of the V/III ratio on the optical properties of InN layers is analyzed. LT PL and cathodoluminescence (CL) measurements were performed. Figure 5.11a illustrates low temperature PL measurement results of the InN layers grown at different V/III ratios. The spectral position of the InN layers (0.78 eV) is in good agreement with other works taking into account Burstein-Moss effect and free electron concentration in the sample[52, 189, 190]. The decrease in PL intensity with decreasing V/III ratio is caused by an increased screw dislocation density acting as nonradiative centers. The increase in screw dislocation density is asessed by an increase in on-axis (0002) FWHM values with rising V/III ratio as explained in the previous chapter. In addition to the main InN band edge luminescence at around 0.78 eV, some peaks were observed at higher wavelengths (Fig. 5.11a). Since the separation of those peaks are almost identical, it can be concluded that the peaks originate from Fabri-Perot interferences. Observation of these oscillations indicates the high interface quality of the layers. Near band edge luminescence detected from CL (Fig. 5.11b) is

comparable to that from PL measurement. The Inset of Fig. 5.11b shows the tendency of the maximum peak positions in PL and CL with respect to the V/III ratio. A blue shift with decreasing V/III ratio is seen in PL and CL results. The shift is attributed to the increase of carrier concentration at low V/III ratio. The small increase in edge dislocation density causes an increase in carrier concentration[102] and consequently a blue shift due to the Burstein moss shift. As explained in chapter 2, dislocations act as donors due to the Fermi level pinning of the conduction band[104, 105, 106].

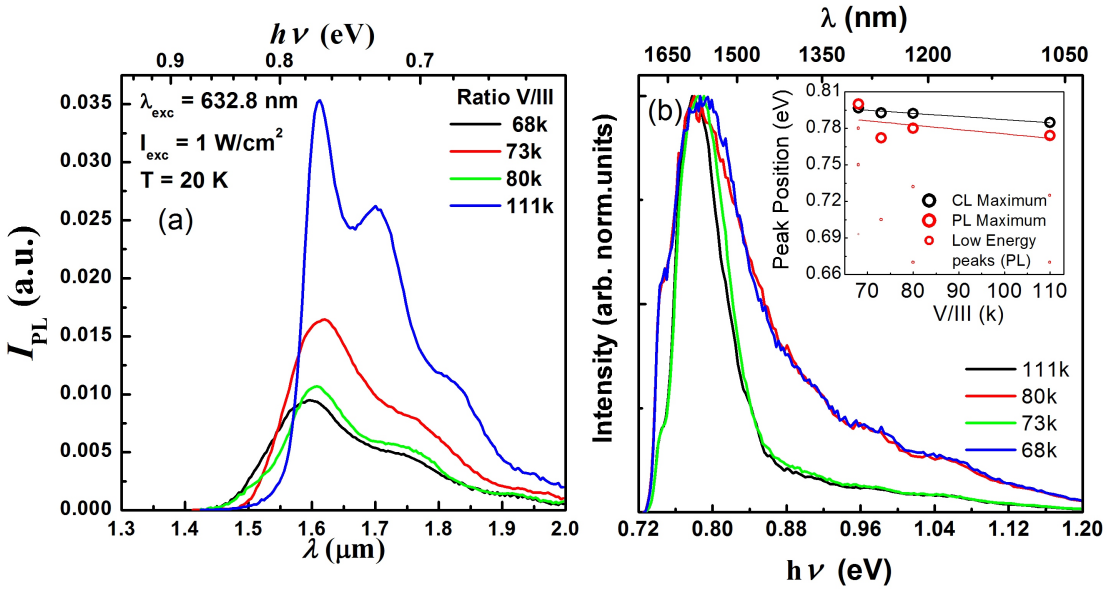

Figure 5.11: a) and b) LT PL and CL of InN layers, respectively. Inset in Fig. b shows the variation of peak position as a function of V/III ratio

5.2.4 Investigation of the influence of V/III ratio on electrical properties of InN

Electrical properties of InN were investigated by means of room temperature Hall Effect measurement, ECV measurement and LO phonon-plasmon coupled mode of Raman spectroscopy. The techniques which have been used in this part were aimed to determine the exact carrier density in InN layers and to allow for a comparison of the results found by these different techniques. Figure 5.12a depicts the variation of the sheet carrier density and the Hall mobility against V/III ratio. An increase in sheet density with

decreasing V/III ratio from 1.3x10^{14} cm^{-2} to 6.0x10^{14} cm^{-2} corresponds to a bulk carrier concentration increase from 6.0x10^{18} cm^{-3} to 2.8x10^{19} cm^{-3}, respectively. This can be associated with the increase of the edge dislocation density[102, 103]. Accordingly, a decrease in carrier mobility from 560 cm^2/Vs to 370 cm^2/Vs with decreasing V/III ratio is found. The decrease in mobility is attributed to an increase in carrier scatterings by defects. Figure 5.12b illustrates the calculated carrier concentration versus depth profile of the sample grown at the highest V/III ratio of 111k. The carrier concentration is calculated using the ECV profile shown in the inset of Fig 5.12b. The negative slope of the CV curve shows that the carriers are electrons. A gradient in carrier concentration from 10^{21} to 10^{19} cm^{-3} is observed within the uppermost 4 nm. The decrease in carrier concentration with depth again indicates the existence of a surface accumulation layer. A sheet carrier concentration of about 9.2x10^{13} cm^{-2} is obtained from the integration of carrier concentration versus depth profile. The sheet density calculated by CV profile is less than the sheet density measured by Hall effect the reason of which was discussed in section 5.1.3.

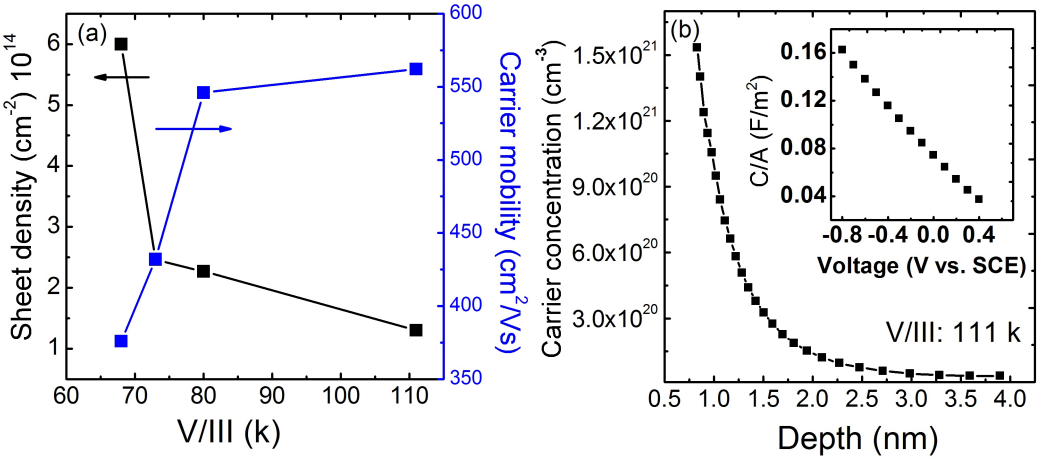

Figure 5.12: (a) Effect of V/III ratio on electrical properties of InN measured by room temperature Hall effect. (b) Calculated carrier concentration variation as a function of depth. Inset in Fig. (b) shows ECV profile of InN grown at the highest V/III ratio of 111k.

The surface electron accumulation and huge density of topological defects on the

surface prevent the determination of reliable bulk carrier concentration in the InN layers by Hall measurement[191]. To eliminate these effects, some sophisticated methods have been used. Moret et al.[191] proposed a theory based on the FWHM value of LT PL measurement. The authors claim is based on the theoretical calculation that a higher carrier concentration causes broadening of the LT PL peak i.e. increasing LT PL FWHM values. The increase in FWHM values with decreasing V/III ratio and accordingly increasing carrier concentration (see Fig. 5.12a) is hence in a good agreement with Morets' theory. Another method is Raman scattering from LO phonon-plasmon coupled modes (LPP). In this method, the shift in the LO phonon band towards the low (high)-frequency side gives an indication about decreasing (increasing) of carrier concentration[151, 150, 192, 193]. Both techniques have also been applied on the investigated samples of this report. Figure 5.13a shows the Raman spectroscopy measurement results of the InN layers grown at different V/III ratios. In backscattering configuration, all allowed modes of E_2 (high) and A_1 (LO) phonons which are expected from the wurtzite crystal belonging to the C^4_{6v} space group were clearly observed together with the very sharp substrate peak. Figure 5.13b displays the variation of the peak position and the FWHM of the Raman E_2 (high) mode as a function of V/III ratio. Sharp E_2 modes with very narrow FWHM values between 6.9 - 7.8 cm^{-1} are observed. The narrow FWHM values are a clear indication of good crystal quality of the layers. The E_2 (high) frequency of 490.1 cm^{-1} of InN was determined using an InN sample which is known to be fully relaxed[62]. This value is a widely accepted reference value for the E_2 (high) mode frequency. If a measured frequency of the E_2 (high) mode is higher than this reference value, it can be accepted as an evidence of compressive strain in the film. In this study, no serious shift in Raman frequency of E_2 (high) (Fig. 5.13b) mode is realized by variation of the V/III ratio. This means that the strain is nearly independent on V/III ratio. In the view of this, the observed very small shift of the Raman E_2 (high) mode compared to the reference value can be attributed to a very small compressive strain of the InN layers on the GaN templates. With rising V/III ratio, a tiny increase of FWHM from 6.9 cm^{-1} to 7.9 cm^{-1} is seen. This increase can be associated with a higher dislocation density at low V/III ratio.

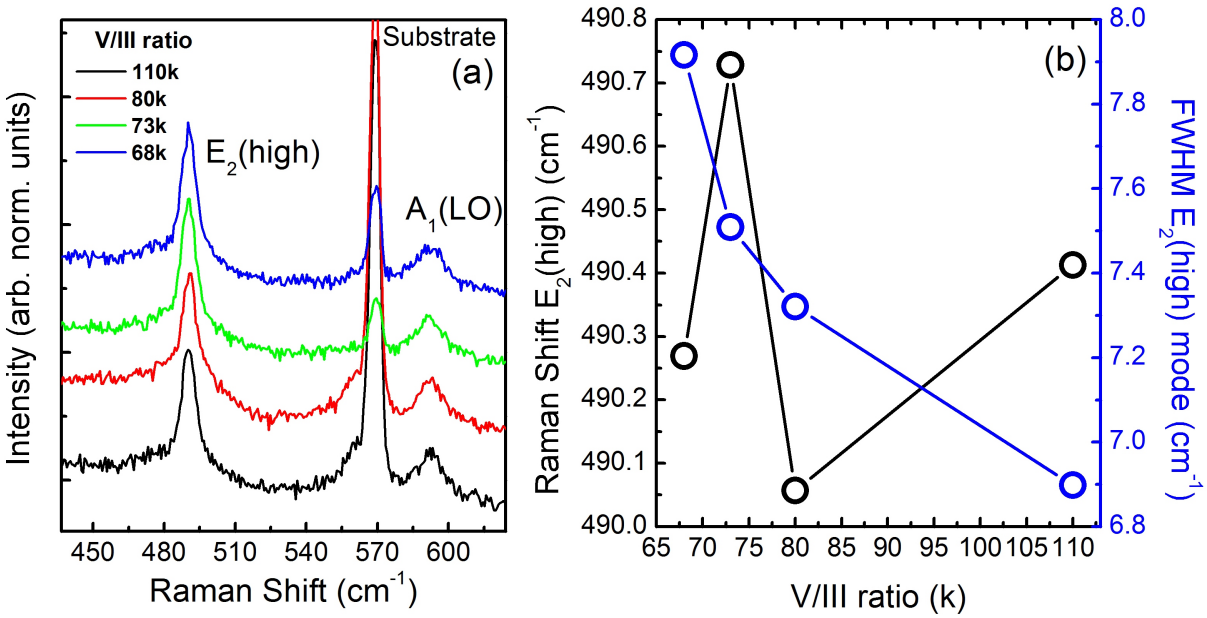

Figure 5.13: a) Raman spectra of InN layers grown at different V/III ratios. b) Raman shift and FWHM of E2 (high) mode as a function of V/III ratio.

In Raman spectroscopy, not only information about the crystal quality and the stress is extracted but also hints about carrier concentration can be deduced. While E_2 (high) mode provides information about the crystal quality and the strain state, it was shown that the polar A_1 (LO) mode can be considered for the estimation of the bulk carrier concentration[151, 150, 192, 193]. Both, a shift from 592.1 cm^{-1} to 593.4 cm^{-1} and broadening of the polar A_1 (LO) mode is observed with increasing V/III ratio as listed in Table 5.1 and as seen in Fig. 5.13a, respectively. This shift and broadening is explained by phonon plasmon coupling as it was observed in GaN and InN before[192, 193].

Table 5.1: a) Raman spectra of InN layers grown at different V/III ratios. b) Raman shift and FWHM of E_2 (high) mode as a function of V/III ratio.

V/III (k)	111	80	73	68
PL FWHM (meV)	76	79	81	100
Position A1(LO)(cm^{-1})	592.01	592.40	592.94	593.4

Based on the equations (3.5) and (3.6)[150], a change of the polar A_1 longitudinal phonon-plasmon modes of LPP+ and LPP- for n-type InN as a function of free carrier concentration is shown in Fig. 5.14a. LPP+ and LPP- modes were evaluated by solving Equation (3.5) for the longitudinal excitation $\epsilon(\omega)$=0. The bulk carrier concentration of InN layers is estimated using the frequencies of the nonpolar A_1 (LO) mode (Table 5.1) and the plot of LPP± mode frequency (Fig. 5.14a). At the lowest V/III ratio of 68k accordingly at A_1 (LO) frequency of 592.1 cm^{-1}, a carrier concentration of approximately 2.0x10^{18} cm^{-3} is found. With increasing V/III ratio to 111k, an increase of the non-polar A_1 (LO) mode frequency to 593.4 cm^{-1} corresponds to a decrease in carrier concentration by a factor of 2-3. As a result, a very low bulk carrier concentration of about 9.5x10^{17} cm^{-3} is predicted. The results are further reinforced by Morets' theory. Moret et al.[191] states (in the referenced study) that the bulk carrier concentration of InN layers can be estimated by just comparing the experimental value of the FWHM of a LT PL spectrum with theory[191]. Figure 5.14b is taken from Morets' paper and the carrier concentration is estimated using this plot. The blue line seen in Fig. 5.14b, which has been drawn[191] by assuming an inhomogeneous broadening parameters B of 0 eV (shown in Fig. 5.14b), is considered for the estimation of carrier concentration.

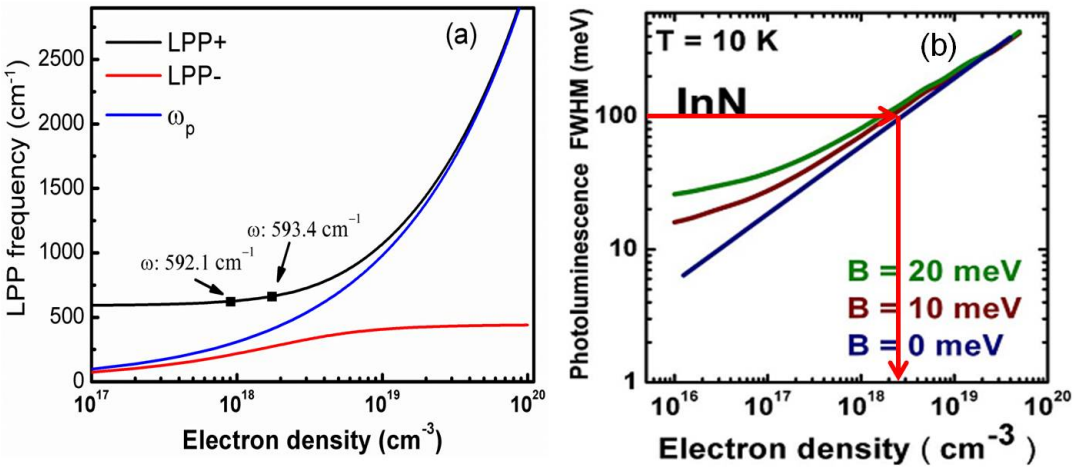

Figure 5.14: a) LOPC mode frequency as a function of carrier concentration. b) Changes in PL FWHM values and A_1 (LO) mode position against V/III ratio. c) LT PL FWHM of InN versus residual bulk doping (taken from[191])

In Table 5.1, the LT PL FWHM values of the investigated InN samples are listed. The arrows in Fig. 5.14b illustrate the FWHM (100 meV) of the sample grown at the lowest V/III of 68k. The corresponding carrier concentration can be deduced from this FWHM value. The carrier concentration of 2-4x10^{18} cm^{-3} estimated by this theory is in a very good agreement with Raman mode results. Carrier concentration values determined by Hall effect, Raman LOPC mode and LT PL are shown in the Fig. 5.15 for a comparison of the results extracted by the different measurement techniques. It is apparent that the carrier concentration evaluated by Raman LOPC mode and FWHM values of LT PL is quite different than the carrier concentration obtained by Hall effect. It is well known that using the Hall effect method one can measure the overall carrier concentration including surface electron accumulation (Fig. 5.12b), the bulk region as well as the interface between layer and substrate[128]. But with these optical techniques, the carrier concentration in the bulk region can be measured more accurately since the penetration depth of the used excitation sources both for PL and RAMAN is high and results are not dominated by the surface of the InN layer. All in all, for the material systems with high surface carrier accumulation and defective

interface, optical techniques and LPP mode of Raman spectroscopy can be considered as an alternative method for the determination of bulk carrier concentration.

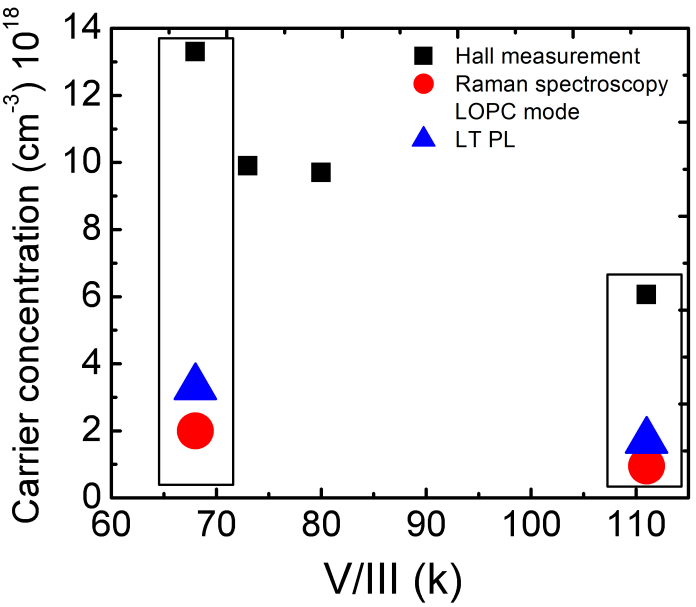

Figure 5.15: Comparison of carrier concentration determined by Hall measurements, Raman spectroscopy and LT PL.

5.2.5 Discussion of InN layer quality

In this chapter, a detailed investigation of MOCVD of InN was given. It was shown that MOCVD growth parameters (growth temperature and V/III ratio) have impacts on the layer properties such as In droplet formation on the surface, electrical and optical properties. As discussed in chapter 2, the growth of InN by MBE is easier than InN growth by MOCVD. In this study, even though the surface of the InN layers is rougher than the MBE grown InN layers (references were given during the discussions in this chapter), other properties like electrical (low carrier concentration and high Hall mobility) and optical properties (optical bandgap) are comparable. Study of the PAS revealed that the growth temperature has an influence on the reduction of the N vacancy concentration in the InN layer. As a result of the growth temperature increase to 550 ^{o}C, no rise in the S parameter was observed. This is an indication of a reduction of N vacancy

concentration by enhancing NH_3 dissociation at high growth temperature. Electrical characterizations results of the InN layers grown at different V/III ratios, which were found by optical techniques (Raman and PL) and Hall measurements, were presented in the last section. Carrier concentrations obtained by those techniques revealed a similar trend with respect to a change of the V/III ratio. However, there is a huge difference with the carrier concentrations obtained by Hall and optical techniques. The carrier concentration found by optical techniques is in the range of $9.0\text{x}10^{17}$ cm^{-3} compared to $6.0\text{x}10^{18}$ cm^{-3} found by Hall measurement. The value obtained by optical techniques is believed to be the lowest value obtained from InN layers grown by MOCVD (to the best of the author). The huge difference is caused by the surface accumulation layer on the InN. Based on this this comparison, it is proposed that for materials with a surface carrier accumulation, optical techniques should be considered for electrical characterizations. With these techniques, one can avoid the surface accumulation effect on the electrical characterization results and achieve a reliable bulk carrier concentration.

6 Growth and characterization of In-rich InGaN alloys

Since 2002, when several researchers started to speak about the 'real' band gap of InN which is 0.65-0.70 eV[194, 53] rather than previously accepted value of 1.9 eV[17, 43, 195, 17], potential applications of InGaN have been extended. For example, the band gap of InGaN alloys which spans a wide range of energies from 0.64 eV (InN) (near-infrared) to 3.44 eV (GaN) (near UV)[196, 197, 46, 198] make this material proper in solar cell technology[199, 200]. InGaN is already in use as active material in high brightness blue/green LED. When yellow and red emission could be obtained by increasing In content in the InGaN MQW, one could achieve monolithic white LEDs by combining blue, green and red emission[201]. Also, due to the narrow band gap and high electron mobility, InN is considered to be a potential material for the fabrication of high-speed and high performance transistors like HEMT[202]. However, growing high quality InN and In-rich InGaN layers remains a challenge due to a large thermal stability difference between InN and GaN, very high equilibrium vapor pressure of nitrogen over InN and high temperature stability of NH_3[203]. In addition, the large difference in inter-atomic spacing between InN and GaN results in a solid-state miscibility gap limiting the InN mole fraction in InGaN layers[203, 119]. This chapter focuses on the growth and investigation of InGaN layers with various In contents ranging from 40% to 85%. The influence of an underlying InN layer on In content in InGaN is studied by growing directly on thin InN interlayer on the GaN templates. This approach can be complementary to growth temperature for increasing In content.

6.1 Growth of In-rich InGaN layers on GaN templates with thin InN interlayer

Deposition processes and layer structures of the studied structures are shown in Fig. 6.1a and b, respectively. Five InGaN layers with In content changing from 40% to 85% were grown on InN interlayer on GaN templates (sample #1-5, Table 6.1.) and was studied as an representative samples. For the InGaN layers, only TMIn partial pressure was varied keeping all the other growth parameters, i.e. growth temperature, reactor pressure, TEGa molar flow (0.87 μmol/min) and NH_3 molar flow (223.3 μmol/min) constant. A surface temperature of 550 ^{o}C was used for both InGaN and InN growth. The reactor pressure was 200 mbar. The TMIn molar flow was varied from 0.50 to 3.50 μmol/min (Fig. 6.1 upper image, sample #1-5, table 6.1). One InGaN layer with the same growth condition as the $In_{0.85}Ga_{0.15}N$ was carried out on GaN template without InN interlayer (sample #7). The aim was to investigate the effect of the InN interlayer on InGaN In content and layer properties. InGaN with 20% In was also grown on GaN at a higher temperature of 720 ^{o}C (sample #8). Only the XPS results of this sample ($In_{0.20}Ga_{0.80}N$) are presented here to have a comprehensive understanding of band bending in the full range of the $In_xGa_{1-x}N$ composition from 20% to 100% In. Finally, one InN layer on GaN template was grown with same conditions as the InN interlayer (sample #6).

6.1.1 Structural and morphological characterization results of InGaN layers and the impact of InN interlayer on In incorporation

Figure 6.2(a) shows XRD ω - 2θ scans of InGaN layers with various In content. The TMIn molar flows and In content (X_{In}) values are noted in the image. A very sharp GaN substrate peak with a very narrow FWHM value of 220 arcsec is seen together with a sharp peak from the single InN layer. Peaks in between InN and GaN are attributed to InGaN layers with different In contents. By varying the TMIn molar flow from 0.50 to 3.50 μmol/min for InGaN growth, various In contents ranging from 40% to 85% (samples 1-5) were achieved. The techniques used to determine the In composition

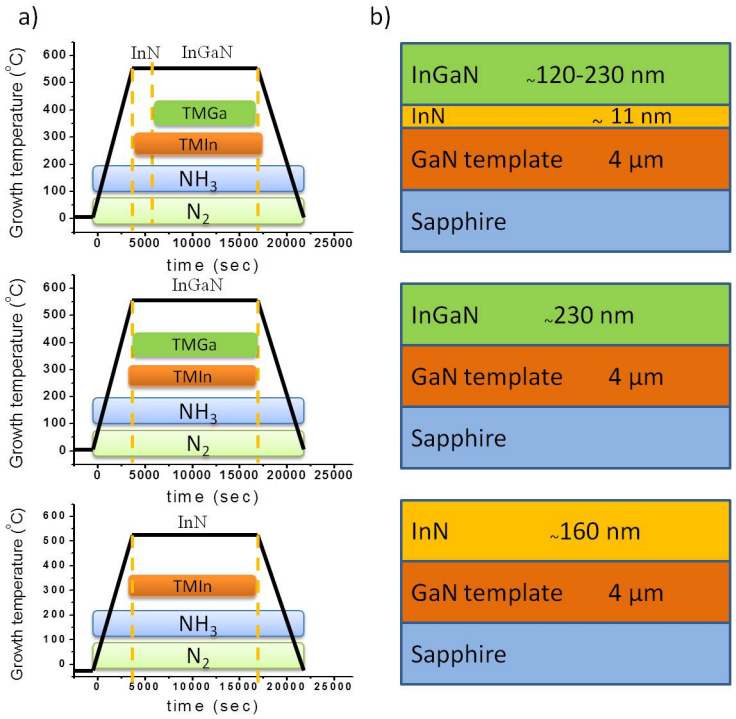

Figure 6.1: a) Deposition process for InGaN and InN layers. b) Layer structures of sample #1-5 upper image, sample #6 bottom image and sample #7 middle image. (Thickness of the layers is noted in the image).

will be discussed later. A decrease in XRD peak intensity is observed in the middle composition range of InGaN (54%). On the other hand, the peak intensity increases with In content lower and higher than mid-range. XRC measurements for symmetric (0002) diffraction were carried out to examine the crystal quality of the InGaN and InN layers (samples #1-5 and #6). In table 6.1, FWHM values of (0002) symmetric diffractions are listed. An increase in FWHM value from 681 arcsec to 2700 arcsec was observed with increasing In content from 40% to 74%. However, for the InGaN layer with highest In content, namely, $In_{0.85}Ga_{0.15}N$ and InN layers, the values decreased to 920 arcsec and 661 arcsec, respectively. By taking these results into consideration, it can be concluded that the crystal quality of the InGaN layers is lower in the middle InGaN composition range. This is attributed to a high degree of atomic disorder and the large atomic radius difference between In and Ga atoms. Alternatively, phase separation detail of which will be discussed during the next section might be another reason for

the decrease in peak intensity[204, 205]. A peak in between $In_xGa_{1-x}N$ (X: 0.85, 0.74, 0.62) and GaN peaks was observed which is an indication of In droplets(Fig. 6.2a). As discussed in chapter 5, formation of the In droplets might be related to the insufficient NH_3 decomposition as a result of the low growth temperature.

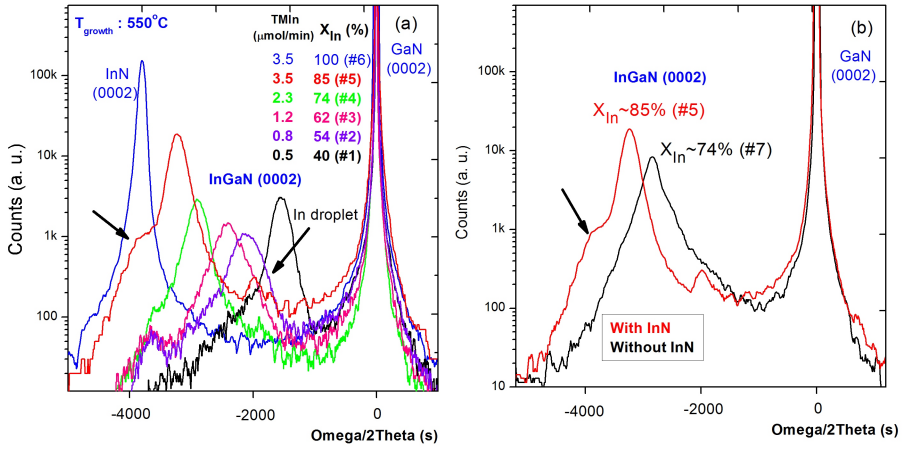

Figure 6.2: a) XRD ω - 2θ scans of InGaN layers with various In contents. b) XRD ω - 2θ scans of GaN/InGaN structure grown with same TMIn partial pressure but with and without InN interlayer.

For an epitaxial layer with a high lattice mismatch to the substrate the strain state is an important property. Relaxation of the layer causes formation of defects and rising of In content by composition pulling effect for InGaN layers[206]. For the strain state investigation of the investigated InGaN and InN layers, RSM for (10-15) diffractions was performed. RSM of (10-15) scans confirmed that all InGaN layers are fully relaxed due to the high lattice mismatch between In-rich InGaN, InN layers and GaN template. As previously mentioned, a thin InN interlayer was included underneath the InGaN layer. Figure 6.2b shows XRD ω - 2θ scans of one InGaN layer with (#5) and without (#7) InN interlayer. In sample #5 a second shoulder-like peak was observed at the position expected for pure InN. This peak is not detected when InN was not included in the structure. The results seem to indicate that there are two different growth mechanisms on InN interlayer and GaN buffer. Due to the initiated strain mode from the very beginning of the InGaN growth on GaN, even though the gradual relaxation of

Table 6.1: Material properties of In(Ga)N samples #1-8 as determined within this study.

ID	X_{In}%	X_{In}%	RMS	GR	FWHM	E_{sF}	E_{bF}	E_g	V_{bb}	$n_b cm^{-3}$	$n_{ss} cm^{-2}$
	XRD	RBS	nm	nm/hr	(0002)	eV	eV	eV	eV	10^{18}	10^{13}
1	40	40	8.5	110	681	2.10	1.95	1.91	0.15	2.9	0.20
2	54	50	25	105	1890	1.94	1.60	1.51	0.34	5.2	0.70
3	63	63	32	108	2550	1.82	1.43	1.30	0.39	6.7	0.88
4	76	74	24	122	2645	1.65	1.18	1.02	0.47	7.2	1.05
5	83	85	21	114	920	1.55	1.09	0.88	0.46	9.5	1.06
6	100	100	10	94	661	1.42	0.84	0.64	0.58	6.2	1.28
7	72	74	-	-	-	-	-	-	-	-	-
8	20	-	-	-	-	2.68	2.65	2.61	0.03	4.1	0.01

InGaN, uniform composition of In through the whole layer is accomplished. However, the growth on InN leads to initiation of a phase separation as either existence of InN or generation of very high composition InGaN in the structure. The comparison of these two samples with (#5) and without (#7) InN interlayer also provides information on the enhancement of In incorporation. Without the InN interlayer, the In content is about 74%, it increased to 85% when the InN interlayer is included. The increase in In content might be explained by In segregation from the InN interlayer to InGaN layer which will be discussed below. The slight decrease in intensity of the XRD peak for the sample grown without InN interlayer might be due to the decrease in In content, which shifts the sample towards the mid composition range with effects as explained before. XRD simulations and RBS measurements were conducted to ascertain the In content in InGaN layers. Relaxation of the layers, which was deducted from XRD RSM of asymmetric (10-15) diffraction, was considered during the determination of the In contents in InGaN layers by simulation of XRD results. The RBS measurement and XRD simulation results of one InGaN layer are shown in Fig. 6.3 and the inset of Fig. 6.3, respectively. Same measurement and simulation were carried out for the other samples as well. In Fig. 6.3b the variation of In content in InGaN as a function

of TMIn molar flow is shown. The results of XRD simulation and RBS measurement techniques were consistent. A linear increase in In content was observed with rising TMIn molar flow. Interestingly, no significant difference was observed in growth rate of InGaN layers when increasing TMIn partial pressure. There is a possibility that the incorporation efficiency of Ga is decreasing with the rise of TMIn flow and therefore the growth rates of the InGaN layers are nearly unaffected. In addition to the determination of In content in InGaN, RBS measurement also give indication about the origine of the increasing In content when grown on InN interlayer. During approximately first 75 nm from the InN/InGaN interface, the In content is higher than the rest of the layer as seen in Fig 6.3a labeled by a circle. The remaining InGaN yielded almost homogeneous In content of 85%. In the RBS measurement (black curve), the slope between InN and InGaN is seen not as sharp as in the RBS simulation (red curve). This can be considered as a hint of In segregation/pulling at the interface from InN interlayer to InGaN and therefore In content is rising. It should be emphasized here that the In content (85%) in the homogeneous part is higher than the In content (74%) in InGaN grown on GaN without InN interlayer. It can therefore be inferred that In segregation occurs through the whole layer but the amount of the segregation is decreasing towards the surface of the InGaN layer.

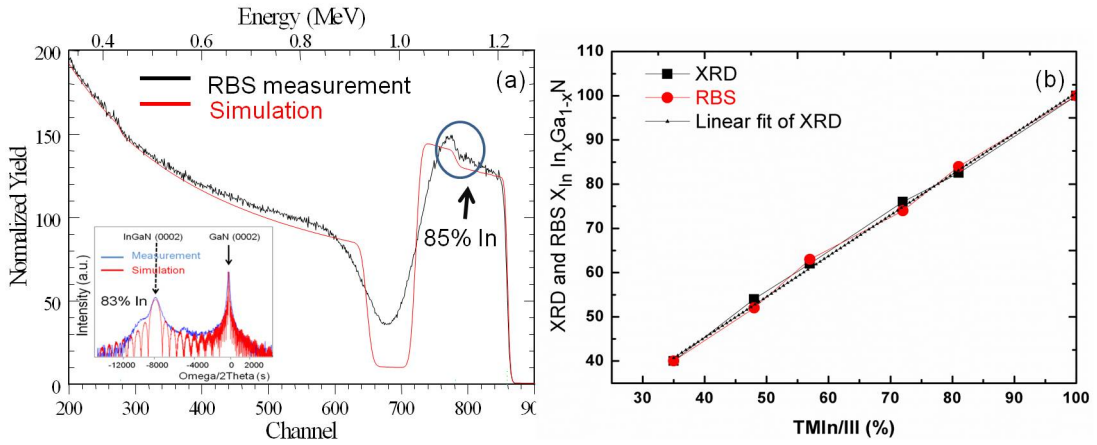

Figure 6.3: a) RBS measurement and simulation result and XRD simulation (inset) for determination of the In content. b) Correlation of InGaN composition from XRD and RBS measurements with gas phase TMIn/III ratios.

In Fig. 6.4, SEM images of InGaN layers with 40%, 63% and 85% In and InN layer are shown. Hexagonally shaped islands are observed on the surface, suggesting that the InGaN layer was grown with the same hexagonal symmetry as InN. The size of these islands becomes larger across the middle of the InGaN composition range. With further increase in In content towards InN, these islands become more uniform and the size becomes smaller. This is due to the fact that in the In-rich region wetting ability is enhanced by thin InN interlayer and provides appropriate nucleating sites. The granular structure of InN and In-rich InGaN is thought to originate from the short migration distance of adsorbed atoms at the low growth temperature. AFM root mean square roughness results are listed in Table 6.1. The roughness of the films is directly correlated with the size of the islands formed on the surface, and the roughness is higher across the middle of the range of InGaN compositions[190].

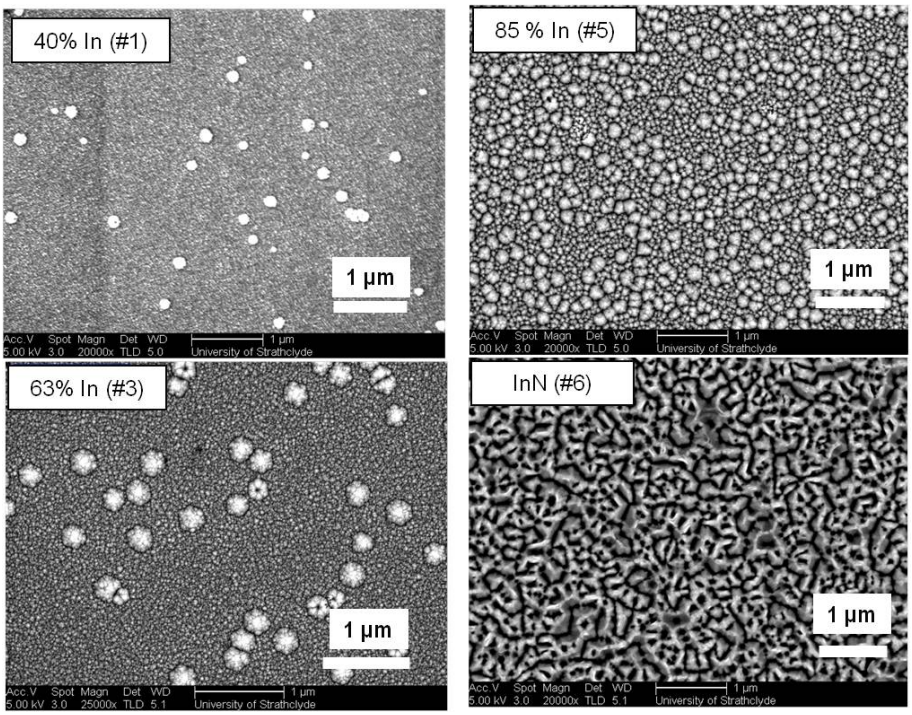

Figure 6.4: SEM plan-view images of investigated InGaN layers.

6.2 Low temperature optical characterization of InGaN layers and observation of phase separation

In Fig. 6.5a LT PL spectra of InGaN layers with In content varying from 100% to 54% determined by XRD are shown. As seen in the inset of Fig. 6.5a, integrated PL intensity decreases by two orders of magnitude with In content decreasing from 100% to 54%. At the same time, the dependence of PL energy on In content variation in InGaN is non monotonic. A decrease in In content from 100% to 76% leads to a shift to shorter wavelengths as expected. However, for further decrease in In content to 62% and 54% a shift to longer wavelengths was observed. A significant broadening of PL is realized with a decrease of In content from 100% to 76%, whereas further decreasing of In to 54% leads to a narrowing of PL spectra. Spectral position of PL of InN layer (0.72 eV) is consistent with other references[46, 198] taking into account Burstein-Moss effect and free electron concentration in the sample. However, the observed inconsistent shift of PL with In content cannot be explained by Burstein-Moss effect, since free electron concentration does not differ significantly in the different samples. Transmittance measurements showed an increase of energy difference between the LT PL spectral position and the RT absorption edge with decreasing In content. In Fig. 6.5b LT PL and RT absorption spectra for samples with 54%, 76% and 100% of In are shown demonstrating the increase of the energy difference with decreasing In content. The detected long wavelength shift in PL with decreasing In content below 76% and increase of energy difference between the LT PL spectral position and the RT absorption edge are caused by increasing degree of localization of photo-generated carriers. Increasing degree of localization of photo-generated carriers depends on phase separation. The phase separation namely formation of In-rich regions with In 54% and In 63% in $In_{0.54}Ga_{0.46}N$ and $In_{0.63}Ga_{0.37}N$, respectively, resulting in local potential minima in the band tail which are dominating the luminescence. Not only phase separation but also inhomogeneous lattice deformation and high density of impurity states could be assigned to the formation of local minima in the band tails. Chen et al.[194] observed similar behaviour from a blue LED structure with a single InGaN active layer. A strong blue-shift with

increasing excitation power was realized which was explained by band filling of local potential minima caused by composition fluctuation in InGaN. The increase in FWHM of PL spectra with decreasing In content up to 76% indicate rising inhomogeneity of InGaN. The homogeneity of the InGaN layers decreasing with further decreasing In content to 54%. The low PL intensity with decreasing In content is caused by increasing concentration of nonradiative defects because of phase separation, high impurity states, and inhomogeneous lattice deformation. InGaN with 40% In did not show a visible PL peak probably because of a high concentration of nonradiative centers. These results are consistent with XRD results. The decrease in XRD peak intensity and the large FWHM values in the middle of the InGaN composition range might be due to phase separation as well as high defect density. Chang et al. presented similar results[207]. In their work, a phase separation is observed in an InGaN layer with 80% In but for InGaN with higher In content of 92% and 98%, there is no phase separation measured by LT PL measurements results.

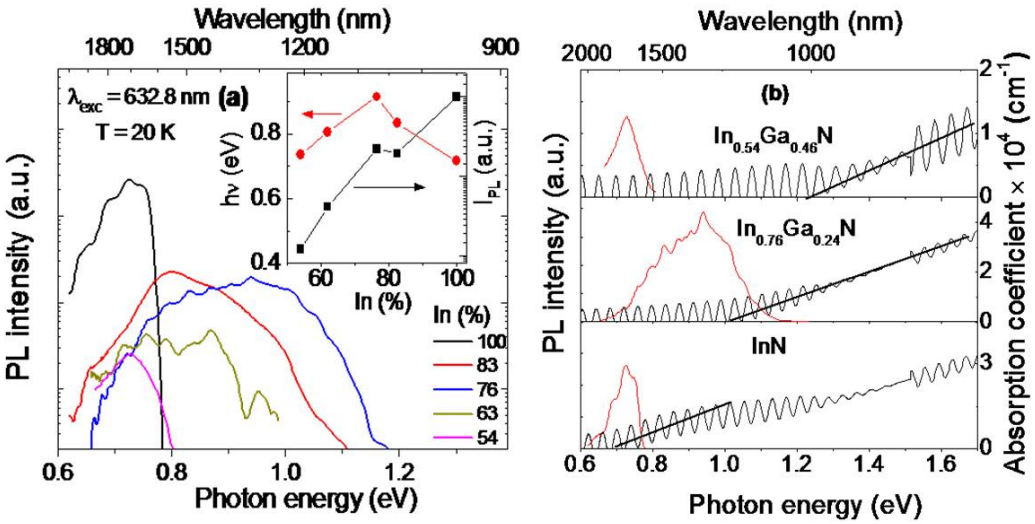

Figure 6.5: a) LT PL spectra of InN and InGaN layers. Inset shows dependences of PL spectral position and PL integral intensity on In content; b) LT PL and RT absorption spectra for InGaN layers with different In contents demonstrating increasing energy difference between PL spectral position and the absorption edge with decreasing In content.

6.3 Surface electronic properties of In-rich InGaN alloys by XPS and IR reflectivity measurements

Both MBE and MOCVD grown In-rich InGaN layers show a large electron accumulation at the surface. The location of the surface Fermi level (E_{sF}) which is below the charge neutrality layer in the conduction band results in a surface electron accumulation layer. The existence of the electron accumulation makes the electrical characterization of these materials very challenging[208]. Constant-field Hall effect measurements are influenced by parallel conduction owing to the high carrier concentration at the interface and in the surface space charge region. Therefore, Hall measurements would overestimate the InGaN bulk layer carrier concentration. In this study, the carrier concentration has been determined from IR reflectivity measurements based on the conduction electron plasma frequency (Eq. 6.1) using a non-parabolic band structure approximation[209].

$$\omega_P^2 = \frac{4ne^2}{\epsilon_0 \epsilon_\infty \langle m^*(E) \rangle} \tag{6.1}$$

Here, ω_p is the free electron plasma frequency, e^- is the electron charge, is the density of states averaged band edge electron effective mass[209], ϵ_0 and ϵ_∞ are the vacuum permittivity and high frequency dielectric constants, respectively. The electron sheet density (electron accumulation) (n_s) has been determined by space charge calculations using Poisson's equation[72] within the modified Thomas-Fermi approximation (MTFA)[210, 211]. For this calculation, the E_{sF} and bulk Fermi level (E_{bF}) were needed. E_{bF} was determined from IR reflectivity measurements and Fermi-Dirac statistics. E_{sF} was determined by XPS using an Omicron SPHERA 125 Spectrometer. The theory and the calculations can be found at ref.[121]. The layers studied here were exposed to air after growth and therefore, Oxygen (O) contamination on the surface is inevitable. Before any measurements were performed, the existence of the native oxides on the surface of $In_xGa_{1-x}N$ was proved by XPS measurement. Figure 6.6a demonstrates XPS wide energy scan from one InGaN layer. Oxides peak (O 1s) together with Carbon (C 1s) was detected from as loaded $In_{0.63}Ga_{0.37}N$ sample. In order to get rid of oxide on the surface, the samples were subjected to HCl etching and insitu annealing. HCl

etching involved dipping the sample into a solution of HCl (10 mol/l) for 60 s, followed by rinsing in deionized water and immediately blowing it dry in N_2 before loading it into the vacuum chamber. Following by these steps, in order to thermally desorb the native oxide the samples were annealed in Vacuum at 300 ^oC for two hours. After this cleaning process without taking the sample out, the same XPS measurement was carried out and the result is shown in Fig. 6.6b. Huge reduction in oxide (O 1s) as well as in carbon (C 1s) peak intensities was observed. This means that a decrease in O and C contamination from the surface of InGaN layer was achieved by this cleaning method. The result is further reinforced by core-level spectroscopy measurement for 1 Os core-level. The measurement was performed on $In_{0.63}Ga_{0.37}N$ layer used for XPS measurement and the result is shown in Fig. 6.6c. O 1s peak consists of components at 532.2 eV and at 530.4 eV arise from incidental oxygen and In-N bonding, respectively. The Oxygen and In-N peaks were detected on both untreated and cleaned samples as seen in Fig. 6.6c. However, after surface treatment $\geq 75\%$ reduction of the oxide layer was achieved. The core-level spectra from the other $In_xGa_{1-x}N$ alloys exhibit similar behavior and a reduction in oxygen coverage as a result of cleaning was obtained. The Oxygen contamination is one of the reason for high surface carrier accumulation on the InN and In-rich InGaN alloys[212]. For the determination of the E_{Fs} position, valance band (VB) edge XPS spectra were performed. The photoemission spectra as function of the binding energy is shown in Fig. 6.7. The extrapolation of a linear fit to the leading edge of the valance band photoemission gives the position of the E_{Fs}. With increasing In content a red shift yielded. The E_{Fs} for InN is 1.42 eV above the valence band maximum (VBM) and it increases to 2.68 eV for $In_{0.20}Ga_{0.80}N$, as listed in Table 6.1. This change is monotonic with alloy composition and similar behavior has been previously observed at n-InAlN[213] and n-InGaN[214] grown by plasma assisted molecular beam epitaxy. To determine the position of the E_{bF}, infrared reflectivity with modeling was carried out. The results were further confirmed by using Hall Effect measurement results and Fermi-dirac statistics. The experimental and simulated infrared reflectivity spectra are presented in Fig. 6.8. The oscillations observed in the experimental spectra are due to Fabry-Perot interferences, corresponding to the total film thickness. Calculation using

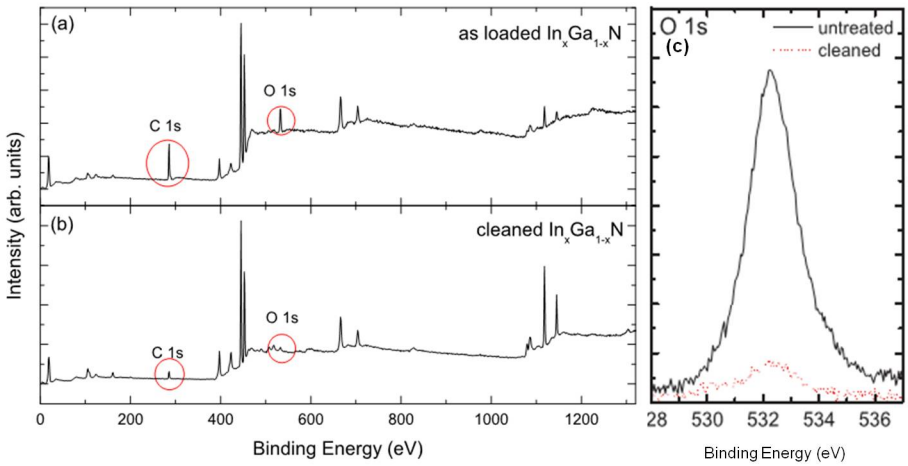

Figure 6.6: XPS wide energy scan on $In_{0.63}Ga_{0.37}N$ (hν = 1486.6 eV) for a) as-loaded film and b) cleaned film. The binding energy scale is with respect to the Fermi level E_F. c) O 1s core-level spectra recorded from an untreated (solid line) and a cleaned (doted lines) $In_{0.63}Ga_{0.37}N$ layer[121].

Fermi-Dirac statistics were undertaken to determine the carrier concentration and the position of bulk Fermi level from the measured conduction electron plasma frequency. This procedure is described in references[121, 208, 215]. Using these calculated and measured values listed on Table 6.1, the effect of InGaN composition on band bending and the amount of surface carrier accumulation is investigated.

Figure 6.9 shows the VBM, conduction band minimum (CBM), and surface and bulk Fermi level as a function of composition referenced to the charge neutrality level (CNL). The CNL is the energy level donating the boundary between surface states that are predominantly donor-like (below) and surface states that are predominantly acceptor-like (above) [72]. The E_{bF} position located below the E_{sF} leads to downward band bending which increases with larger separation between E_{sF} and E_{bF}[216]. The surface and bulk Fermi level positions of $In_xGa_{1-x}N$ alloys with the composition x>0.40 are located below the CNL indicating the existence of unoccupied donor like surface states. In order to maintain the charge neutrality, downward band bending of the bands relative to the Fermi level occur and as a result an accumulation of electrons at the surface. See chapter 2 for more information. Additionally, the surface and bulk Fermi levels

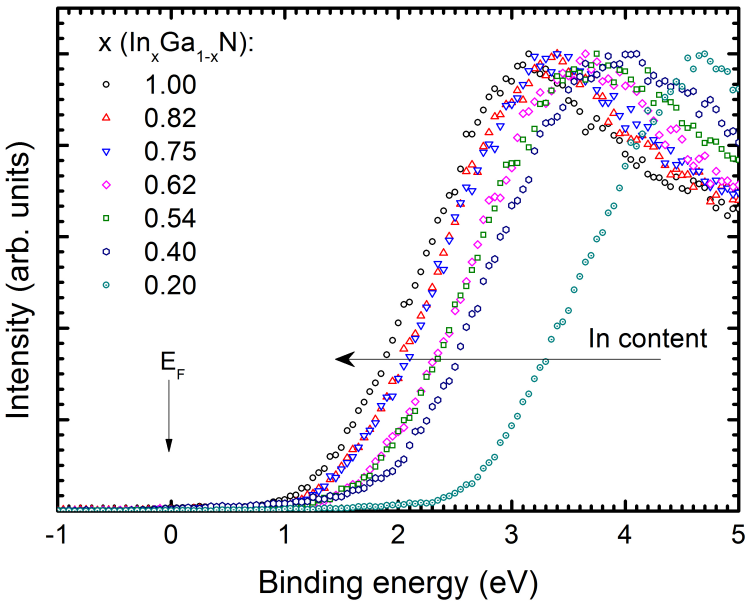

Figure 6.7: Valence band photoemission spectra with respect to the Fermi level (E_F) of $In_xGa_{1-x}N$ alloys across the composition range.

move closer together with increasing Ga content, reducing band bending from 0.58 to 0.15 eV and hence reduction of electron accumulation at the surface (Table 6.1). Further increase in Ga fraction changes the position of surface Fermi level to be located above the CNL causing some acceptor states to be occupied and hence indicating a surface electron depletion layer. It can be seen for the $In_{0.20}Ga_{0.80}N$ alloy that the surface Fermi level is located at 0.44 eV above the CNL. However, the bulk Fermi level for this alloy is situated slightly below the surface Fermi level, consequently the small downward band bending of 0.03 eV (Fig. 6.10a) and residual surface accumulation layer is present (Fig. 6.10b). As seen in Fig. 6.10b, a large electron accumulation has been observed for InN, consistent with previous observations[208]. The surface electron density changes from 1.28x10^{13} cm^{-2} (InN) to 1x10^{11} cm^{-2} ($In_{0.20}Ga_{0.80}N$) given in Table 6.1. This confirms the existence of an electron accumulation layer in the InGaN layer and that the amount of accumulation is larger in In-rich $In_xGa_{1-x}N$ layers. For the $In_{0.20}Ga_{0.80}N$ alloy, the small band bending of 0.03 eV indicates that the transition from an accumulation layer of In-rich $In_xGa_{1-x}N$ to a depletion layer. Nevertheless, within the error bars the surface and bulk Fermi levels could be located in the same

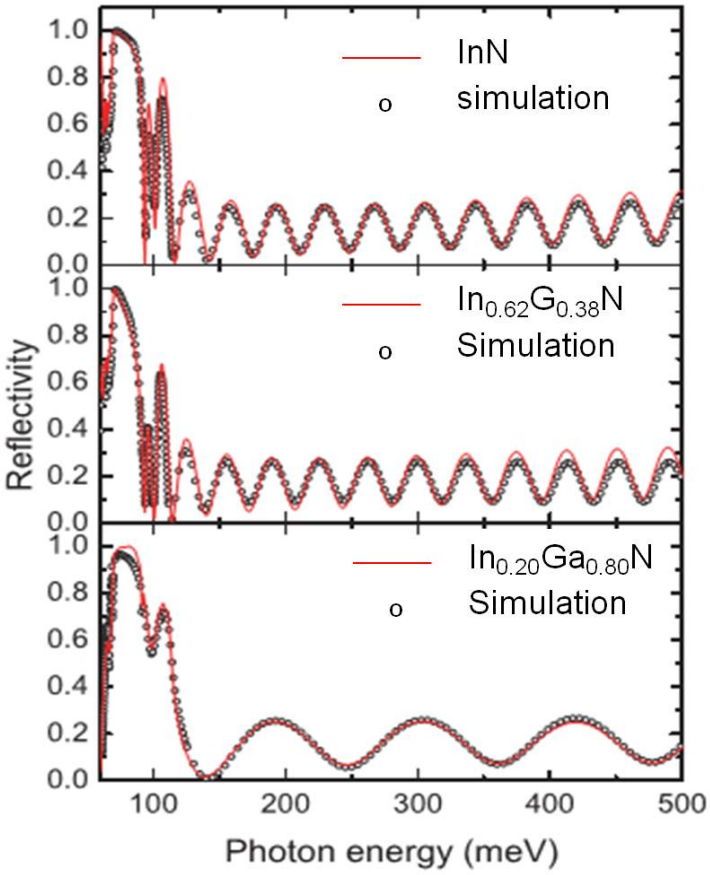

Figure 6.8: The experimental infrared reflectivity spectra for InN, $In_{0.62}Ga_{0.38}N$ and $In_{0.20}Ga_{0.80}N$ with the simulated spectra.

position and consequently the presence of flat band is highly possible. These results indicate that the position of bulk Fermi level plays a very important role in surface electronic properties of semiconductors, and the transition from an accumulation layer of In-rich $In_xGa_{1-x}N$ to a depletion layer at the surface is at a composition slightly less than x = 0.20 for these samples. The bulk carrier concentration is monotonically decreased with decreasing In content as shown in Table 6.1.

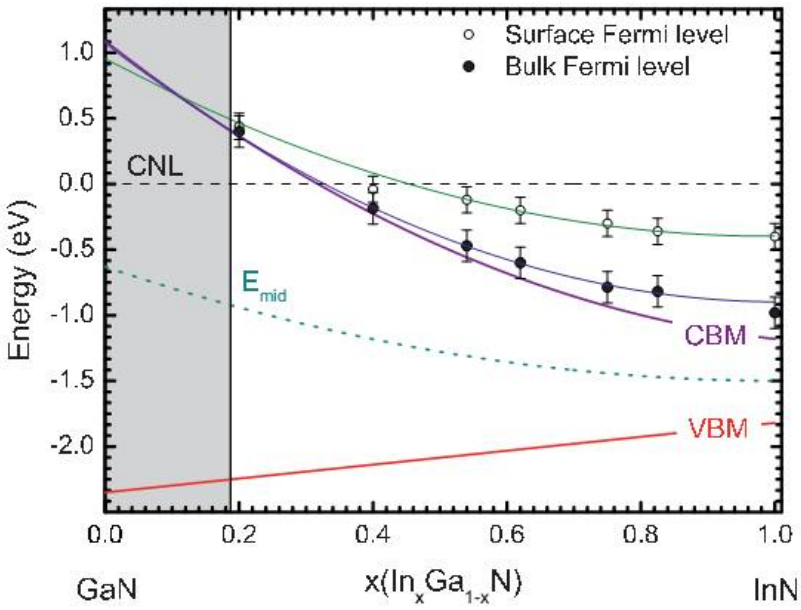

Figure 6.9: The CBM, VBM, and mid-gap position (E_{mid}) as a function of $In_xGa_{1-x}N$ composition with respect to the charge neutrality level (CNL). The relative positions of the surface and bulk Fermi levels, determined by XPS, Hall effect measurements, and infrared reflection, are also shown as open circle and circle points, respectively. The shaded area denotes the compositions for which the $In_xGa_{1-x}N$ alloys exhibit electron depletion at the surface.

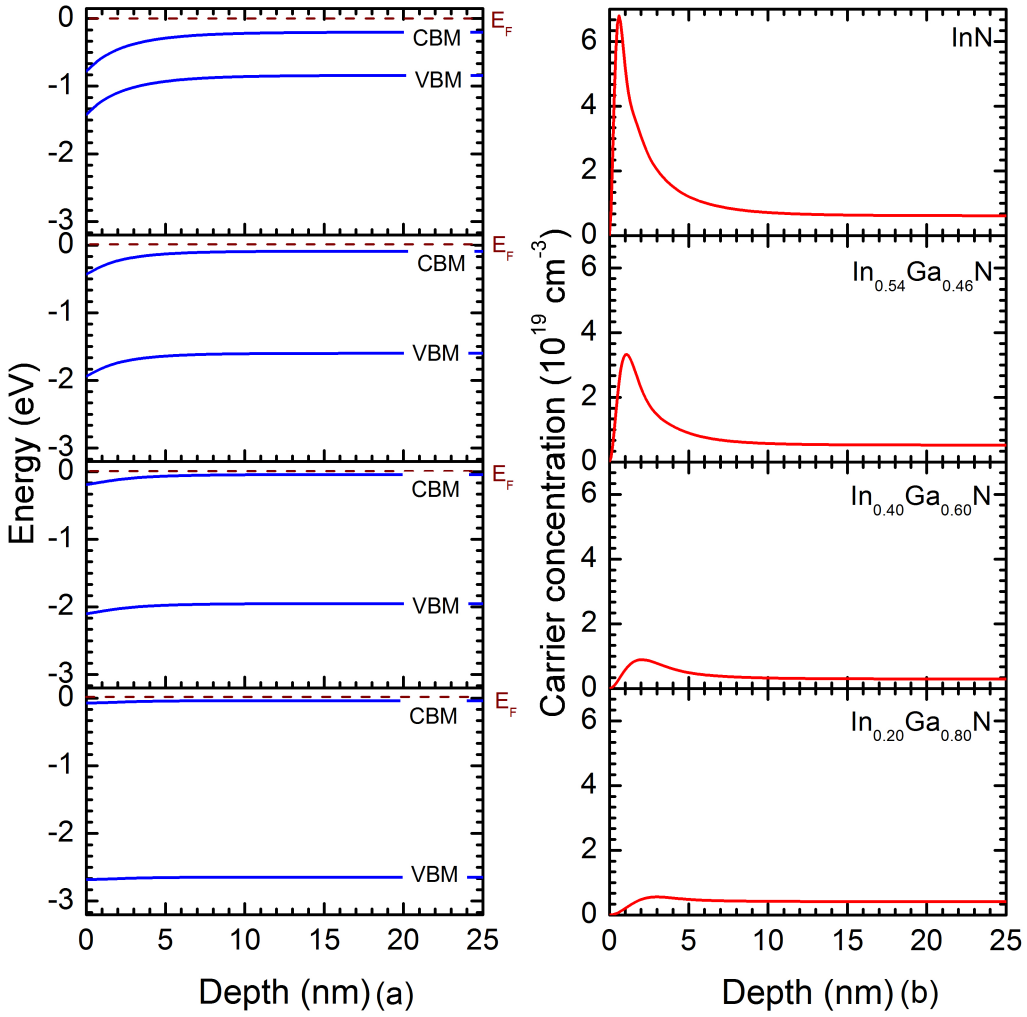

Figure 6.10: The band bending (a) and carrier concentration (b) as a function of depth from the semiconductor surface for InN and $In_xGa_{1-x}N$ (X: 0.54, 0.40, and 0.20).

6.4 Summary and discussion of In-rich InGaN layer properties

In this chapter, $In_xGa_{1-x}N$ layers with various In content were grown and investigated. A new method was proposed in order to enhance the In incorporation in InGaN layer.

This method based on growing InGaN directly on thin InN interlayer on the GaN templates. This approach can be complementary to growth temperature for increasing In content. With this method In incorporation was enhanced by In segregation from thin InN interlayer to the $In_xGa_{1-x}N$ layer. Band bending and the related surface electron accumulation was investigated. A decrease in surface electron accumulation was observed with increasing Ga content, and the transition from an accumulation to a depletion layer was observed at X_{In}=20%. By wet etching in HCL and subsequent annealing in vacuo helped to reduce the native oxide on the surface of InGaN layers. A reduction of the oxide layer greater than 75% was achieved.

7 Growth and Structural, Optical and Electrical characterizations of Mg-Doped InGaN layers

InGaN, like other III/V nitride semiconductor compounds, is a promising material for electronic and optoelectronic devices[217]. Especially for multi-junction tandem solar cells, InGaN is a very attractive material since its bandgap can theoretically be tuned from 0.7 eV to 3.4 eV by changing its composition[218]. p-Type GaN is widely used as a hole injection layer for blue and green LEDs[219, 220, 221]. For the active layer in blue LEDs, InGaN QWs with an In composition of about 16% are required. Although the p-type GaN is grown at relatively higher temperature compared to the InGaN QW, the thermal degradation of the InGaN QW is not too much[219, 220, 221]. However, the required high growth temperature (950 ^{o}C) of p-type GaN makes it inappropriate for devices like solar-cells, green laser diodes, yellow and red LEDs. The active layers of those structures have to be grown under In-rich conditions[222, 223, 224], with In content over 30%. Therefore, the growth temperature has to be kept at low values to enhance the In incorporation. In addition, compulsory high temperature ($\approx$1000 ^{o}C) post annealing, which must be employed to activate Mg acceptors, potentially leads to a degradation of the structural and optical properties of the active layer, and thus, results in a reduction of device efficiency[225]. The degradation can be caused by In segregation from InGaN QW and by formation of In-rich regions in the InGaN layer at higher temperatures[223]. The low-temperature growth of Mg-doped InGaN makes it

an attractive alternative to the p-type GaN, particularly in mentioned devices such as green laser diodes and long-wavelength emitters. In addition, due to the relatively lower Mg activation energy in InGaN:Mg, the high temperature annealing for Mg activation is not required. Therefore, degradation caused by annealing can be avoided. Moreover, low activation energy E_A promotes large hole concentrations which lead to higher conductivity and to lower contact resistance for p-type material [217]. However, due to the presence of a large background electron concentration and a high defect density in InN and In-rich InGaN, realizing p-type material is highly challenging. A comprehensive investigation is required to figure out the Mg doping mechanism for InGaN, with the aim of optimising p-type doping in InGaN. This chapter is devoted to the synthesis and systematic study of structural, optical and electrical properties of Mg-doped $In_xGa_{1-x}N$ layers. At first, $In_xGa_{1-x}N$ (X_{In}: 0.18, 0.17, 0.09) layers doped with different Cp_2Mg flows will be examined. The influence of Mg doping level on structural, morphological and optical properties will be given. Afterwards, electrical properties, which were studied by means of C-V measurements, will be discussed. Following this, structural and electrical properties of Mg-doped In-rich $In_xGa_{1-x}N$ layers with various In contents of X_{In}: 0.30, 0.50, 0.79 and 1.0 will be studied.

7.1 Growth of Mg-doped $In_xGa_{1-x}N$ layers on GaN templates

A series of Mg-doped InGaN layers with thickness of about 55∓1 nm were grown on GaN templates. The GaN templates are slightly n-type doped and the doping level is in the range of 5.0x10^{17} cm^{-3}. The process and layer structure was the same as for undoped layers (see middle image in Fig. 6.1c). Cp_2Mg was used as the Mg precursor. Mg doping concentrations were measured by SIMS. For this growth series, only the Cp_2Mg flow was varied. All the other growth parameters, i.e. growth temperature, growth pressure, TMIn, and TEGa partial pressures, and NH_3 flow were kept constant. N_2 was used as carrier gas. In contents, listed in Table 7.1, were determined by a comparison of XRD ω - 2θ measurement results with simulations. In order to activate

Table 7.1: Details of the growth parameters and a summary of thecharacterization results of $In_xGa_{1-x}N$:Mg layers. Indium content in InGaN, X_{In}, growth temperature, T_{growth}, flows of MO precursors, TMIn, TMGa, Cp_2Mg, ammonia flow, NH_3, and root-mean square roughness, (RMS) are included.

ID	Mg conc.	X_{In}	T_{growth}	TMIn	TMGa	NH_3	Mg/III	RMS
	$cm^{-3}10^{20}$	±0.5%	$^oC \pm 1$	$\mu mol/min$	$\mu mol/min$	$\mu mol/min$	%	nm
I	0.7	0.18	710	3.7	1.8	178	1	5.1
II	3.8	0.18	710	3.7	1.8	178	3	5.3
III	7.3	0.17	710	3.7	1.8	178	5	5.6
IV	9.2	0.12	710	3.7	1.8	178	7	6.2

the Mg acceptor in the InGaN:Mg, the samples were annealed at 750 ^{o}C in N_2 ambient. The total annealing time, including heating up and cooling down, is 60 minutes. This includes about 30 minutes of pure annealing time at 750 ^{o}C. More information about the growth parameters can be found in Table 7.1.

7.2 Influence of Cp_2Mg flow on structural and morphological properties of $In_xGa_{1-x}N$ layers

Figure 7.1 depicts XRD ω - 2θ scans of the $In_xGa_{1-x}N$:Mg layers grown at different Mg acceptor concentrations. The expected InGaN (0002) peaks and sharp GaN (0002) peaks are observed. The measured Mg acceptor concentrations and extracted In contents for all samples are noted in Table 7.1. There is a change in In content for different Mg doping levels. For the first three samples, the determined In contents are about 17%-18% within 0.5% error. For sample IV, the In content is about 12%∓0.5%. There are some shoulders to the peaks, shown by arrows in Figure 7.1. These shoulders might be caused by deformation of the crystal structure by Mg doping or might be an indication of phase separation in InGaN.

The influence of Mg doping level on the phase separation in InGaN:Mg is analyzed by performing RSMs on asymmetric (10-15) diffraction (see Fig. 7.2). The

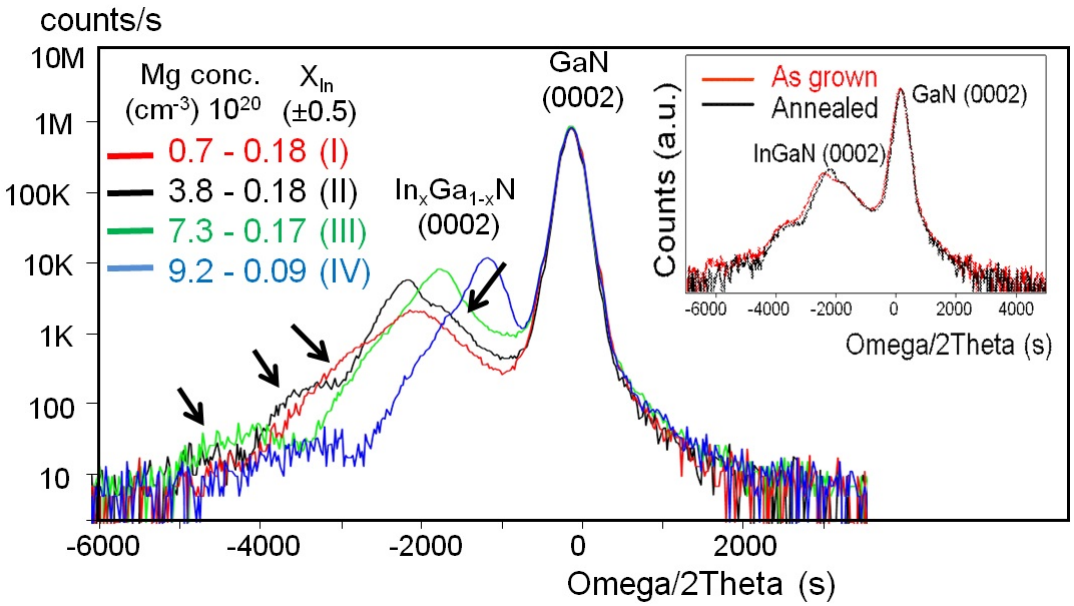

Figure 7.1: XRD ω - 2θ scans of as-grown InGaN layers grown under different Cp_2Mg partial pressures. Inset shows the XRD ω - 2θ scans of an InGaN:Mg layer before and after annealing.

asymmetrical RSMs contain information on both in-plane and out-of-plane lattice constants, from which the In composition and degree of strain relaxation can be estimated independently[226, 227, 228]. The X-axis on the RSM is labeled Qx and the y-axis is labeled Qy. Qx and Qy are correlated with in-plane and out-of-plane lattice constants, respectively. For sample (I) which was doped with the lowest Mg concentration, the RSM exhibits a single diffraction peak related to InGaN. Concerning the Qx value of InGaN:Mg relative to the Qx of GaN, it can be inferred that the InGaN:Mg layer is nearly lattice matched to the underlying GaN layer (blue lines indicate fully lattice matched condition and red lines indicate the position(s) of InGaN layers). Interestingly, as the Mg concentration increases, the InGaN diffraction peak starts to split (sample II*, III, and IV). (*In RSM result InGaN peak position for second layer is different to the others with respect to the GaN peak. This is related to the measurement techniques which do not influence the results). Two well separated InGaN peaks along the growth direction were realized for the sample which was doped with the highest Mg acceptor concentration (sample IV). The two well separated peaks indicate a phase separation

along the growth direction. It can be seen in the RSM of sample IV that one InGaN layer (labeled as InGaN (1)) is fully strained to the underlying GaN layer (same Qx values). For the case of the InGaN (2) layer, it is partially relaxed (different Qx values). The relaxation percentage of the InGaN layers was considered during the determination of In content from the XRD simulation[133]. According to theoretical calculations based on a valence-force-field (VFF) model, phase separation depends not only on the thickness and In composition but also on the strain state in the InGaN films[228, 229]. Taking this fact into account the effect of Mg on strain should be analyzed. The covalent radius of Mg atoms (0.130 nm) is larger than that of Ga atoms (0.126 nm) [230]. It can be proposed that the compressive strain would be increased by the incorporation of Mg atoms into InGaN. With increasing Mg doping level, the compressive strain will be further increased. However, above a critical thickness, the strain will relax. Such a variable strain state with film thickness leads to phase separation along the growth direction[228]. Phase separation with increasing Mg acceptor concentration was also observed by Sang et al.[228]. The authors reported no phase separation from undoped $In_{0.08}Ga_{0.92}N$ layers but found strong broadening of InGaN peaks and phase separations from the samples which were doped with increasing Mg concentration.

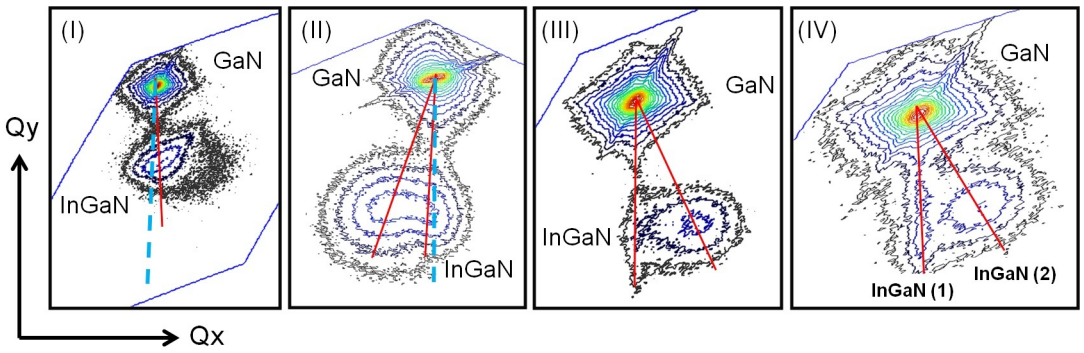

Figure 7.2: XRD RSMs of InGaN:Mg layers. RSMs were performed for the asymmetric diffractions of (10-15).

The inset in Figure 7.1 demonstrates the spectra of the ω - 2θ scans on the annealed and as-grown samples for sample (II). The diffraction peak of the annealed sample deviates slightly from the peak of the as-grown sample. This evidences that the In content

of InGaN is mildly changed after annealing. Due to the weak bond strength between In and N, desorption of In atoms is inevitable after annealing at high temperature. It must be pointed out that there is no degradation in crystal quality; no decrease in XRD peak intensity and no broadening of the InGaN peak yielded by XRD after annealing. Deng et al.[231] have also investigated the effect of annealing on InGaN properties. A higher temperature of 800 ^{o}C and a shorter time of 10 min were employed for annealing. Similarly a slight reduction in In content was observed after annealing. The comparison of the annealing conditions of this study and that of Deng's lead us to conclude that the differences in growth conditions have an effect on the stability of InGaN layers[231]. AFM surface morphology results of InGaN:Mg layers are shown in Fig. 7.3. The RMS values are noted on each image. The RMS of the layers is increasing from 5.1 nm to 6.2 nm with rising Mg doping concentration from 7.0x10^{19} cm^{-3} (sample I) to 9.2x10^{20} cm^{-3} (sample IV). This increase is believed to be associated with the increase in sizes of the In clusters, which are labeled by circles on the surface. With careful consideration of AFM surface morphology and XRD ω - 2θ measurement results, it might be deduced that the decrease in In content from 18% (sample I, II and III) to 12% (sample IV) has a relation with cluster formation and cluster size. It is possible that once In droplets form on the surface, they grow bigger by accumulation of In atoms. Therefore, the incorporation of In atoms in the crystal structure decreases, resulting in a decrease in In content in InGaN. In addition, during this work it was found that the influence of rising TMIn partial pressure on the growth rate of InGaN is too low due to formation of In droplets. All in all, the observed strong decrease in In content might not only be due to the strong phase separation, but might also be due to the formation of In clusters on the surface.

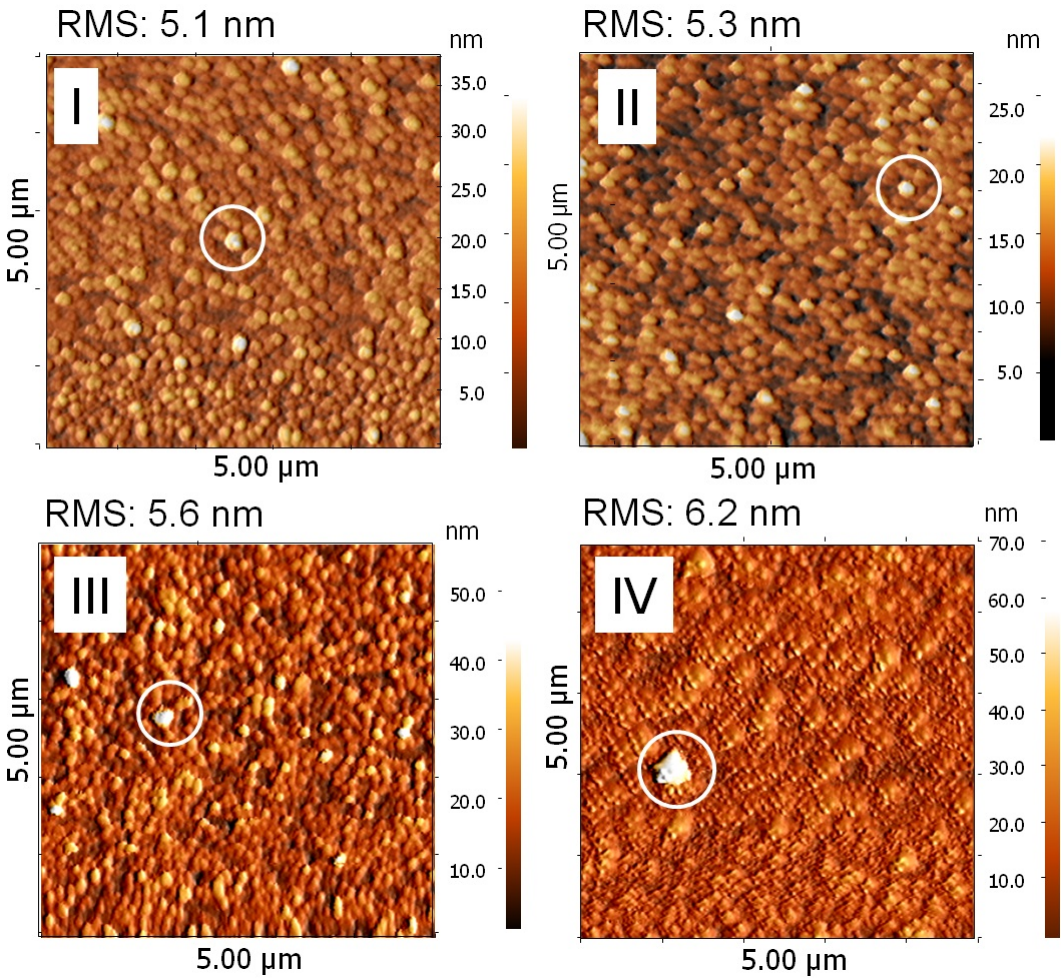

Figure 7.3: AFM surface morphology of Mg-doped $In_xGa_{1-x}N$ layers (In contents are listed in table 7.1).

7.3 Low-temperature photoluminescence characterization results of Mg-doped InGaN layers

The excitation energy, excitation intensity and measurement temperature in a PL measurement are very critical parameters since all of them have profound effects on the PL signal[232, 233]. For instance, excitation intensity influences the density of photo excited electrons and holes. When the carrier density in the investigated material is too low, if low excitation intensity is used, the measurement result is dominated by dis-

crete defects and impurities at the interfaces and within the bulk of the material[232]. Measurement temperature tunes the thermal occupation of the available states. For example, at the lowest temperature, PL is dominated by the lowest energy levels. It has been observed that as the sample temperature and corresponding thermal energy rises, excitons dissociate and carriers vacate shallow traps[232], resulting in a decrease in PL intensity. With different excitation energies, the penetration depth of the incident light can be changed. Namely, with lower and higher excitation energies the surface and bulk optical properties can be deduced, respectively. If multiple excitation wavelengths are available, this property of PL can be used to distinguish surface and bulk contributions [232, 233]. In order to get a comprehensive understanding of the optical properties of InGaN:Mg layers, PL measurements at various temperatures and excitation levels were carried out using emissions of a continuous-wave (CW) helium-cadmium laser (λ = 325 nm, I_{exc} = 0.004 - 1.2 W/cm^2), a pulsed nitrogen laser (λ = 337.1 nm, I_{exc} = 1.34 - 285 kW/cm^2) and the second harmonic of a Ti-sapphire laser (λ = 390 nm, I_{exc} = 300 kW/cm^2) as excitation sources. For investigation of PL at low temperature (LT), the samples were placed into a closed-cycle CCS-150 helium cryostat. PL emission was detected using an optical fiber and a spectrometer with a CCD camera. In Figure 7.4, LT PL spectra, measured at different excitation levels for all investigated samples before (a, c) and after (b, d) annealing, are shown. All LT PL spectra exhibit the presence of a relatively strong and narrow GaN-related near band edge peak indicating good quality of the GaN buffer layer. At low excitation level (1.2 W/cm^2), the PL band at 410 nm is visible in all as-grown samples (a). A clearly visible PL peak at λ = 460 nm was registered only in the as-grown sample which was doped with the lowest Mg doping level of 0.7x10^{20} cm^{-3} (a, I). The origins of the peaks at 410 and 460 nm will be discussed below. At high excitation level (285 kW/cm^2), a clearly distinguished PL band near 430 nm was observed in the spectra of the as grown samples I and II (c). A hypothesis for the origin of this peak will be given later in this chapter. After annealing, which was carried out to activate the Mg acceptors, a significant decrease in intensity of all bands was observed (b, d). It could be caused by the fact that the annealing process deteriorates the crystal quality of the InGaN layers, i.e. it adds a

number of nonradiative defects to the already existing ones after growth. The damage in crystal quality can be explained by the loss of the stability of InGaN by desorption of In atoms, leading to breaking of In-N bonds at high temperature. The possible defects in undoped samples were briefly explained in chapter 2 section 2.2. Moreover, all LT PL spectra show a decrease in integrated PL intensity of InGaN peaks with a rise of Mg doping concentration. This is caused by an increase of Mg incorporation and generation of Mg-related nonradiative recombination centers. In addition, the slight increase in RMS roughness from 5.1 nm to 6.2 nm might also lead to a decrease in PL intensity. The rough surface intensifies surface scattering resulting in a weaker absorption, and consequently lower intensity PL.

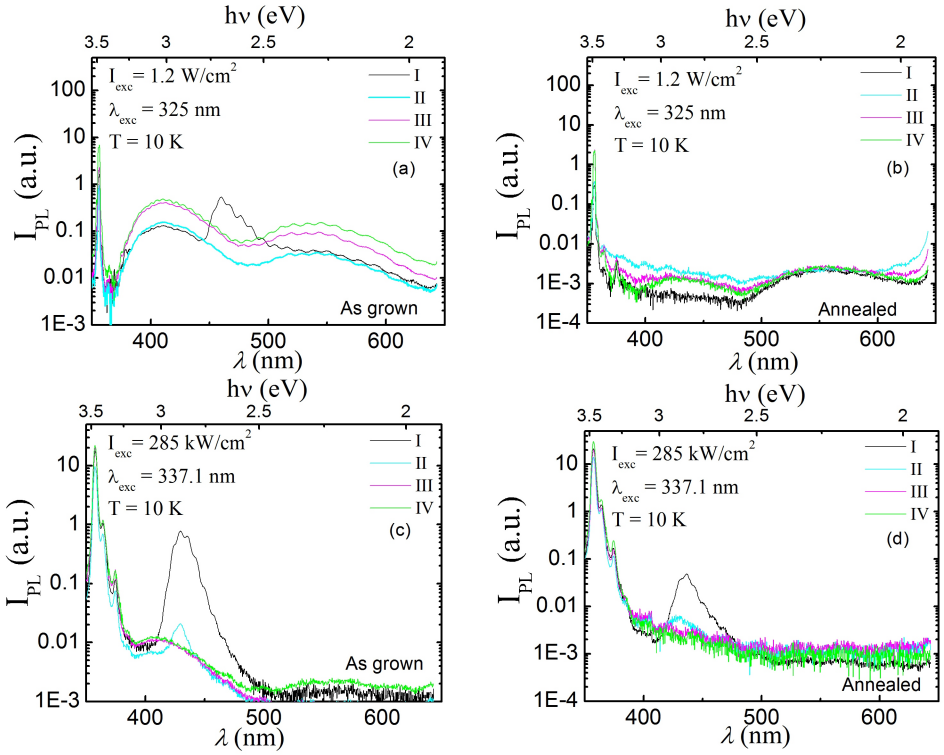

Figure 7.4: LT PL spectra of as grown (a, c) and annealed (b, d) InGaN:Mg epitaxial layers measured at I_{exc}=1.2 W/cm^2, I_{exc}=285 kW/cm^2. and I_{exc}=285 kW/cm^2, respectively.

To clarify the origin of the violet (410 nm) and blue (460 nm) PL bands, a series of PL experiments were performed for the sample grown at the lowest Mg doping level

(I). First, LT excitation-dependent PL spectra of the sample I at CW (Fig. 7.5a) and pulsed (Fig. 7.5b) excitations are presented. Figure 7.5c shows the dependence of the band positions on excitation level. All above-mentioned violet and blue bands are observed in the spectra as well. At low excitation intensities (0.0039 W/cm^2 to 0.07 W/cm^2) a very broad blue band was observed. The PL intensity rise with excitation intensity is stronger for the band at 460 nm, which becomes prevalent at higher excitation intensities, even for the case of the CW excitation (a). A super-linear increase of this band intensity with excitation intensity confirms a band-to-band recombination mechanism in InGaN:Mg. The change in the spectra with increasing excitation intensity can be attributed to the increased number of excited electron-hole pairs. Similar behavior was observed by Wang et al.[234] for Mg doped InN layers. The increase in PL intensity with rising excitation intensity was attributed to the high density of states in the valance band. As will be analyzed later, the changes in PL emission with decreasing excitation intensity are similar to those observed when increasing the measurement temperature. It can be seen for the blue band in Fig. 7.5(a, b, c) that a large short-wavelength shift from 467 to 434 nm occurs with rising excitation intensity from 3.9x10^{-6} to 174 kW/cm^2 (c). The observed spectral shift is in good agreement with other doped semiconductors[235, 233]. Lim et al. observed about 10 nm shift to higher energies in highly Mg-doped GaN layers[235]. The authors attributed this to the saturation of deep donors at high excitation intensity. Wang et al.[234] also observed a short blue shift in a series of Mg-doped InN layers. Valance-band Urbach tail was considered as the explanation[233]. Urbach tail is energy position at the band edges where the density of states tends to tail exponentially into the forbidden gap. This is due to defects near the band edges[236]. In this study, the strong short-wavelength shift of 33 nm cannot be explained in terms of the usual band-to-band transition. In order to describe the blue shift behavior, an electron-hole recombination mechanism in InGaN band tails caused by In clusterization is considered. For InGaN, there is a source of inhomogeneous broadening; namely, fluctuations in alloy composition. A fluctuation of In content contributes to tail formation often observed in InGaN/GaN QW structures[194]. Such phase segregation creates local potential fluctuations that are

highly susceptible to rapid state filling as the excitation level is increased. Therefore, the rapid band filling of localized InGaN radiative centers with high In composition can explain the strong blue shift. Although there is no sharp and clear phase separation observed for sample (I), a tiny relaxation visible by RSM is indicating a possibility of phase segregation. The PL band at 410 nm does not change its position significantly and saturates with increasing excitation level. As will be explained later in this section, this band originates from donor-acceptor pair (DAP) recombination in the GaN. The saturation of this peak can be attributed to the low density of states[234].

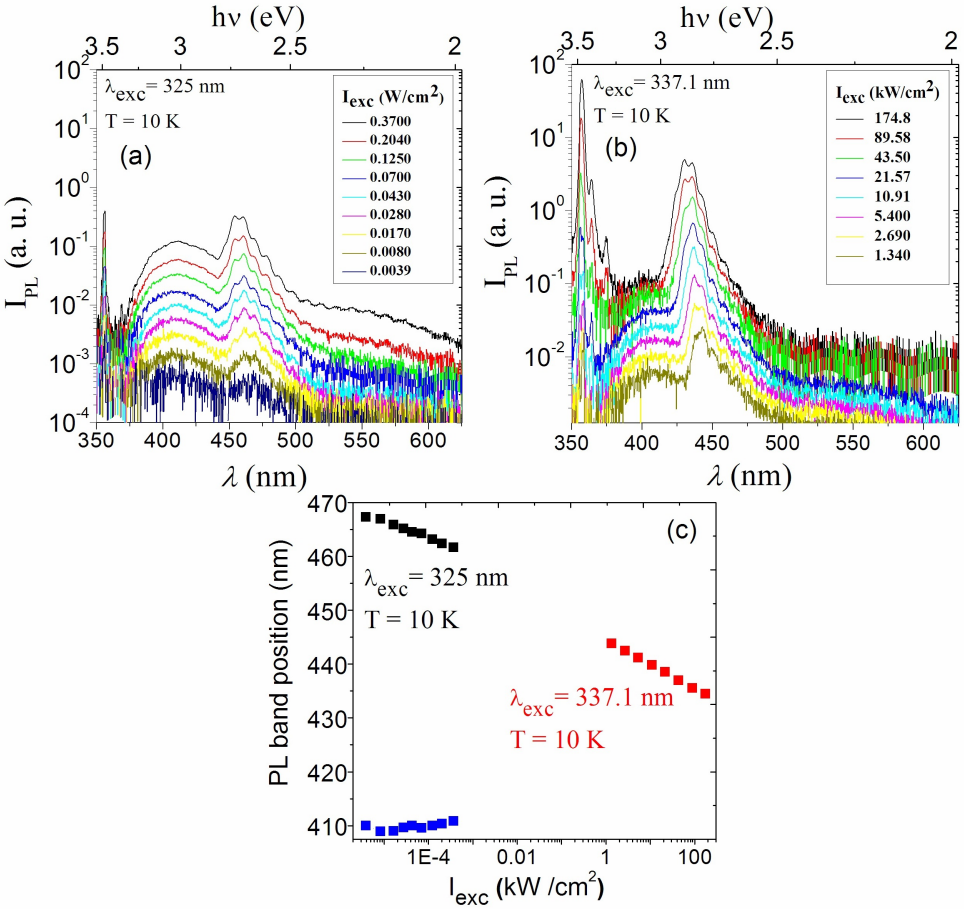

Figure 7.5: LT PL spectra of sample I at different excitation intensities of a) CW HeCd and b) pulsed N_2 laser emission. c) Position of the InGaN-related PL band as a function of excitation intensity.

In order to further clarify what is the origin of the band peak at 440 nm (position at

high excitation level in Fig. 7.5b-c) and to be able to answer whether it really originates from the InGaN:Mg, an experiment on the InGaN PL spectra was carried out using an excitation energy below the GaN band gap. The second harmonic emission of a Ti-sapphire laser with λ_{exc}=390 nm was used to eliminate absorption in the GaN layer. The result is shown in Fig. 7.6. The same blue band in the PL spectra near λ =440 nm was observed at an excitation energy below the GaN band gap. This is the evidence that the blue PL emission originates from InGaN:Mg. It should be noted that the "yellow" PL band at 560 nm from GaN disappeared from the PL spectra and a new red band near 620 nm becomes visible. Therefore, the red emission might be due to a recombination via deep levels in InGaN. In order to investigate the origin of the band at 410 nm, PL excitation (PLE) measurements were performed. Ordinary PL emission only reveals the lowest energy states. In order to measure expected emission at a fixed wavelength, PLE measurement was used. PLE spectra are determined by measuring emission intensity at a fixed wavelength while varying the wavelength of the incident light used to produce the electronically excited species responsible for emission. The excitation spectrum is a measure of the efficiency of electronic excitations as a function of excitation wavelength[232]. As an outcome of the PLE measurement result, the violet band at 410 nm can be ascribed to donor-acceptor pair (DAP) recombination in GaN since the PLE spectrum of this band has a GaN-related absorption edge (see the inset of Fig. 7.6. However, it is unclear whether the DAP PL band originates from segregated GaN regions in the InGaN:Mg layer or from an underlying unintentionally Mg-doped buffer GaN layer. The latter can be explained by segregation of Mg atoms into the uppermost 1-2 nm of the GaN buffer layer.

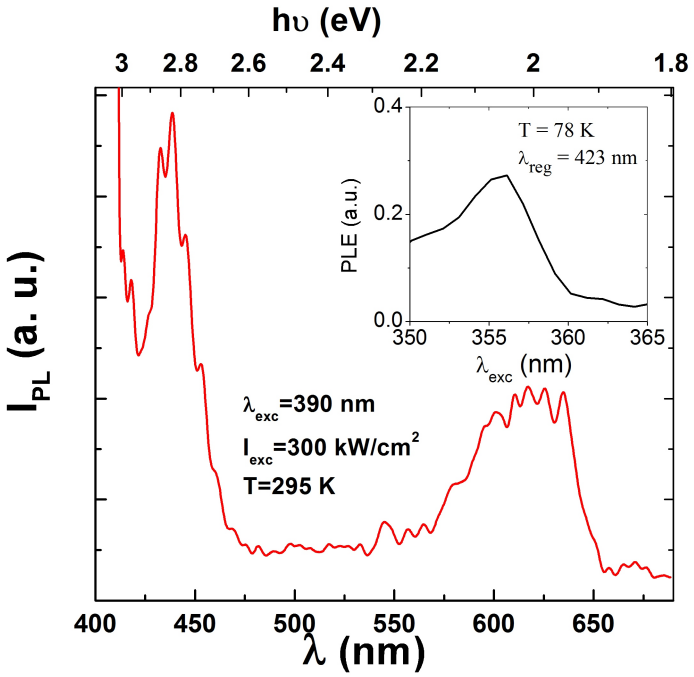

Figure 7.6: PL spectrum of (I) due to excitation of the second harmonic of a Ti-sapphire laser with λ_{exc}=390 nm. Inset shows PLE spectrum of blue PL band.

7.4 Temperature dependent photoluminescence and calculation of activation energies in Mg-doped InGaN layers

The effect of measurement temperature on the PL properties for the InGaN:Mg layer (I) was investigated by performing PL measurements at temperatures from 10 to 300K (Fig. 7.7a). At the lowest temperature of 10K, a sharp blue band at 440 nm and a very broad violet band at 410 nm were observed. The origin of a yellow band at 550 nm is not clearly known but carbon (C) impurities[237], N vacancies and O_N-related defect complexes[238], compensation centers[239] and N antisites[240] have been proposed as some possible reasons for yellow luminescence. A strong decrease in intensity of the blue band was observed with increasing temperature to 300K. The violet band is quenched

as the temperature increases to 120K. At a higher temperature than 120K, no PL emission from the violet band was observed. Before the discussion of the results it should be known that the thermal occupation of the available states in the valance and conduction bands can be tuned by varying the measurement temperature. At the lowest temperature, electron and hole pairs (excitons) are trapped at the lowest energy levels of the conduction and valance bands, respectively. That is why PL at LT is generally dominated by recombination from the lowest energy levels. As the sample temperature and the corresponding thermal energy increases, carriers might have enough energy to escape from trap centers, leading to a reduction in radiative recombination efficiency and therefore PL intensity[232, 233]. As mentioned before, the behavior of the PL spectrum with decreasing excitation intensity is similar to that with rising temperature. For instance; as the excitation intensity is increased the density of excited electron-hole pairs will increase and therefore the PL intensity will also increase. In other words, as the temperature decreases the number of localized holes will increase which enhances the radiative recombination efficiency and therefore the PL intensity. In light of this information, the increase in the intensity of the blue band at LT can be explained by high localization of carriers. The quenching of the violet band at LT is attributed to the filling of the density of the states. The intensity as a function of temperature also reveals a characteristic activation energy. Therefore, the Mg activation energy can be determined by doing a simulation of the temperature dependent PL measurement. The slope of the logarithmic variation of PL intensity as a function of the reciprocal temperature yields the activation energy of Mg. A two-channel dissociation Arrhenius model (Equ. (7.1)) was considered for simulation of the blue (440 nm) and violet (410 nm) bands[241].

$$\frac{I(T)}{I(0)} = \frac{1}{1 + C_1 x \exp(-\frac{E_{1A}}{kT}) + C_2 x \exp(-\frac{E_{2A}}{kT})} \tag{7.1}$$

Here I(T) and I(0) are the integrated intensities of the blue and violet emissions at a temperature of T and 0 K respectively. E_1 and E_2 are activation energies. C_1 and C_2 are constants[241]. Figure 7.7b demonstrates the variation of the integrated PL intensity as a function of the reciprocal temperature (dots) and fitting (solid line) [232, 241].

The simulation according to the Arrhenius model yielded activation energies of 160 meV and 80 meV, for the violet and blue bands (Fig. 7.7b), respectively. These values are close to the Mg acceptor activation energies in GaN and $In_{0.18}Ga_{0.82}N$, as given in[242, 243, 244].

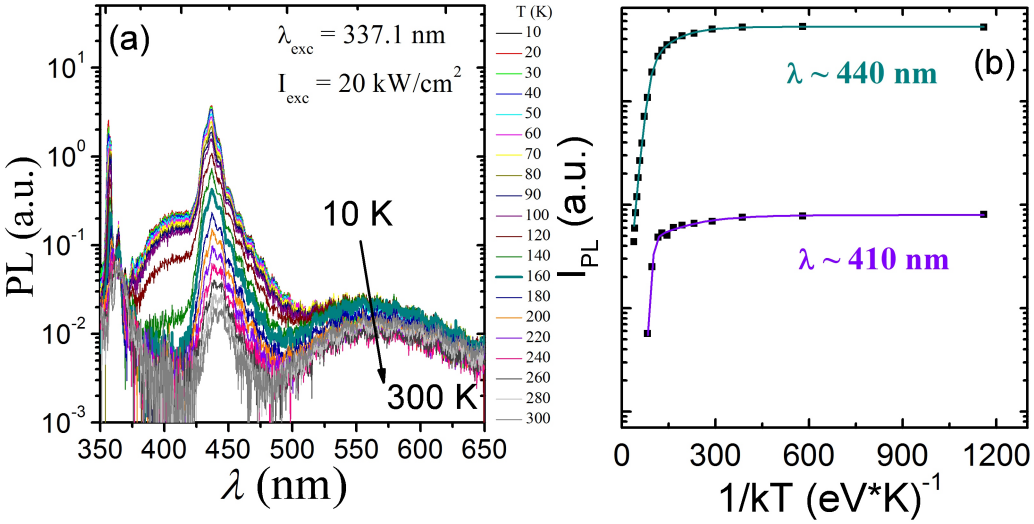

Figure 7.7: a) Temperature-resolved PL spectra for sample I. b) Temperature dependencies of PL intensity for the blue and violet bands and their Arrhenius fits.

7.5 Electrical characterization and evidence of p-type Mg-doped InGaN layers

Electrical properties were investigated by C-V measurements. For measurements, p-n diodes were fabricated as follows. Ni/Au ohmic contacts for the p-type material were deposited by electron beam evaporation. Subsequently, contact annealing at 495 ^oC under N_2 atmosphere was carried out. A recess was made using a chlorine-based reactive ion etch process to make contact to the n-type GaN. As an ohmic contact material, Ti/Al/Ni/Au was used without post-deposition annealing. The measurement frequency of the C-V measurements was 10 kHz. Ohmic contact for sample IV could not be made due to the very high sheet resistance. This is believed to be caused by

very high Mg doping level. Defects incorporated by the Mg doping itself play a key role for electrical compensation of the shallow Mg acceptor level[245]. The theory of the C-V measurement and M-S calculation, explained in chapter 3 section 3.3.2 of this thesis, will be considered during the subsequent discussion of the results. Figures 7.8a-b illustrate the C-V (a) and M-S (b) plots of the annealed InGaN:Mg layers grown at different Mg doping concentrations (Samples I, II and III). The sample doped with the lowest Mg acceptor concentration shows an inflection point with increasing bias voltage (Fig. 7.8a, I). The capacitance normalized to the area decreases with increasing bias voltage. However, at larger bias voltages, an increase in capacitance is observed. This behavior is considered in more detail in the M-S plot ($(C/A)^{-2}$ vs V) (Fig. 7.8b). The M-S plot of sample I shows a positive-slope region which is an indication of electron accumulation on the surface. An inflection point with a slope change is observed at high applied voltage. While the positive-slope region at low voltage is associated with the electron-rich surface layer, the negative-slope region at higher voltage is an indication of p-type conductivity[124]. The theory which describes this phenomena can be found in chapter 3 section 3.3.2 of this thesis. It was shown in section 6.3 of the previous chapter that the surface inversion layer for $In_xGa_{1-x}N$, with In content less than 20%, is shallow because the E_{Fs} energy at these In contents (X_{In}<0.2) is close to the conduction band edge of the $In_xGa_{1-x}N$. Therefore, the passivation of the carrier accumulation (inversion layer) is possible with increasing doping (acceptor) concentration. The effect of high doping on passivation of the inversion layer is observed by the C-V result of sample II. Namely, the inflection phenomenon is not realized after increasing the Mg doping concentration to 3.8x10^{20} cm^{-3}. For sample II, a slight increase in capacitance was found with increasing bias voltage (Fig. 7.8a, II). A negative slope, which is an indication of p-type conductivity, is seen in the M-S plot. For too high doping with Mg (sample III), a turn to n-type conductivity is illustrated by the positive slope in the M-S plot (Fig. 7.8b, III). While the calculated acceptor concentration using (3.3) is about 3.5x10^{18} cm^{-3} for the lowest doped layer (I), it reduces to 9.5x10^{17} cm^{-3} with increasing Mg doping (II). Further increase of Mg doping (III) leads to a change of conductivity from p-type to n-type. There are several reasons which could account

for the compensation of holes and the conductivity type variation due to high Mg doping concentrations. For instance, highly Mg-doped GaN has been shown to produce deep donors and consequently reduce the free hole concentration. This result has been attributed to the formation of compensating defect complexes like Mg-V_N [124, 125, 126]. Moreover, transmission electron microscopy investigations of high-level Mg doping of InN, InGaN and GaN have shown an increase in planar extended defects which could also contribute to the n-type conductivity[105, 103].

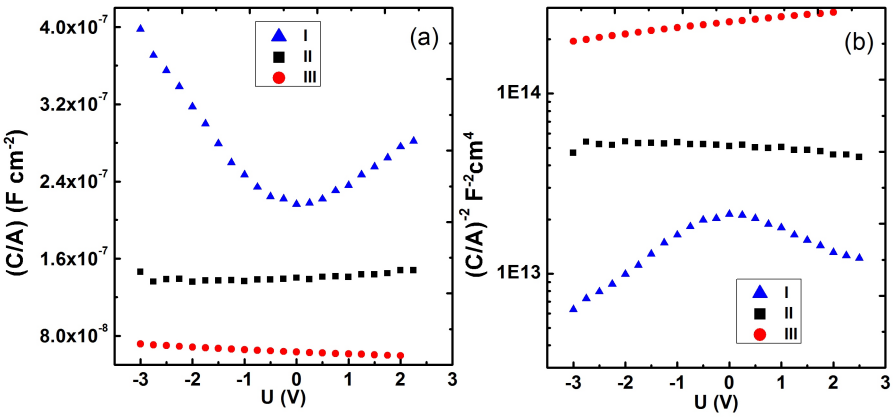

Figure 7.8: a) C-V and b) M-S plots of $In_xGa_{1-x}N$:Mg samples (In contents of the layers are listed in table 7.1).

7.6 Discussion of the structural and morphological characterization results of p-type In-rich Mg-doped InGaN

The low Mg activation energy in $In_{0.18}Ga_{0.82}N$, detailed in the previous section of this chapter, makes In-rich Mg-doped InGaN layers more interesting. A series of Mg-doped thick InGaN layers with thickness of about 120±5 nm was grown on n-type GaN templates. Process and layer structure were the same as for undoped layers (see upper image in Fig. 6.1a). The partial pressures of TMIn and Cp_2Mg were varied in order to keep a Cp_2Mg/III ratio of 1 for samples V, VI and VII, of 1.2 for sample VIII and of

Table 7.2: Details of the growth parameters and summary of the characterization results of In-rich $In_xGa_{1-x}N$:Mg layers. In content in InGaN, X_{In}, growth temperature, T_{growth}, flows of MO precursors(μmol/min), TMIn, TMGa, Cp_2Mg, ammonia flow, NH_3 (μmol/min), and root-mean square roughness, RMS, are included.

ID	Mg conc.	X_{In}	T_{growth}	TMIn	TMGa	NH_3	Mg/III	RMS
	$\mu mol/min$	±0.5%	^oC±1	$\mu mol/min$	$\mu mol/min$	$\mu mol/min$	%	nm
V	0.013	0.30	550	0.5	0.87	222.3	1	9
VI	0.020	0.51	550	1.2	0.87	222.3	1	18
VII	0.044	0.79	550	3.5	0.87	222.3	1	14
VIII	0.067	100	550	3.5	0	222.3	9	8
IX	0.044	100	550	3.5	0	222.3	7	8

1.9 for sample IX. Cp_2Mg was used as the dopant and N_2 was used as the carrier gas. In contents were determined by a comparison of XRD ω - 2θ measurement results with simulations. In order to activate Mg in the InGaN:Mg, the samples were annealed at 565 ^oC in N_2 ambient for one hour including heating up and cooling down times. The growth pressure was set to 200 mbar. More information about the growth parameters are listed in Table 7.2. SIMS measurements were performed on the $In_xGa_{1-x}N$:Mg (X_{In}: 0.30, 0.51, 0.79) layers, and Mg concentrations were found to be in the range of 3.3-6.0x10^{19} cm^{-3}. Even though the same Mg/III ratios have been used, a small variation in Mg concentration in the samples was observed. The tiny difference in Mg concentration might be caused by the inhomogeneous distribution of the Mg atoms, possibily due to the phase separated regions in the InGaN layers.

During the following part, at first, structural and morphological properties of Mg-doped In-rich InGaN layers will be analyzed and the results will be compared with the undoped In-rich InGaN layers studied in chapter 6. After that, the electrical characterization results investigated by means of the ECV technique will be examined. Figure 7.9 depicts XRD ω - 2θ scans of the Mg-doped InGaN layers. The trend of the XRD peak intensities and the broadening in the middle and in the high and low InGaN composition

ranges obtained for InN:Mg and InGaN:Mg layers is similar to the behavior observed for the un-doped In-rich InGaN layers (see Fig.6.2). Same explanations as given in chapter 6 section 6.1.1 can be considered for XRD results of InGaN:Mg layers as well. Inset Fig. 7.9 shows the comparison of the XRD ω - 2θ scans of the $In_{0.51}Ga_{0.49}N$ layer before and after annealing. It can be seen that there is no shift in the InGaN peak position which means that there is no change in In content after annealing. The comparison of this and previous XRD (XRD of $In_{0.18}Ga_{0.82}N$) results exhibit that high temperature annealing (765 ^{o}C) results in In desorption from the InGaN:Mg layer[231]. As a result, the activation energy of Mg acceptor in InN and InGaN is lower than the Mg activation energy in GaN. Therefore, low annealing temperature is enough to be able to activate Mg acceptor in InN and InGaN[246]. As will be shown during the electrical characterization section (section 7.7), the low annealing temperature of 565 ^{o}C which is close to the growth temperature of 550 ^{o}C is sufficient to activate the Mg atoms and reach p-type In-rich InGaN layers without any decrease in In content as shown in inset of Fig. 7.9.

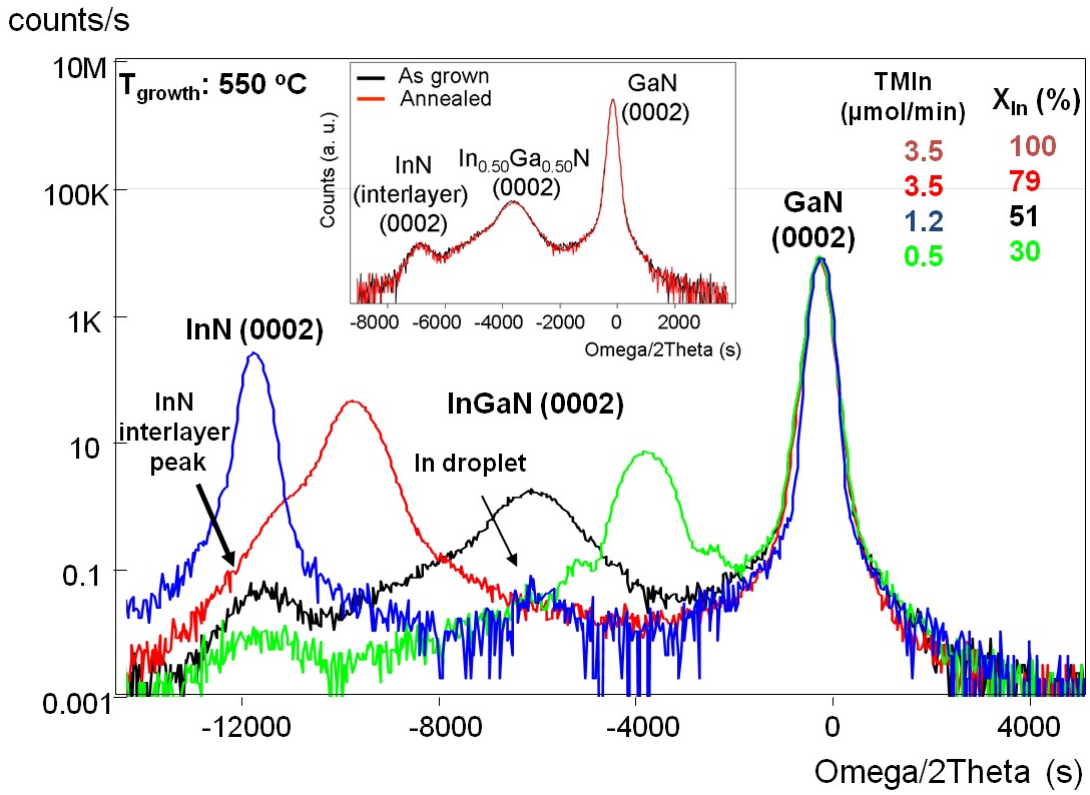

Figure 7.9: XRD ω - 2θ scans of InGaN:Mg layers of various In content before annealing. Inset shows the XRD ω - 2θ scan of $In_{0.79}Ga_{0.21}N$:Mg layer before and after annealing.

Figure 7.10 shows AFM surface measurement results of the InGaN:Mg and InN:Mg samples. There are some features observed on the surface. The feature density is getting higher and the size of the features is becoming larger in the middle of the InGaN composition range. Correspondingly, the surface is rougher. The same trend was observed by SEM results for undoped In-rich InGaN layers (see Fig. 6.4). The shape of the features on undoped InGaN was hexagonal. Partly hexagonal but mainly triangle-shaped features are seen on the surface of InGaN:Mg samples by AFM (sample VI in Fig. 7.10). This might be due to the different measurement techniques and/or the Mg-doping effect. The features observed are mainly triangle- shaped. Due to the similarities in surfaces between un-doped and Mg-doped layers, the interpretation of the SEM results in chapter 6 section 6.1 (namely, how the features are forming on the

surface, and how the surface morphology is changing depending on In content), can be considered for understanding the AFM results.

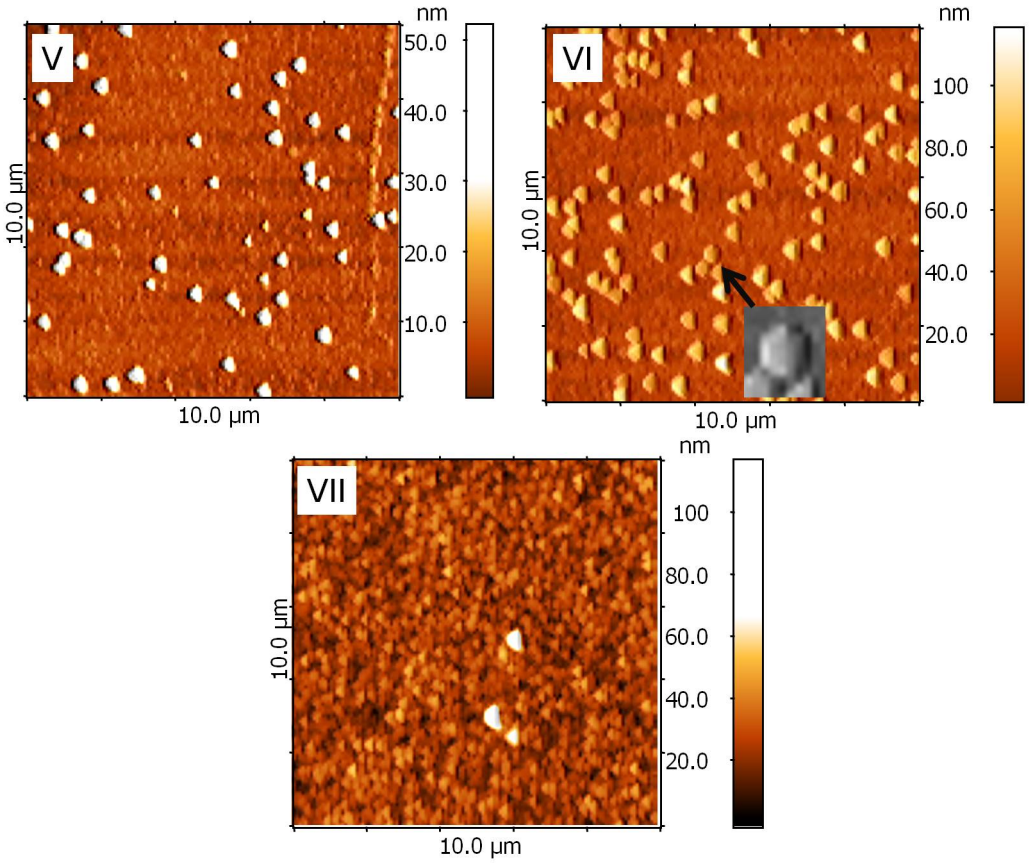

Figure 7.10: AFM images of InGaN:Mg layers. Inset in VI depicts a magnification of the shape of one feature realized on the surface.

7.7 Electrical characterization results and evidence of p-type conductivity in In-rich Mg-doped InGaN

Electrical characterization of In-rich InGaN:Mg layers was carried out by ECV measurements. An electrolyte (KOH) was used in order to be able to form Schottky contacts on the surface. As discussed in the previous section, due to the E_{sF} level which is above the conduction band minimum, a large surface electron accumulation is existing on the surface and therefore the metal contacts fail to form Schottky contacts on the surface. C-V

and Mott-Schottky plots of InN:Mg and In-rich $In_xGa_{1-x}N$:Mg (X_{In}: 0.30, 0.51, 0.79) samples are illustrated in Figures. 7.11a and b, respectively. The two InN:Mg samples have different Mg/III ratios of 1.2 (1) and 1.9 (2). The details of the growth parameters are listed in Table 7.2. It is evident in the Mott-Schottky plots that all layers except InN:Mg (1) have inflection points, where the sign of the slopes ($d(C/A)^{-2}/dV$) change from positive to negative. With increasing Ga content in the InGaN:Mg samples from 0 to 70%, the slope in the positive side gets steeper and the voltage required to change the slope sign from positive to negative (inflection point) moves to lower values (moves left). The bias value required to deplete the surface accumulation and to lead to a slope change in the M-S plot is depending on the amount of surface carriers[247]. It could be inferred that a reduction of the electron accumulation occurs with increasing Ga content in InGaN:Mg. As presented in chapter 6 section 6.3, an increase in Ga content causes a shift of the E_{sF} level through the conduction band minimum. Therefore, a weak downward band bending occurs, and correspondingly less electrons accumulate on the surface. This is enough to maintain charge neutrality. While the low-slope region at low voltages indicates the n-type conductivity, the slope region at higher voltage has the opposite sign, indicating a net concentration of acceptors in the bulk beneath the surface electron accumulation layer[247]. In order to investigate the effect of Mg doping on the change of the slope sign and accordingly the conductivity type of InN:Mg, two InN:Mg layers (1) and (2), with different Mg/III ratios have been examined. While there is no inflection point for sample 1 (sample VIII in Table 7.2), with increasing Mg doping level (Mg/III: 1.9%), a change in the slope was realized. Depending on the SIMS measurement results, the Mg concentrations are about $3.0x10^{19}$ cm^{-3} for sample 1 and $3.5x10^{20}$ cm^{-3} for sample 2. For the passivation of the high background electron concentration in InN, sufficient acceptor concentration is required[248, 249]. Unintentionally doped n-type InN samples, grown at similar growth conditions and analyzed during this work, show electron concentrations of about 3-$5x10^{19}$ cm^{-3} in conventional Hall measurements. It could be speculated that in order to reach p-type conductivity in InN, the Mg acceptor concentration must be in the range of 2-$5x10^{20}$ cm^{-3}. Anderson et al. presented similar behaviour for InN:Mg layers [249]. However, p-type conductivity

was achieved at the higher Mg concentration of 1.0x10^{21} cm^{-3}. This can be associated with the low quality of the layers, leading to a high background electron concentration. In order to investigate the influence of the Mg doping level on InGaN:Mg conductivity,

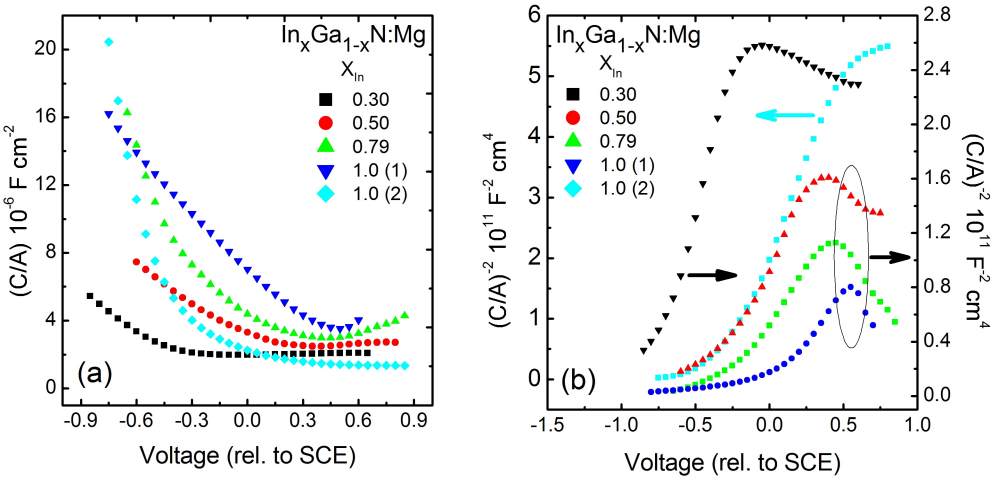

Figure 7.11: a) C-V and b) M-S plots of In-rich Mg-doped InGaN with constant Mg/III ratio, and of two InN samples with different Mg/III ratios.

a set of $In_{0.79}Ga_{0.21}N$ samples was grown by changing Mg/III ratio from 1% to 9%. SIMS measurements were performed on samples with Cp_2Mg/III ratios of 1%, 3%, 5%, and 7%. A linear increase of the Mg concentration with increasing Cp_2Mg/III ratio was observed as illustrated in the inset of Fig. 7.12a. Using this linear relation, the Mg concentration of the sample with Cp_2Mg/III ratio of 9% was estimated. The Mg concentrations are shown in the inset of Fig. 7.12b. At the lowest Mg concentration of 3.3x10^{19} cm^{-3}, a change in the slope sign from positive at low bias to negative at high bias is observed, indicating the existence of a buried p-type conductivity beneath the surface electron accumulation layer, as mentioned before. At the higher Mg concentration of 2.6x10^{20} cm^{-3}, a negative slope region, namely an indication of p-type conductivity, is also observed. However, with a further increase in Mg concentration to 4.4x10^{20} cm^{-3} and 6.0x10^{20} cm^{-3}, a negative slope region was not seen. This is evidence of a change to n-type conductivity at Mg concentrations higher than 2.6x10^{20} cm^{-3}. As discussed in section 7.5, excess Mg doping behaves as a donor by forming

Mg-N complexes with N vacancies. The detailed explanation for this effect can be found in section 7.4 of this chapter.

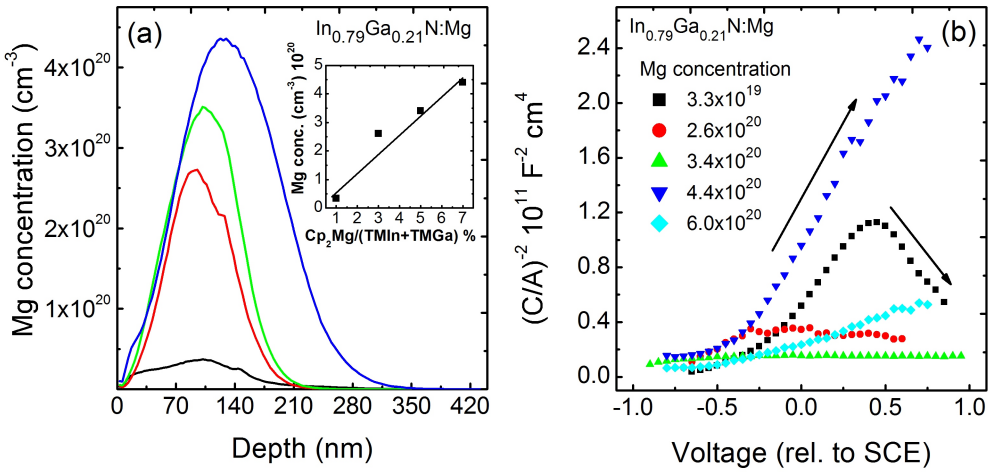

Figure 7.12: (a) Mg concentrations in InGaN:Mg layers measured by SIMS. Inset shows the variation of Mg concentration as a function of $Cp_2Mg/(TMIn+TMGa)$ ratio. (b) Mott-Schottky plots of the InGaN:Mg samples doped with different Mg acceptor concentrations.

7.8 Summary and discussion of Mg-doped InN and InGaN layers

A detailed study of the effect of the Mg doping on InN and InGaN properties and conductivity was presented in this chapter. It was shown that the Mg activation energy in $In_{0.18}Ga_{0.82}N$ is about 80 meV which is lower than the Mg activation energy (160 meV) in GaN:Mg. Due to this fact, an annealing temperature of 750 ^oC was found to be enough for the activation of Mg in InGaN:Mg. Therefore, it is believed that p-type InGaN is more convenient to be used as hole injection layer in the LED structures. By using the p-type InGaN, the degradation in the LED structures caused by required high annealing temperature of the GaN:Mg can be avoided. Moreover, it was observed that Mg doping concentration is a critical parameter for the conductivity type of the InGaN. A detailed investigation of the Mg doping concentration effect on the conductivity type

of InN and InGaN was carried out by growing InN and In-rich InGaN layers at different Mg doping concentrations. At a Mg doping range of 3.3x10^{19} cm^{-3} - 2.6x10^{20} cm^{-3}, p-type conductivity was obtained for InN and In-rich $In_xGa_{1-x}N$ ($X_{In} \geq$ 30%)layers beneath a surface electron accumulation layer. Less and more than this critical Mg doping range, the conductivity type is obtained to be n-type both for InN and InGaN layers. A doping less than the critical Mg doping range, acceptor concentration is not high enough to passivate the donor concentration, and therefore, the conductivity is found to be n-type. However, a doping more than the critical Mg doping range, the access Mg atoms form clusters with defects and N vacancies, which behave as donor, and therefore, the conductivity is measured to be n-type.

8 Summary and Conclusion

The most drastic breakthrough for InN, which was the measurement of the real bandgap of 0.65 eV instead of the previously accepted bandgap values of 1.9 - 2.1 eV[34, 35, 36, 37], makes it an attractive material among other III-V semiconductors. At the same time, the revision in bandgap has made the InGaN alloys more significant since one can cover the whole solar spectrum by only changing In composition in InGaN alloys. However, growing these materials in high quality is very challenging. Even though the growth of these materials by MBE yields better quality than MOCVD grown samples; MOCVD is the preferred growth technique from the view of mass production. Alloying of these materials with MOCVD grown of other nitrides, such as GaN and AlN, is essential to develop devices for instance InGaN based solar cells and AlInN based HEMT. With these motivations, the goal of this study was the growth of high-quality n- and p-type-doped InN and InGaN alloys with different In content and the detailed characterization. In chapter 5, the influence of the most critical MOCVD growth parameters, temperature and V/III ratio, on InN was investigated in detail. A proper growth region with respect to the structural, optical and electrical properties of InN as well as prevention of In droplet formation on the surface of InN was obtained. High (565 ^{o}C) and low (500 ^{o}C) growth temperatures and low V/III ratio result in In droplet formation on the surface due to lack of reactive N atoms. By increasing the V/III ratio and by keeping the growth temperature in the middle range (520 ^{o}C), In droplet formation was prevented. InN with a low screw dislocation density of 4.5x10^{8} cm^{-2} and a relatively high edge dislocation density of 1.0x10^{11} cm^{-2} were found. High lattice mismatch between InN and GaN is the main reason for high edge dislocation density. By Hall effect measurements, a carrier

density of 4.1x10^{18} cm^{-3} with a high electron mobility of 1200 cm^2/Vs was obtained from the InN layer grown at high temperature of 550 ^oC. A decrease in carrier concentration with rising growth temperature was observed. The decrease in the carrier concentration at high growth temperature was attributed to the decrease of the density of N vacancy. The decrease in the N vacancy concentration at high growth temperature has been proven by positron annihilation spectroscopy. In order to eliminate the influence of the surface electron accumulation layer on the electrical characterization results of the InN layers, optical techniques were proposed as alternative methods for characterization of the electrical properties. For that, Raman mode with respect to longitudinal phonon-plasmon (LPP) was analyzed. It was shown that a InN layer, which was grown at the highest V/III ratio, yield a low carrier concentration in the range of 9.0x10^{17} cm^{-3} compared to 6.0x10^{18} cm^{-3} as determined by Hall effect measurements. The low carrier concentration value indicates the high quality of the InN layer. The comparison of the results from Raman spectroscopy and Hall measurements suggest that the Hall measurement are dominated by the surface accumulation layer and therefore, it is an inappropriate technique for characterization of electrical properties of InN.

A large thermal stability difference between InN and GaN, very high equilibrium vapor pressure of nitrogen over InN and temperature stability of NH_3 hamper the growth of high quality In-rich InGaN layers, which are essential for multi junction solar cells as well as for red LEDs. In this study, a new approach was proposed, which is based on the enhancement of In incorporation by inserting a thin InN interlayer beneath the InGaN layer. As a result of this approach, an additional increase of In content in InGaN with an amount of 11% was achieved. For instance, while without the InN interlayer, the In content was about 74%, it increased to 85% when the InN interlayer was grown. The increase in In content is explained by In segregation from the InN interlayer to the InGaN layer. This explanation was reinforced by RBS measurement results. With the InN interlayer method, InGaN layers with various In contents ranging from 40% to 85% were successfully grown. This method can be complementary to growth temperature for increasing In content. Because with decreasing temperature, the In incorporation is enhanced but at the cost of less crystal quality of InGaN. Structural

and optical characterization results showed that the InGaN layers in the middle In composition range have the lowest quality. This is attributed to a high degree of atomic disorder and the large atomic radius difference between In and Ga atoms. Optical investigation confirmed the existence of a strong phase separation in the middle of the InGaN composition range. In other words, optical spectra of InGaN layers in the middle InGaN composition range exhibits more than one emission peak. This is believed to be originated from the formation of local minima in the band tail which is cause by In fluctuations as well as inhomogeneous lattice deformation and high density of impurity states. By XPS and IR reflectivity measurements, band bending and the related surface electron accumulation were observed in InGaN layers. In the light of these results, it could be concluded that the position of bulk Fermi level with respect to charge neutrality layer plays a very important role in surface electronic properties of semiconductors. For the investigated In-rich $In_xGa_{1-x}N$ layers, a transition from an accumulation layer to a depletion layer at the surface is observed at a composition slightly less than X_{In} =0.20.

p-Type InN and InGaN are essential in order to be used as hole injection layers for devices such as green laser diodes and long-wavelength emitters. In chapter 7, synthesis and a systematic study of structural, optical and electrical properties of Mg-doped $In_xGa_{1-x}N$ layers were presented. In the first part of chapter 7, it was demonstrated that p-type InGaN layers with about 18% In can be grown with an acceptor concentration of 3.5x10^{18} cm^{-3}. Even with low annealing temperature (750 ^oC), p-type conductivity was achieved. This means that Mg activation energy in these materials is lower that the activation energy of Mg in Mg-doped GaN. Temperature dependent PL revealed the activation energy of Mg in $In_{0.18}Ga_{0.82}N$:Mg is about 80 meV which is much lower that the activation energy of Mg in Mg-doped GaN which is about 160 meV. Even though the growth and annealing temperature of the $In_{0.18}Ga_{0.82}N$:Mg are lower than in the case of Mg-doped GaN, these temperatures are still high for the growth of solar cells and red LED structures since the active layers of these structures must be grown at low temperature to enhance In incorporation in InGaN. Therefore, p-type In-rich InGaN layers are necessary. With this motivation, in the second part, Mg-doped In-rich $In_xGa_{1-x}N$ (X_{In}: 0.30, 0.51, 0.79) layers were examined. The layers were grown

at a low temperature of 550 ^{o}C on GaN templates. The samples were annealed at a low temperature of 565 ^{o}C in order to activate Mg atoms. ECV results indicated that p-type buried layers exist in all Mg-doped In-rich InGaN layers. As expected, a surface accumulation layer was observed. A strong correlation with the amount of surface accumulation and In content in InGaN was obtained. It was also shown that Mg doping concentration is critical for the conductivity type change. For instance, in the case of InN:Mg, p-type conductivity was obtained when the InN layers were doped with Mg concentration in the range of 2.6x10^{20} cm^{-3}. Mg concentration higher than this value was observed to change the conductivity type of InN:Mg to completely n-type. In the case of over doping, Mg atoms form complexes with N vacancies which behave as donors and therefore results in a change in conductivity from p- to n-type.

In conclusion, in terms of electrical properties such as low carrier concentration of about 9x10^{17} cm^{-3} and high electron mobility of 1200 cm^{-3} and optical properties of low energy bandgap and narrow line widths of PL emission peaks (less than 100 meV) confirm the achievement of the good quality of MOCVD grown InN layers. A comparison of these results to the literature is reinforced the good quality of the layers achieved in this study[44, 250, 251]. The employed optical techniques for the determination of bulk carrier concentration and figuring out the reasons of the high bulk carrier concentration help to push forward the growth of good quality InN layers. For In-rich InGaN layers, the proposed method of growing InGaN layers directly on a thin InN interlayer is the key point for the achievement of the In-rich InGaN layers. In addition, as a first time, for MOCVD grown In-rich InGaN layers, it was shown that the transition from an electron accumulation to an electron depletion occurs when the In content is about 20%. Many physical aspects behind the magnesium doping mechanism for MOCVD grown InN and various Indium containing InGaN alloys were deeply investigated. It was obtained that Mg doping concentration as well as In composition plays important roles for doping mechanism. Depending on the In content in InGaN, the required Mg doping concentration to achieve p-type conductivity was found to be different. For example, a high hole carrier concentration of 3.5x10^{18} cm^{-3} was achieved for $In_{0.18}Ga_{0.82}N$ layers by controlling the Mg doping concentration. Above a critical Mg doping concentration,

Mg atoms form clusters with defects and therefore behave as donors in grown materials. Further investigations of electrical properties by employing variable filed Hall effect and temperature dependent Hall effect measurements are need to be done in order to understand and improve the material properties.

List of Figures

List of Tables

List of Abbreviations

AlN	aluminium nitride
AlGaN	aluminium galium nitride
ADM	amphoteric defect model
Al	aluminium
AFM	atomic force microcopy
CNL	charge neutrality layer
CBM	conduction band minimum
C-V	capacitance-voltage
Cp_2Mg	biscyclopentadienylmagnesium
CW	continuous wave
CCS	close couple schowerhead
CL	cathoholuminescence
DT	differential transmission
E_{sF}	surface fermi energy level
E_{FS}	fermi level stabilization energy
ECV	electrochemical capacitance voltage
FWHM	full width at half maximum
FTIR	fourier transform IR spectrometer
GaP	galium phosphide
GaAs	galium arsenide
Ga	galium
GaN	galium nitride
GaInAs	galium indium arsenide
GaInP	galium indium phosphide
H	hydrogen
HREEL	high resolution electron energy loss

HFET	high Electron Field Transistor
HT	high temperature
InN	indium nitride
In	indium
InGaN	indium galium nitride
LPP	longitudional phonon plasmon
LED	light lmitting diodes
LT	low temperature
Mg	magnesium
MOCVD	metal organic chamical vapor deposition
MBE	molecular beam epitaxy
m*	effective mass
N	nitrogen
NH_3	ammonia
n	bulk carrier concentration
O	oxygen
PLE	photoluminescence excitation spectrocopy
PL	photoluminescence
PAS	positron annihilation spectrocopy
RF	radio frequency
RSM	reciprocal space mapping
RMS	root mean square
RBS	rutherford backscatteting
SIMS	secondary ion mass spectroscopy
SiH_4	silane
SCE	saturated calomel electrode
SEM	scanning electron microscopy
TMGA	trimethylgallium
TEGa	triethylgallium
TMIn	trimethylindium
TEM	transmission electron microscopy
XPS	x-ray photoemission spectrocopy
XRD	x-ray diffraction
UV	ultraviolet
VBM	valance band maximum
V_{In}	indium vacancy
V_N	nitrogen vacancy

Bibliography

[1] S. Nakamura. The roles of structural imperfections in ingan-based blue light-emitting diodes and laser diodes. *Science*, 281:956–961, 1998.

[2] S. Nakamura. Ingan/algan blue-light-emitting diodes. *J. Vac. Sci. Technol.*, A 13(3):705–710, 1995.

[3] S. Nakamura, T. Mukai, and M. Senoh. High-power gan p-n junction blue-light-emitting diodes. *Japanese Journal of Applied Physics*, 30(Part 2, No. 12A):L1998–L2001, 1991.

[4] G. W. Crabtree and N. S. Lewis. Solar energy conversion. *Physics Today*, 3:37, 2007.

[5] D. Ginley, A. G. Martin, and R. Collins. Solar energy conversion toward 1 terawatt. *MRS Bulletin*, 33:355, 2008.

[6] V. Deodatta, S. Khatkhate, J. G. Randall, R. L. DiCarlo, and G. Dripps. Environment, health and safety issues for sources used in movpe growth of compound semiconductors. *Journal of Crystal Growth*, 272:816 – 821, 2004.

[7] T. Matsuoka, H. Okamoto, M. Nakao, H. Harima, and E. Kurimoto. Environment, health and safety issues for sources used in movpe growth of compound semiconductors. *Appl.Phys. Lett.*, 81:1246, 2002.

[8] M. Hori, K. Kano, T. Yamaguchi, Y. Saito, T. Araki, Y. Nanishi, N. Tera-guchi,

and A. Suzuki. Optical properties of ingan with entire alloy composition on inn buffer layer grown by rf-mbe. *Phys. Status Solidi B*, 234:750, 2002.

[9] T. Miyajima. Structure analysis of inn film using extended x-ray absorption fine structure method. *Phys. Status Solidi B*, 234:801, 2002.

[10] R. Juza, H. Hahn, and Z. Anorg. Über die kristallstrukturen von cu3n, gan und inn metallamide und metallnitride. *Allg. Chem.*, 239:282, 1938.

[11] S. N. Mohammad and H. Morkoc. Progress and prospects of group-iii nitride semiconductors. *Prog. Quantum Electron.*, 20:361, 1996.

[12] V. W. Chin, T. L. Transley, and T. Osotchan. Electron mobilities in gallium, indium, and aluminum nitrides. *J. Appl. Phys.*, 75:7365, 1994.

[13] K. F. Brennan J. D. Albrecht E. Bellotti, B. K. Doshi and P. P. Ruden. Ensemble monte carlo study of electron transport in wurtzite inn. *J. Appl. Phys.*, 85:916, 1999.

[14] S. K. O'leary, B. E. Foutz, M. S. Shur, U. V. Bhapkar, and L. F. Eastman. Electron transport in wurtzite indium nitride. *J. Appl. Phys.*, 83:826, 1998.

[15] S. K. O'Leary, B. E. Foutz, M. S. Shur, and L. F. Eastman. Potential performance of indium-nitride-based devices. *Appl. Phys. Lett.*, 88:152113, 2006.

[16] V. M. Polyatov and F. Schwierz. Low-field electron mobility in wurtzite inn. *Appl. Phys. Lett.*, 88:032101, 2006.

[17] T. L. Tansley and C. P. Foley. *Journal of Applied Physics*, 59:3241, 1986.

[18] C. S. Gallinat, G. Koblmĺuller, J. S. Brown, S. Bernardis, J. S. Speck, G. D. Chern, E. D. Readinger, H. Shen, , and M. Wraback. *Appl. Phys. Lett.*, 89:032109, 2006.

[19] N. Dietz, M. Alevli, R. Atalay, G. Durkaya, R. Collazo, J. Tweedie, S. Mita, and Z. Sitar. The influence of substrate polarity on the structural quality of inn layers grown by high-pressure chemical vapor deposition. *Applied Physics Letters*, 92(4):041911, 2008.

[20] O. Ambacher. Growth and applications of group iii-nitrides. *Journal of Physics D: Applied Physics*, 31(20):2653, 1998.

[21] S. C. Jain, M. Willander, J. Narayan, and R. Van Overstraeten. Iii-nitrides: Growth, characterization, and properties. *Journal of Applied Physics*, 87(3):965–1006, 2000.

[22] D. G. Zhao, S. J. Xu, M. H. Xie, S. Y. Tong, and H. Yang. Stress and its effect on optical properties of gan epilayers grown on si(111), 6h-sic(0001), and c-plane sapphire. *Applied Physics Letters*, 83(4):677 –679, jul 2003.

[23] Y. Honda, Y. Kuroiwa, M. Yamaguchi, and N. Sawaki. Growth of gan free from cracks on a (111)si substrate by selective metalorganic vapor-phase epitaxy. *Applied Physics Letters*, 80(2):222 –224, jan 2002.

[24] B. Maleyre, S. Ruffenach, O. Briot, and A. van der Lee. Lattice parameters of relaxed wurtzite indium nitride powder obtained by mocvd. *Superlattices and Microstructures*, 36:527 – 535, 2004.

[25] W. Paszkowicz, J. Adamczyk, S. Krukowski, M. Leszczynskiand S. Porowski, J. A. Sokolowski, M. Michalec, and W. Lasocha. Lattice parameters, density and thermal expansion of inn microcrystals grown by the reaction of nitrogen plasma with liquid indium. *Philosophical Magazine A*, 79(5):1145–1154, 1999.

[26] J. Wu. When group-iii nitrides go infrared: New properties and perspectives. *Journal of Applied Physics*, 106(1):011101, 2009.

[27] H. Iwanaga, A. Kunishige, and S. Takeuchi. Anisotropic thermal expansion in wurtzite-type crystals. *Journal of Materials Science*, 35:2451–2454, 2000. 10.1023/A:1004709500331.

[28] K. Wang and R. R. Reeber. Thermal expansion and elastic properties of inn. *Applied Physics Letters*, 79(11):1602–1604, 2001.

[29] K. Ito, K. Hiramatsu, H. Amano, and I. Akasaki. Preparation of alxga1-xn/gan heterostructure by movpe. *Journal of Crystal Growth*, 104(2):533 – 538, 1990.

[30] W.T. Read. *Dislocations in crystals.* International series in pure and applied physics. McGraw-Hill, 1953.

[31] V. Srikant, J. S. Speck, and D. R. Clarke. Mosaic structure in epitaxial thin films having large lattice mismatch. *Journal of Applied Physics*, 82(9):4286–4295, 1997.

[32] P. Anderson, J. Hirth, and J. Lothe. *Theory of Dislocations.* Cambridge University Press, 2008.

[33] Ingan: An overview of the growth kinetics, physical properties and emission mechanisms. *http://courses.eas.ualberta.ca/eas421/lecturepages/microstructures.html.*

[34] H. J. Hovel and J. J. Cuomo. Electrical and optical properties of rf-sputtered gan and inn. *Applied Physics Letters*, 20(2):71–73, 1972.

[35] J. Trainor and K. Rose. Some properties of inn films prepared by reactive evaporation. *Journal of Electronic Materials*, 3:821–828, 1974. 10.1007/BF02651400.

[36] K. Osamura, K. Nakajima, Y. Murakami, P. H. Shingu, and A. Ohtsuki. Fundamental absorption edge in gan, inn and their alloys. *Solid State Communications*, 11(5):617 – 621, 1972.

[37] K. Osamura, S. Naka, and Y. Murakami. Preparation and optical properties of gainn thin films. *Journal of Applied Physics*, 46(8):3432–3437, 1975.

[38] T. L. Tansley and C. P. Foley. Electron mobility in indium nitride. *Electronics Letters*, 20(25-26):1066–1068, 1984.

[39] C. P. Foley and T. L. Tansley. Morphology and structure of indium nitride films. *Applications of Surface Science*, 22 - 23, Part 2(0):663 – 669, 1985.

[40] C. P. Foley and T. L. Tansley. Pseudopotential band structure of indium nitride. *Phys. Rev. B*, 33:1430–1433, Jan 1986.

[41] T. L. Tansley and C. P. Foley. Infrared absorption in indium nitride. *Journal of Applied Physics*, 60(6):2092–2095, 1986.

[42] K. S. A. Butcher, M. W. Fouquet, P. P. T. Chen, T. L. Tansley, and S. Srikeaw. High mobility nitrides. *Materials Research Society Symposium Proceedings*, 693(0):I6.9.1, 1985.

[43] W. Walukiewicz, J. W. Ager III, K. M. Yu, Z. Liliental-Weber, J. Wu, S. X. Li, R. E. Jones, and J. D. Denlinger. Structure and electronic properties of inn and in-rich group iii-nitride alloys. *Journal of Physics D: Applied Physics*, 39(5):R83, 2006.

[44] Hai Lu, William J. Schaff, Jeonghyun Hwang, Hong Wu, Goutam Koley, and Lester F. Eastman. Effect of an aln buffer layer on the epitaxial growth of inn by molecular-beam epitaxy. *Applied Physics Letters*, 79(10):1489–1491, 2001.

[45] Y. Nanishi, Y. Saito, and T. Yamaguchi. Rf-molecular beam epitaxy growth and properties of inn and related alloys. *Japanese Journal of Applied Physics*, 42(Part 1, No. 5A):2549–2559, 2003.

[46] V. Y. Davydov, A. A. Klochikhin, R. P. Seisyan, V. V. Emtsevand S. V. Ivanov, F. Bechstedt, J. Furthmüller, H. Harimaand A.V. Mudryi, J. Aderhold, O. Semchinova, and J. Graul. Absorption and emission of hexagonal inn. evidence of narrow fundamental band gap. *physica status solidi (b)*, 229(3):r1–r3, 2002.

[47] J. Wu, W. Walukiewicz, K. M. Yu, J. W. Ager, E. E. Haller, H. Lu, William J. Schaff, Y. Saito, and Y. Nanishi. Unusual properties of the fundamental band gap of inn. *Applied Physics Letters*, 80(21):3967–3969, 2002.

[48] K. Sugita, H. Takatsuka, A. Hashimoto, and A. Yamamoto. Photoluminescence and optical absorption edge for movpe-grown inn. *physica status solidi (b)*, 240(2):421–424, 2003.

[49] T. Inushima, V. V. Mamutin, V. A. Vekshin, S. V. Ivanov, T. Sakon, M. Motokawa, and S. Ohoya. Physical properties of inn with the band gap energy of inn. *Journal of Crystal Growth*, 227 - 228(0):481 – 485, 2001.

[50] A. G. Bhuiyan, A. Hashimoto, and A. Yamamoto. Indium nitride (inn): A review on growth, characterization, and properties. *Journal of Applied Physics*, 94(5):2779–2808, 2003.

[51] V. Y. Davydov, A.A. Klochikhin, V.V. Emtsev, D.A. Kurdyukovand S.V. Ivanov, V.A. Vekshin, F. Bechstedt, J. Furthmüllerand J. Aderhold, J. Graul, A.V. Mudryi, H. Harima, A. Hashimoto, A. Yamamoto, and E.E. Haller. Band gap of hexagonal inn and ingan alloys. *physica status solidi (b)*, 234(3):787–795, 2002.

[52] C. S. Gallinat, G. Koblmüller, J. S. Brown, S. Bernardis, J. S. Speck, G. D. Chern, E. D. Readinger, H. Shen, and M. Wraback. In-polar inn grown by plasma-assisted molecular beam epitaxy. *Applied Physics Letters*, 89(3):032109, 2006.

[53] P. Schley, R. Goldhahn, G. Gobsch, M. Feneberg, K. Thonkeand X. Wang, and A. Yoshikawa. Influence of strain on the band gap energy of wurtzite inn. *physica status solidi (b)*, 246(6):1177–1180, 2009.

[54] E. Burstein. Anomalous optical absorption limit in insb. *Phys. Rev.*, 93:632–633, Feb 1954.

[55] T. S. Moss. The interpretation of the properties of indium antimonide. *Proceedings of the Physical Society. Section B*, 67(10):775, 1954.

[56] G. Motlan, E. M. Goldys, and T. L. Tansley. Optical and electrical properties of inn grown by radio-frequency reactive sputtering. *Journal of Crystal Growth*, 241(12):165 – 170, 2002.

[57] N. A. Gorjunova. The interpretation of the properties of indium antimonide. *Slosnye Almazopodobnye Poluprovodniki,Moscow*, 1964.

[58] J. B. MacChesney, P. M. Bridenbaugh, and P. B. O'Connor. Thermal stability of indium nitride at elevated temperatures and nitrogen pressures. *Materials Research Bulletin*, 5(9):783 – 791, 1970.

[59] P. D. C. King, T. D. Veal, P. H. Jefferson, S. A. Hatfield, L. F. J. Piper, C. F. McConville, F. Fuchs, J. Furthmüller, F. Bechstedt, H. Lu, and W. J. Schaff.

Determination of the branch-point energy of inn: Chemical trends in common-cation and common-anion semiconductors. *Phys. Rev. B*, 77:045316, Jan 2008.

[60] S. H. Wei and A. Zunger. Valence band splittings and band offsets of aln, gan, and inn. *Applied Physics Letters*, 69(18):2719–2721, 1996.

[61] S.H. Wei and A. Zunger. Predicted band-gap pressure coefficients of all diamond and zinc-blende semiconductors: Chemical trends. *Phys. Rev. B*, 60:5404–5411, Aug 1999.

[62] T. D. Veal, C. F. McConville, and W. J. Schaff. *Indium Nitride and Related Alloys*. Taylor & Francis, 2009.

[63] S.H. Wei and A. Zunger. Calculated natural band offsets of all ii–vi and iii–v semiconductors: Chemical trends and the role of cation d orbitals. *Applied Physics Letters*, 72(16):2011–2013, 1998.

[64] G. Martin, A. Botchkarev, A. Rockett, and H. Morkoç. Valence-band discontinuities of wurtzite gan, aln, and inn heterojunctions measured by x-ray photoemission spectroscopy. *Applied Physics Letters*, 68(18):2541–2543, 1996.

[65] C. L. Wu, H. M. Lee, C. T. Kuo, S. Gwo, and C. H. Hsu. Polarization-induced valence-band alignments at cation- and anion-polar inn/gan heterojunctions. *Applied Physics Letters*, 91(4):042112, 2007.

[66] P. D. C. King, T. D. Veal, C. E. Kendrick, L. R. Bailey, S. M. Durbin, and C. F. McConville. Inn/gan valence band offset: High-resolution x-ray photoemission spectroscopy measurements. *Phys. Rev. B*, 78:033308, Jul 2008.

[67] S. X. Li, K. M. Yu, J. Wu, R. E. Jones, W. Walukiewicz, J. W. Ager, W. Shan, E. E. Haller, H. Lu, and W. J. Schaff. Fermi-level stabilization energy in group iii nitrides. *Phys. Rev. B*, 71:161201, Apr 2005.

[68] V. Bougrov, M. E. Levinshtein, S. L. Rumyantsev, and A. Zubrilov. Properties of advanced semiconductor materials gan, aln, inn, bn, sic, sige. *John Wiley & Sons, Inc.*, (1):1–30, 2001.

[69] G. Yu. Properties of advanced semiconductor materials gan, aln, inn, bn, sic, sige. *John Wiley & Sons, Inc.*, (1):31–47, 2001.

[70] W. Walukiewicz. Amphoteric native defects in semiconductors. *Applied Physics Letters*, 54(21):2094–2096, 1989.

[71] W. Walukiewicz. Intrinsic limitations to the doping of wide-gap semiconductors. *Physica B: Condensed Matter*, 302-303(0):123 – 134, 2001.

[72] W. Monch. *Semiconductor Surfaces and Interfaces*. Springer Series in Surface Sciences. Springer, 2001.

[73] S. B. Zhang, S.H. Wei, and A. Zunger. A phenomenological model for systematization and prediction of doping limits in ii–vi and i–iii–vi[sub 2] compounds. *Journal of Applied Physics*, 83(6):3192–3196, 1998.

[74] C. G. Van de Walle and J. Neugebauer. The roles of structural imperfections in ingan-based blue light-emitting diodes and laser diodes. *Nature*, 423:626, 2003.

[75] J. Robertson and B. Falabretti. Band offsets of high k gate oxides on iii-v semiconductors. *Journal of Applied Physics*, 100(1):014111, 2006.

[76] I. Mahboob, T. D. Veal, L. F. J. Piper, C. F. McConville, H. Lu, W. J. Schaff, J. Furthmüller, and F. Bechstedt. Origin of electron accumulation at wurtzite inn surfaces. *Phys. Rev. B*, 69:201307, May 2004.

[77] F. Daniel, S. Heidemarie, and G. Marius. Band dispersion relations of zinc-blende and wurtzite inn. *Phys. Rev. B*, 69:165204, Apr 2004.

[78] J. Tersoff. Schottky barriers and semiconductor band structures. *Phys. Rev. B*, 32:6968–6971, Nov 1985.

[79] H. Lu, W. J. Schaff, L. F. Eastman, and C. E. Stutz. Surface charge accumulation of inn films grown by molecular-beam epitaxy. *Applied Physics Letters*, 82(11):1736–1738, 2003.

[80] K. A. Rickert, A. B. Ellis, F. J. Himpsel, H. Lu, W. Schaff, J. M. Redwing, F. Dwikusuma, and T. F. Kuech. X-ray photoemission spectroscopic investigation of surface treatments, metal deposition, and electron accumulation on inn. *Applied Physics Letters*, 82(19):3254–3256, 2003.

[81] I. Mahboob, T. D. Veal, C. F. McConville, H. Lu, and W. J. Schaff. Intrinsic electron accumulation at clean inn surfaces. *Phys. Rev. Lett.*, 92:036804, Jan 2004.

[82] H. Lüth. *Solid Surfaces, Interfaces and Thin Films*. Graduate Texts in Physics. Springer, 2010.

[83] *Philip David King, Charge Neutrality Level in Significantly Cation-Anion Mismatched Semiconductors*. PhD thesis, University of Warwick, 2009.

[84] C. Stampfl, C. G. Van de Walle, D. Vogel, P. Krüger, and J. Pollmann. Native defects and impurities in inn: First-principles studies using the local-density approximation and self-interaction and relaxation-corrected pseudopotentials. *Phys. Rev. B*, 61:R7846–R7849, Mar 2000.

[85] M. Yoshimoto, H. Yamamoto, W. Huang, H. Harima, J. Saraie, A. Chayahara, and Y. Horino. Widening of optical bandgap of polycrystalline inn with a few percent incorporation of oxygen. *Applied Physics Letters*, 83(17):3480–3482, 2003.

[86] A. Janotti and C. G. Van de Walle. Sources of unintentional conductivity in inn. *Applied Physics Letters*, 92(3):032104, 2008.

[87] S. Limpijumnong and C. G. Van de Walle. Passivation and doping due to hydrogen in iii-nitrides. *physica status solidi (b)*, 228(1):303–307, 2001.

[88] D. C. Look, H. Lu, W. J. Schaff, J. Jasinski, and Z. Liliental-Weber. Donor and acceptor concentrations in degenerate inn. *Applied Physics Letters*, 80(2):258–260, 2002.

[89] E. A. Davis, S. F. J. Cox, R. L. Lichti, and C. G. Van de Walle. Shallow donor state of hydrogen in indium nitride. *Applied Physics Letters*, 82(4):592–594, 2003.

[90] G. Pettinari, F. Masia, M. Capizzi, A. Polimeni, M. Losurdo, G. Bruno, T. H. Kim, S. Choi, A. Brown, V. Lebedev, V. Cimalla, and O. Ambacher. Experimental evidence of different hydrogen donors in n-type inn. *Phys. Rev. B*, 77:125207, Mar 2008.

[91] S. P. Fu, T. J. Lin, W. S. Su, C. Y. Shieh, Y. F. Chen, C. A. Chang, N. C. Chen, and P. H. Chang. Influence of hydrogenation on surface morphologies, transport, and optical properties of inn epifilms. *Journal of Applied Physics*, 99(12):126102, 2006.

[92] J. Wu, W. Walukiewicz, S. X. Li, R. Armitage, J. C. Ho, E. R. Weber, E. E. Haller, Hai Lu, William J. Schaff, A. Barcz, and R. Jakiela. Effects of electron concentration on the optical absorption edge of inn. *Applied Physics Letters*, 84(15):2805–2807, 2004.

[93] L. F. J. Piper, T. D. Veal, C. F. McConville, H. Lu, and W. J. Schaff. Origin of the n-type conductivity of inn: The role of positively charged dislocations. *Applied Physics Letters*, 88(25):252109, 2006.

[94] H. Wang, D. S. Jiang, L. L. Wang, X. Sun, W. B. Liu, D. G. Zhao, J. J. Zhu, Z. S. Liu, Y. T. Wang, S. M. Zhang, and H. Yang. Investigation on the structural origin of n-type conductivity in inn films. *Journal of Physics D: Applied Physics*, 41(13):135403, 2008.

[95] A. Yamamoto, T. Tanaka, K. Koide, and A. Hashimoto. Improved electrical properties for metalorganic vapour phase epitaxial inn films. *physica status solidi (a)*, 194(2):510–514, 2002.

[96] D. W. Jenkins and J. D. Dow. Electronic structures and doping of inn. *Phys. Rev. B*, 39:3317–3329, Feb 1989.

[97] X. M. Duan and C. Stampfl. Nitrogen vacancies in inn: Vacancy clustering and metallic bonding from first principles. *Phys. Rev. B*, 77:115207, Mar 2008.

[98] C. G. Van de Walle, J. L. Lyons, and A. Janotti. Controlling the conductivity of inn. *physica status solidi (a)*, 207(5):1024–1036, 2010.

[99] T. L. Tansley and R. J. Egan. Point-defect energies in the nitrides of aluminum, gallium, and indium. *Phys. Rev. B*, 45:10942–10950, May 1992.

[100] A. Yamamoto, Y. Murakami, K. Koide, M. Adachi, and A. Hashimoto. Growth temperature dependences of movpe inn on sapphire substrates. *physica status solidi (b)*, 228(1):5–8, 2001.

[101] F. Tuomisto, J. M. Maki, C. Rauch, and I. Makkonen. On the formation of vacancy defects in iii-nitride semiconductors. *Journal of Crystal Growth*, 350(1):93 – 97, 2012.

[102] Y. Takei and T. Nakayama. Electron-carrier generation by edge dislocations in inn films: First-principles study. *Journal of Crystal Growth*, 311(10):2767 – 2771, 2009.

[103] X. Wang, S. B. Che, Y. Ishitani, and A. Yoshikawa. Threading dislocations in in-polar inn films and their effects on surface morphology and electrical properties. *Applied Physics Letters*, 90(15):151901, 2007.

[104] V. Cimalla, V. Lebedev, F. M. Morales, R. Goldhahn, and O. Ambacher. Model for the thickness dependence of electron concentration in inn films. *Applied Physics Letters*, 89(17):172109, 2006.

[105] V. Lebedev, V. Cimalla, T. Baumann, O. Ambacher, F. M. Morales, J. G. Lozano, and D. González. Effect of dislocations on electrical and electron transport properties of inn thin films. ii. density and mobility of the carriers. *Journal of Applied Physics*, 100(9):094903, 2006.

[106] P. D. C. King, T. D. Veal, and C. F. McConville. Unintentional conductivity of indium nitride: transport modelling and microscopic origins. *Journal of Physics: Condensed Matter*, 21(17):174201, 2009.

[107] Ö. Tuna, R. Kirste, S. Mohn, E. Bakir Kandemir, C. Giesen, H. Kalisch, A. Vescan, A. Hoffmann, and M. Heuken. Thermodynamic study on metalorganic vapor-phase epitaxial growth of group iii nitrides. *Japanese Journal of Applied Physics*, (Part 2, No. 9A/B), submitted.

[108] O. Ambacher, M. S. Brandt, R. Dimitrov, T. Metzger, M. Stutzmann, R. A. Fischer, A. Miehr, A. Bergmaier, and G. Dollinger. Thermal stability and desorption of group iii nitrides prepared by metal organic chemical vapor deposition. *Journal of Vacuum Science & Technology B: Microelectronics and Nanometer Structures*, 14(6):3532–3542, 1996.

[109] W. K. Chen, Y. C. Pan, H. C. Lin, J. Ou, W. H. Chen, and M. C. Lee. Growth and x-ray characterization of an inn film on sapphire prepared by metalorganic vapor phase epitaxy. *Japanese Journal of Applied Physics*, 36(Part 2, No. 12B):L1625–L1627, 1997.

[110] A. O. Rachel, J. K. Menno, J. H. Colin, G. Andrew, and D. Briggs. The influence of ammonia on the growth mode in ingan/gan heteroepitaxy. *Journal of Crystal Growth*, 272(1-4):393 – 399, 2004.

[111] A. Koukitu, T. Taki, N. Takahashi, and H. Seki. Thermodynamic study on the role of hydrogen during the movpe growth of group iii nitrides. *Journal of Crystal Growth*, 197(1-2):99 – 105, 1999.

[112] V. Darakchieva, K. Lorenz, M. Y. Xie, E. Alves, W. J. Schaff, T. Yamaguchi, Y. Nanishi, S. Ruffenach, M. Moret, and O. Briot. Unintentional incorporation of h and related structural and free-electron properties of c- and a-plane inn. *physica status solidi (a)*, 209(1):91–94, 2012.

[113] A. Koukitu, N. Takahashi, and H. Seki. Thermodynamic study on metalorganic vapor-phase epitaxial growth of group iii nitrides. *Japanese Journal of Applied Physics*, 36(Part 2, No. 9A/B):L1136–L1138, 1997.

[114] O. Briot, S. Ruffenach, M. Moret, B. Gil, C. Giesen, M. Heuken, S. Rushworth,

T. Leese, and M. Succi. Growth of inn films and nanostructures by movpe. *Journal of Crystal Growth*, 311(10):2761 – 2766, 2009.

[115] M. K. I. Senevirathna, S. Gamage, R. Atalay, A. R. Acharya, A. G. U. Perera, N. Dietz, M. Buegler, A. Hoffmann, L. Su, A. Melton, and I. Ferguson. Effect of reactor pressure on the electrical and structural properties of inn epilayers grown by high-pressure chemical vapor deposition. *Journal of Vacuum Science & Technology A: Vacuum, Surfaces, and Films*, 30(3):031511, 2012.

[116] I. H. Ho and G. B. Stringfellow. Solid phase immiscibility in gainn. *Applied Physics Letters*, 69(18):2701–2703, 1996.

[117] Z. Liliental-Weber, D. N. Zakharov, K. M. Yu, J. W. Ager, W. Walukiewicz, E. E. Haller, H. Lu, and W. J. Schaff. Compositional modulation in ingan: Tem and x-ray studies. *Journal of Electron Microscopy*, 54(3):243–250, June 2005.

[118] Ingan: An overview of the growth kinetics, physical properties and emission mechanisms. *Ö. Tuna, unpublished results.*

[119] A. Tabata, L. K. Teles, L. M. R. Scolfaro, J. R. Leite, A. Kharchenko, T. Frey, D. J. As, D. Schikora, K. Lischka, J. Furthmüller, and F. Bechstedt. Phase separation suppression in ingan epitaxial layers due to biaxial strain. *Applied Physics Letters*, 80(5):769–771, 2002.

[120] R. Singh, D. Doppalapudi, T. D. Moustakas, and L. T. Romano. Phase separation in ingan thick films and formation of ingan/gan double heterostructures in the entire alloy composition. *Applied Physics Letters*, 70(9):1089–1091, 1997.

[121] *Wojciech M. Linhart, Electron accumulation and doping in InN and InGaN alloys.* PhD thesis, University of Warwick, 2012.

[122] S. Fischer, C. Wetzel, E. E. Haller, and B. K. Meyer. On p-type doping in gan acceptor binding energies. *Applied Physics Letters*, 67(9):1298–1300, 1995.

[123] J. W. Orton. Acceptor binding energy in gan and related alloys. *Semiconductor Science and Technology*, 10(1):101, 1995.

[124] N. Miller, J. W. Ager, III, H. M. Smith, III, M. A. Mayer, K. M. Yu, E. E. Haller, W. Walukiewicz, W. J. Schaff, C. Gallinat, G. Koblmuller, and J. S. Speck. Hole transport and photoluminescence in mg-doped inn. *Journal of Applied Physics*, 107(11):113712, 2010.

[125] U. Kaufmann, P. Schlotter, H. Obloh, K. Kohler, and M. Maier. Hole conductivity and compensation in epitaxial gan:mg layers. *Phys. Rev. B*, 62:10867–10872, Oct 2000.

[126] L. T. Romano, M. Kneissl, J. E. Northrup, C. G. Van de Walle, and D. W. Treat. Influence of microstructure on the carrier concentration of mg-doped gan films. *Applied Physics Letters*, 79(17):2734–2736, 2001.

[127] *Nathaniel Reed Miller, Electrical and Electrothermal Transport Properties of n- and p-type InN.* PhD thesis, University of California, BERKELEY, 2010.

[128] L. J. Van der Pauw. A method of measuring specific resistivity and hall effect of discs of arbitrary shape. *Philips Res. Repts.*, 13(4):1–9, jul 1958.

[129] R. E. Jones, K. M. Yu, S. X. Li, W. Walukiewicz, J. W. Ager, E. E. Haller, H. Lu, and W. J. Schaff. Evidence for p-type doping of inn. *Phys. Rev. Lett.*, 96:125505, Mar 2006.

[130] X. Wang, S. B. Che, Y. Ishitani, and A. Yoshikawa. Hole mobility in mg-doped p-type inn films. *Applied Physics Letters*, 92(13):132108, 2008.

[131] Y. C. Yeo, T. C. Chong, and M. F. Li. Electronic band structures and effective-mass parameters of wurtzite gan and inn. *Journal of Applied Physics*, 83(3):1429–1436, 1998.

[132] Laytec instruments.

[133] H. F. Liu, W. Liu, A. M. Yong, X. H. Zhang, S. J. Chua, and D. Z. Chi. Effects of annealing on structural and optical properties of ingan/gan multiple quantum wells at emission wavelength of 490 nm. *Journal of Applied Physics*, 110(6):063505, 2011.

[134] B. Hollander, H. Heer, M. Wagener, H. Halling, and S. Mantl. New high-precision 5-axes rbs/channeling goniometer for ion beam ers. *Nuclear Instruments and Methods in Physics Research Section B: Beam Interactions with Materials and Atoms*, 161-163(0):227 – 230, 2000.

[135] S. T. Picraux, L. R. Dawson, J. Y. Tsao, B. L. Doyle, and S. R. Lee. Structure of layered crystals studied by high energy ion beams. *Nuclear Instruments and Methods in Physics Research Section B: Beam Interactions with Materials and Atoms*, 33(1-4):891 – 897, 1988.

[136] F. Tuomisto. Vacancy defects in iii-nitrides: what does positron annihilation spectroscopy reveal? *Journal of Physics: Conference Series*, 265(1):012003, 2011.

[137] *Christian Rauch, Defect studies in n-type indium nitride.* PhD thesis, Aalto University, 2012.

[138] P. Asoka-Kumar and K. G. Lynn. Applications of positron annihilation spectroscopy. *J. Phys. IV France*, 05:C1–15–C1–25, 1995.

[139] R. Krause-Rehberg, Martin-Luther-University Halle-Wittenberg, Germany, (ppt).

[140] I. Prochazka. Stress and its effect on optical properties of gan epilayers grown on si(111), 6h-sic(0001), and c-plane sapphire. *Materials Structure*, 8(2):55–58, jul 2001.

[141] A. Vehanen, K. Saarinen, P. Hautojärvi, and H. Huomo. Profiling multilayer structures with monoenergetic positrons. *Phys. Rev. B*, 35:4606–4610, Apr 1987.

[142] C. Rauch, Ö. Tuna, C. Giesen, M. Heuken, and F. Tuomisto. Point defect evolution in low-temperature mocvd growth of inn. *physica status solidi (a)*, 209(1):87–90, 2012.

[143] Y. Sun, X. M. Shen, J. Wang, D. G. Zhao, G. Feng, Y. Fu, S. M. Zhang, Z. H. Zhang, Z. H. Feng, Y. X. Bai, and H. Yang. Thermal annealing behaviour of ni/au on n-gan schottky contacts. *Journal of Physics D: Applied Physics*, 35(20):2648, 2002.

[144] J. Xie, S. Mia, R. Dalmau, R. Collazo, A. Rice, J. Tweedie, and Z. Sitar. Ni/au schottky diodes on alxga1-xn (0.7<x<1) grown on aln single crystal substrates. *physica status solidi (c)*, 8(7-8):2407–2409, 2011.

[145] P. Blood. Capacitance-voltage profiling and the characterisation of iii-v semiconductors using electrolyte barriers. *Semiconductor Science and Technology*, 1(1):7, 1986.

[146] Wafer Profiler CVP21 equipment.

[147] G. Gouy. Electronic band structures and effective-mass parameters of wurtzite gan and inn. *J. Phys. Theor. Appl.*, 9(3):457Ű–468, 1910.

[148] O. Z. Stern. Electronic band structures and effective-mass parameters of wurtzite gan and inn. *Elektrochem. Angew. Phys. Chem.*, 30(3):508Ű516, 1924.

[149] H. Helmholtz. Electronic band structures and effective-mass parameters of wurtzite gan and inn. *Ann. Phys.*, 243(3):337Ű382, 1879.

[150] H. Harima. Properties of gan and related compounds studied by means of raman scattering. *Journal of Physics: Condensed Matter*, 14(38):R967, 2002.

[151] M. Kuball. Electronic band structures and effective-mass parameters of wurtzite gan and inn. *Surf. Interface Anal.*, 31(3):987, 2001.

[152] O. Briot, B. Gil, B. Maleyre, S. Ruffenach, C. Pinquier, F. Demangeot, and J. Frandon. Strain-induced correlations between the phonon frequencies of indium nitride. *physica status solidi (c)*, 1(6):1420–1424, 2004.

[153] Ö. Tuna, Jpn. Journal. Apply. Phys. submitted, 2012.

[154] G. Irmer, V. V. Toporov, B. H. Bairamov, and J. Monecke. Determination of the charge carrier concentration and mobility in n-gap by raman spectroscopy. *physica status solidi (b)*, 119(2):595–603, 1983.

[155] H. Harima, H. Sakashita, and S. Nakashima. Properties of gan and related compounds studied by means of raman scattering. *Material Science Forum*, 264-268(38):1363–1366, 1998.

[156] B. B. Varga. Coupling of plasmons to polar phonons in degenerate semiconductors. *Phys. Rev.*, 137:A1896–A1902, Mar 1965.

[157] S. R. Lee, A. M. West, A. A. Allerman, K. E. Waldrip, D. M. Follstaedt, P. P. Provencio, D. D. Koleske, and C. R. Abernathy. Effect of threading dislocations on the bragg peakwidths of gan, algan, and aln heterolayers. *Applied Physics Letters*, 86(24):241904, 2005.

[158] S. Keller, B. P. Keller, Y. F. Wu, B. Heying, D. Kapolnek, J. S. Speck, U. K. Mishra, and S. P. DenBaars. Influence of sapphire nitridation on properties of gallium nitride grown by metalorganic chemical vapor deposition. *Applied Physics Letters*, 68(11):1525–1527, 1996.

[159] N. Grandjean, J. Massies, and M. Leroux. Nitridation of sapphire. effect on the optical properties of gan epitaxial overlayers. *Applied Physics Letters*, 69(14):2071–2073, 1996.

[160] T. Lang, M. Odnoblyudov, V. Bougrov, and M. Sopanen. Mocvd growth of gan islands by multistep nucleation layer technique. *Journal of Crystal Growth*, 277:64 – 71, 2005.

[161] D. D. Koleske, M. E. Coltrin, S. R. Lee, G. Thaler, K. C. Cross, and M. J. Russell. Understanding gan nucleation layer evolution on sapphire and its impact on gan dislocation density. pages 68410H–68410H–12, 2007.

[162] X. H. Wu, P. Fini, E. J. Tarsa, B. Heying, S. Keller, U. K. Mishra, S. P. DenBaars, and J. S. Speck. Dislocation generation in gan heteroepitaxy. *Journal of Crystal Growth*, 189-190(0):231 – 243, 1998.

[163] M. Jamil, H. Zhao, J. B. Higgins, and N. Tansu. Influence of growth temperature

and v/ii grown on gan/sapphire using pulsed movpe. *Journal of Crystal Growth*, 310(23):4947 – 4953, 2008.

[164] I. N. Stranski and L. Krastanow. Mathematisch-naturwissenschaftlichen klasse iib. *Akademie der Wissenschaften Wien*, (146), 1938.

[165] A. Jain, X. Weng, S. Raghavan, B. L. VanMil, T. Myers, and J. M. Redwing. Effect of polarity on the growth of inn films by metalorganic chemical vapor deposition. *Journal of Applied Physics*, 104(5):053112, 2008.

[166] S. A. Kukushkin, A. V. Osipov, V. N. Bessolov, B. K. Medvedev, V. K. Nevolin, and K. A. Tcarik. Substrates for epitaxy of gallium nemical vapor deposition. *Rev.Adv.Mater.Sci.*, 17:1–32, 2008.

[167] R. People and J. C. Bean. Calculation of critical layer thickness versus lattice mismatch for ge[sub x]si[sub 1 - x]/si strained-layer heterostructures. *Applied Physics Letters*, 47(3):322–324, 1985.

[168] S. Srinivasan, L. Geng, R. Liu, F. A. Ponce, Y. Narukawa, and S. Tanaka. Slip systems and misfit dislocations in ingan epilayers. *Applied Physics Letters*, 83(25):5187–5189, 2003.

[169] S. J. Hearne, J. Han, S. R. Lee, J. A. Floro, D. M. Follstaedt, E. Chason, and I. S. T. Tsong. Brittle-ductile relaxation kinetics of strained algan/gan heterostructures. *Applied Physics Letters*, 76(12):1534–1536, 2000.

[170] M. Perez Caro, A. G. Rodriguez, E. Löpez-Luna, M. A. Vidal, and H. Navarro-Contreras. Critical thickness of beta-inn/gan/mgo structures. *Journal of Applied Physics*, 107(8):083510, 2010.

[171] P. Gibart. Metal organic vapour phase epitaxy of gan and lateral overgrowth. *Reports on Progress in Physics*, 67(5):667, 2004.

[172] D. C. Look and J. R. Sizelove. Dislocation scattering in gan. *Phys. Rev. Lett.*, 82:1237–1240, Feb 1999.

[173] A. Krtschil, A. Dadgar, and A. Krost. Decoration effects as origin of dislocation-related charges in gallium nitride layers investigated by scanning surface potential microscopy. *Applied Physics Letters*, 82(14):2263–2265, 2003.

[174] D. Cherns, C. G. Jiao, H. Mokhtari, J. Cai, and F.A. Ponce. Electron holography studies of the charge on dislocations in gan. *physica status solidi (b)*, 234(3):924–930, 2002.

[175] J. Cai and F.A. Ponce. Determination by electron holography of the electronic charge distribution at threading dislocations in epitaxial gan. *physica status solidi (a)*, 192(2):407–411, 2002.

[176] *Abhishek Jain, MOCVD Growth and Study of Thin Films of Indium Nitrides.* PhD thesis, Pennsylvania State University, 2006.

[177] S. Ruffenach, M. Moret, O. Briot, and B. Gil. Ammonia: A source of hydrogen dopant for inn layers grown by metal organic vapor phase epitaxy. *Applied Physics Letters*, 95(4):042102, 2009.

[178] A. Yamamoto, K. I. Sugita, and A. Hashimoto. Elucidation of factors obstructing quality improvement of movpe-grown inn. *Journal of Crystal Growth*, 311(22):4636 – 4640, 2009.

[179] K. S. A. Butcher, A. J. Fernandes, P. P. T. Chen, M. Wintrebert-Fouquet, H. Timmers, S. K. Shrestha, H. Hirshy, R. M. Perks, and Brian F. Usher. The nature of nitrogen related point defects in common forms of inn. *Journal of Applied Physics*, 101(12):123702, 2007.

[180] V. Darakchieva, M. Y. Xie, D. Rogalla, H. W. Beckerand K. Lorenz, E. Alves, S. Ruffenach, M. Moret, and O. Briot. Free electron properties and hydrogen in inn grown by movpe. *physica status solidi (a)*, 208(5):1179–1182, 2011.

[181] C. Rauch, I. Makkonen, and F. Tuomisto. Identifying vacancy complexes in compound semiconductors with positron annihilation spectroscopy: A case study of inn. *Phys. Rev. B*, 84:125201, Sep 2011.

[182] A. Uedono, C. Shaoqiang, S. Jongwon, K. Ito, H. Nakamori, N. Honda, S. Tomita, K. Akimoto, H. Kudo, and S. Ishibashi. Vacancy-type defects in er-doped gan studied by a monoenergetic positron beam. *Journal of Applied Physics*, 103(10):104505, 2008.

[183] A. Uedono, K. Ito, H. Nakamori, K. Mori, Y. Nakano, T. Kachi, S. Ishibashi, T. Ohdaira, and R. Suzuki. Annealing properties of vacancy-type defects in ion-implanted gan studied by monoenergetic positron beams. *Journal of Applied Physics*, 102(8):084505, 2007.

[184] A. Uedono, H. Nakamori, K. Narita, J. Suzuki, X. Wang, S. B. Che, Y. Ishitani, A. Yoshikawa, and S. Ishibashi. Vacancy-type defects in mg-doped inn probed by means of positron annihilation. *Journal of Applied Physics*, 105(5):054507, 2009.

[185] C. Chang, S. Chuan-Feng, C. Nai-Chuan, C. Pen-Hsiu, and L. Kuo-Shiun. High mobility inn films grown by metal-organic vapor phase epitaxy. *physica status solidi (c)*, 1(10):2559–2563, 2004.

[186] F. Chen, A. N. Cartwright, H. Lu, and W. J. Schaff. Temperature dependence of carrier lifetimes in inn. *physica status solidi (a)*, 202(5):768–772, 2005.

[187] D. P. Norman, L. W. Tu, S. Y. Chiang, P. H. Tseng, P. Wadekar, S. Hamad, and H. W. Seo. Effect of temperature and v/iii ratio on the initial growth of indium nitride using plasma-assisted metal-organic chemical vapor deposition. *Journal of Applied Physics*, 109(6):063517, 2011.

[188] H. Wang, D. S. Jiang, J. J. Zhu, D. G. Zhao, Z. S. Liu, Y. T. Wang, S. M. Zhang, and H. Yang. The influence of growth temperature and input v/iii ratio on the initial nucleation and material properties of inn on gan by mocvd. *Semiconductor Science and Technology*, 24(5):055001, 2009.

[189] R. Kirste, M. R. Wagner, J. H. Schulze, A. Strittmatter, R. C. S. Zlatko, M. Alevli, N. Dietz, and A. Hoffmann. Optical properties of inn grown on templates with controlled surface polarities. *physica status solidi (a)*, 207(10):2351–2354, 2010.

[190] Ö. Tuna, W.M. Linhart, E.V. Lutsenko, M.V. Rzheutski, G.P. Yablonskii, T.D. Veal, C.F. McConville, C. Giesen, H. Kalisch, A. Vescan, and M. Heuken. Structural, electrical and optical characterization of mocvd grown in-rich ingan layers. *Journal of Crystal Growth*, 358(0):51 – 56, 2012.

[191] M. Moret, S. Ruffenach, O. Briot, and B. Gil. The determination of the bulk residual doping in indium nitride films using photoluminescence. *Applied Physics Letters*, 95(3):031910, 2009.

[192] P. Perlin, J. Camassel, W. Knap, T. Taliercio, J. C. Chervin, T. Suski, I. Grzegory, and S. Porowski. Investigation of longitudinal-optical phonon-plasmon coupled modes in highly conducting bulk gan. *Applied Physics Letters*, 67(17):2524–2526, 1995.

[193] R. Cusco, N. Domenech-Amador, L. Artus, T. Gotschke, K. Jeganathan, T. Stoica, and R. Calarco. Probing the electron density in undoped, si-doped, and mg-doped inn nanowires by means of raman scattering. *Applied Physics Letters*, 97(22):221906, 2010.

[194] J. H. Chen, Z. C. Feng, J. C. Wang, H. L. Tsai, J. R. Yang, A. Parekh, E. Armour, and P. Faniano. Study of carrier localization in ingan/gan quantum well blue-light-emitting diode structures. *Journal of Crystal Growth*, 287(2):354 – 358, 2006.

[195] T. Matsuoka, N. Yoshimoto, T. Sasaki, and A. Katsui. Wide-gap semiconductor ingan and ingaaln grown by movpe. *J. Electron. Mater.*, 21(2):157–163, February 1992.

[196] Ö. Tuna, H. Behmenburg, C. Giesen, H. Kalisch, R. H. Jansen, G. P. Yablonskii, and M. Heuken. Dependence of inn properties on mocvd growth parameters. *physica status solidi (c)*, 8(7-8):2044–2046, 2011.

[197] T. Mukai, M. Yamada, and S. Nakamura. Characteristics of ingan-based uv/blue/green/amber/red light-emitting diodes. *Japanese Journal of Applied Physics*, 38(Part 1, No. 7A):3976–3981, 1999.

[198] V. Y. Davydov, A. A. Klochikhin, V. V. Emtsev, S. V. Ivanovand V. V. Vekshin, F. Bechstedt, J. Furthmüller, H. Harima, A. V. Mudryi, A. Hashimoto, A. Yamamoto, J. Aderhold, J. Graul, and E. E. Haller. Band gap of inn and in-rich inxga1Ůxn alloys ($0.36 < x < 1$). *physica status solidi (b)*, 230(2):R4–R6, 2002.

[199] O. Jani, I. Ferguson, C. Honsberg, and S. Kurtz. Design and characterization of gan/ingan solar cells. *Applied Physics Letters*, 91(13):132117, 2007.

[200] J. W. Ju, E. S. Kang, H. S. Kim, L. W. Jang, H.-K. Ahn, J. W. Jeon, I. H. Leea, and J. H. Baek. Metal-organic chemical vapor deposition growth of ingan/gan high power green light emitting diode: Effects of ingan well protection and electron reservoir layer. *Journal of Applied Physics*, 102(5):053519, 2007.

[201] *Neelam Khan, Optical, Structural, and Transport Propertoes of InN, InGaN Alloys Grown by Metalorganic Chemical Vapor Deposition.* PhD thesis, Kansas State University, 2009.

[202] E. Trybus, O. Jani, S. Burnham, I. Ferguson, C. Honsbergand M. Steiner, and W. A. Doolittle. Characteristics of ingan designed for photovoltaic applications. *physica status solidi (c)*, 5(6):1843–1845, 2008.

[203] F. K. Yam and Z. Hassan. Ingan: An overview of the growth kinetics, physical properties and emission mechanisms. *Superlattices and Microstructures*, 43(1):1 – 23, 2008.

[204] P. D. C. King, T. D. Veal, P. H. Jefferson, C. F. McConvilleand Hai Lu, and W. J. Schaff. Variation of band bending at the surface of mg-doped ingan: Evidence of p-type conductivity across the composition range. *Phys. Rev. B*, 75:115312, Mar 2007.

[205] N. A. El-Masry, E. L. Piner, S. X. Liu, and S. M. Bedair. Phase separation in ingan grown by metalorganic chemical vapor deposition. *Applied Physics Letters*, 72(1):40–42, 1998.

[206] B. Liu, R. Zhang, J. G. Zheng, X. L. Ji, D. Y. Fu, Z. L. Xie, D. J. Chen, P. Chen, R. L. Jiang, and Y. D. Zheng. Composition pulling effect and strain relief mechanism in algan/aln distributed bragg reflectors. *Applied Physics Letters*, 98(26):261916, 2011.

[207] C. Chang, C. Shih, N. Chen, T. Y. Lin, and L. Kuo-Shiun. In-rich in[sub 1 - x]ga[sub x]n films by metalorganic vapor phase epitaxy. *Applied Physics Letters*, 85(25):6131–6133, 2004.

[208] L. R. Bailey, T. D. Veal, P. D. C. King, C. F. McConville, J. Pereiro, J. Grandal, M. A. Sánchez-García, E. Mu noz, and E. Calleja. Band bending at the surfaces of in-rich ingan alloys. *Journal of Applied Physics*, 104(11):113716, 2008.

[209] P. D. C. King, T. D. Veal, and C. F. McConville. Nonparabolic coupled poisson-schrödinger solutions for quantized electron accumulation layers: Band bending, charge profile, and subbands at inn surfaces. *Phys. Rev. B*, 77:125305, Mar 2008.

[210] H. Übensee, G. Paasch, and J.-P. Zöllner. Modified thomas-fermi theory for depletion and accumulation layers in n -type gaas. *Phys. Rev. B*, 39:1955–1957, Jan 1989.

[211] T. D. Veal, L. F. J. Piper, M. R. Phillips, M.H. Zareie, H. Lu, W. J. Schaff, and C. F. McConville. Doping-dependence of subband energies in quantized electron accumulation at inn surfaces. *physica status solidi (a)*, 204(2):536–542, 2007.

[212] A. Yang, Y. Yamashita, T. Yamaguchi, M. Imura, M. Kaneko, O. Sakata, Y. Nanishi, and K. Kobayashi. Strong correlation between oxygen donor and near-surface electron accumulation in undoped and mg-doped in-polar inn films. *Applied Physics Express*, 5(3):031002, 2012.

[213] P. D. C. King, T. D. Veal, A. Adikimenakis, H. Lu, L. R. Bailey, E. Iliopoulos, A. Georgakilas, W. J. Schaff, and C. F. McConville. Surface electronic properties of undoped inaln alloys. *Applied Physics Letters*, 92(17):172105, 2008.

[214] T. D. Veal, P. H. Jefferson, L. F. J. Piper, C. F. McConville, T. B. Joyce, P. R. Chalker, L. Considine, H. Lu, and W. J. Schaff. Transition from electron accumulation to depletion at ingan surfaces. *Applied Physics Letters*, 89(20):202110, 2006.

[215] W. M. Linhart, T. D. Veal, P. D. C. King, G. Koblmüller, C. S. Gallinat, J. S. Speck, and C. F. McConville. Surface, bulk, and interface electronic properties of nonpolar inn. *Applied Physics Letters*, 97(11):112103, 2010.

[216] W. M. Linhart, Ö. Tuna, T. D. Veal, J. J. Mudd, C. Giesenand M. Heuken, and C. F. McConville. Surface electronic properties of in-rich ingan alloys grown by mocvd. *physica status solidi (c)*, 9(3-4):662–665, 2012.

[217] T. Chung, J. B. Limb, U. Chowdhury, P. Li, J. H. Ryou, D. Yoo, D. Zakharov, Z. Liliental-Weber, and R. D. Dupuis. Mocvd growth of ingan:mg for gan/ingan hbts. *physica status solidi (c)*, 2(7):2157–2160, 2005.

[218] K. Sasamoto, T. Hotta, K. Sugita, A.G. Bhuiyan, A. Hashimoto, A. Yamamoto, K. Kinoshita, and Y. Kohji. Movpe growth of high quality p-type ingan with intermediate in compositions. *Journal of Crystal Growth*, 318(1):492 – 495, 2011.

[219] J. P. Liu, J. B. Limb, J. H. Ryou, W. Lee, D. Yoo, C. A. Horne, and R. D. Dupuis. Characteristics of Green Light-Emitting Diodes Using an InGaN:Mg/GaN:Mg Superlattice as p Type Hole Injection and Contact Layers. *Journal of Electronic Materials*, 37:558–563, 2008.

[220] M. D. McCluskey, L. T. Romano, B. S. Krusor, N. M. Johnson, T. Suski, and J. Jun. Interdiffusion of in and ga in ingan quantum wells. *Applied Physics Letters*, 73(9):1281–1283, 1998.

[221] C. C. Chuo, C. M. Lee, and J. I. Chyi. Interdiffusion of in and ga in ingan/gan multiple quantum wells. *Applied Physics Letters*, 78(3):314–316, 2001.

[222] J. Liu, J.-H. Ryou, Z. Lochner, J. Limb, D. Yoo, R. D. Dupuis, Z. Wu, A. M. Fischer, and F. A. Ponce. Surface morphology control of green leds with p-

ingan layers grown by metalorganic chemical vapor deposition. *Journal of Crystal Growth*, 310(23):5166 – 5169, 2008.

[223] R. Dahal, B. Pantha, J. Li, J. Y. Lin, and H. X. Jiang. Ingan/gan multiple quantum well solar cells with long operating wavelengths. *Applied Physics Letters*, 94(6):063505, 2009.

[224] K. Aryal, B. N. Pantha, J. Li, J. Y. Lin, and H. X. Jiang. Hydrogen generation by solar water splitting using p-ingan photoelectrochemical cells. *Applied Physics Letters*, 96(5):052110, 2010.

[225] W. Lee and J. Limb. Influence of growth temperature and growth rate of p-gan layers on the characteristics of green light emitting diodes. *Journal of Electronic Materials*, 35:587–591, 2006. 10.1007/s11664-006-0104-2.

[226] S. Pereira, M. R. Correia, E. Pereira, K. P. O'Donnell, E. Alves, A. D. Sequeira, N. Franco, I. M. Watson, and C. J. Deatcher. Strain and composition distributions in wurtzite ingan/gan layers extracted from x-ray reciprocal space mapping. *Applied Physics Letters*, 80(21):3913–3915, 2002.

[227] M. Schuster, P. O. Gervais, B. Jobst, W. Hösler, R. Averbeck, H. Riechert, A. Iberl, and R. Stömmer. Determination of the chemical composition of distorted ingan/gan heterostructures from x-ray diffraction data. *Journal of Physics D: Applied Physics*, 32(10A):A56, 1999.

[228] L. Sang, M. Takeguchi, W. Lee, Y. Nakayama, M. Lozac'h, T. Sekiguchi, and M. Sumiya. Phase separation resulting from mg doping in p-ingan film grown on gan/sapphire template. *Applied Physics Express*, 3(11):111004, 2010.

[229] I. H. Ho and G. B. Stringfellow. Effects of annealing on structural and optical properties of ingan/gan multiple quantum wells at emission wavelength of 490 nm. *Mater. Res. Soc. Symp. Proc.*, 449(6):871, 1997.

[230] Ingan: An overview of the growth kinetics, physical properties and emission mechanisms. *http://www.webelements.com/*.

[231] Q. Deng, X. Wang, H. Xiao, C. Wang, H. Yin, H. Chen, D. Lin, L. Jiang, C. Feng, J. Li, Z. Wang, and X. Hou. Comparison of as-grown and annealed gan/ingan:mg samples. *Journal of Physics D: Applied Physics*, 44(34):345101, 2011.

[232] T. H. Gfroerer. *Photoluminescence in Analysis of Surfaces and Interfaces*. John Wiley & Sons, Ltd, 2006.

[233] A. A. Klochikhin, V. Y. Davydov, V. V. Emtsev, A. V. Sakharov, V. A. Kapitonov, B. A. Andreev, H. Lu, and W. J. Schaff. Acceptor states in the photoluminescence spectra of n-InN. *Phys. Rev. B*, 71:195207, May 2005.

[234] X. Wang, S. B. Che, Y. Ishitani, and A. Yoshikawa. Growth and properties of mg-doped in-polar inn films. *Applied Physics Letters*, 90(20):201913, 2007.

[235] P. H. Lim, B. Schineller, O. Schon, K. Heime, and M. Heuken. Photoluminescence ofetalorganic vapor-phase epitaxy (movpe). *Journal of Crystal Growth*, 205(1-2):1 – 10, 1999.

[236] F. Chen, A. N. Cartwright, H. Lu, and W. J. Schaff. Time-resolved spectroscopy of recombination and relaxation dynamics in inn. *Applied Physics Letters*, 83(24):4984–4986, 2003.

[237] J. L. Lyons, A. Janotti, and C. G. Van de Walle. Carbon impurities and the yellow luminescence in gan. *Applied Physics Letters*, 97(15):152108, 2010.

[238] C. B. Soh, S. J. Chua, H. F. Lim, D. Z. Chi, S. Tripathy, and W. Liu. Assignment of deep levels causing yellow luminescence in gan. *Journal of Applied Physics*, 96(3):1341–1347, 2004.

[239] E. F. Schubert, I. D. Goepfert, and J. M. Redwing. Evidence of compensating centers as origin of yellow luminescence in gan. *Applied Physics Letters*, 71(22):3224–3226, 1997.

[240] H. M. Chen, Y. F. Chen, M. C. Lee, and M. S. Feng. Yellow luminescence in n-type gan epitaxial films. *Phys. Rev. B*, 56:6942–6946, Sep 1997.

[241] D. G. Chtchekine, G. D. Gilliland, Z. C. Feng, S. J. Chua, D. J. Wolford, S. E. Ralph, M. J. Schurman, and I. Ferguson. Temperature dependence of bound exciton emissions in gan. *MRS Online Proceedings Library*, 537, 1998.

[242] K. Kumakura, T. Makimoto, and N. Kobayashi. Mg-acceptor activation mechanism and transport characteristics in p-type ingan grown by metalorganic vapor phase epitaxy. *Journal of Applied Physics*, 93(6):3370–3375, 2003.

[243] C. Chang, T. Tang, P.-H. Chang, N.-C. Chen, and C. T. Liang. Magnesium doping of in-rich ingan. *Japanese Journal of Applied Physics*, 46(5A):2840–2843, 2007.

[244] B. N. Pantha, A. Sedhain, J. Li, J. Y. Lin, and H. X. Jiang. Electrical and optical properties of p-type ingan. *Applied Physics Letters*, 95(26):261904, 2009.

[245] L. Eckey, U. von Gfug, J. Holst, A. Hoffmann, A. Kaschner, H. Siegle, C. Thomsen, B. Schineller, K. Heime, M. Heuken, O. Schön, and R. Beccard. Photoluminescence and raman study of compensation effects in mg-doped gan epilayers. *Journal of Applied Physics*, 84(10):5828–5830, 1998.

[246] N. Khan, N. Nepal, A. Sedhain, J. Y. Lin, and H. X. Jiang. Mg acceptor level in inn epilayers probed by photoluminescence. *Applied Physics Letters*, 91(1):012101, 2007.

[247] J. W. Ager, R. E. Jones, D. M. Yamaguchi, K. M. Yu, W. Walukiewicz, S. X. Li, E. E. Haller, H. Lu, and W. J. Schaff. p-type inn and in-rich ingan. *physica status solidi (b)*, 244(6):1820–1824, 2007.

[248] *Phillip A. Anderson, Indium Nitride: An Investigation of Growth, Electronic Structure and Doping*. PhD thesis, University of Canterbury, 2006.

[249] P. A. Anderson, C. H. Swartz, D. Carder, R. J. Reeves, S. M. Durbin, S. Chandril, and T. H. Myers. Buried p-type layers in mg-doped inn. *Applied Physics Letters*, 89(18):184104, 2006.

[250] M. Higashiwaki and T. Matsui. Epitaxial growth of high-quality inn films on sapphire substrates by plasma-assisted molecular-beam epitaxy. *Journal of Crystal Growth*, 252(1-3):128 – 135, 2003.

[251] P. Singh, P. Ruterana, M. Morales, F. Goubilleau, M. Wojdak, J.F. Carlin, M. Ilegems, and D. Chateigner. Structural and optical characterisation of inn layers grown by mocvd. *Superlattices and Microstructures*, 36(4-6):537 – 545, 2004. <ce:title>European Materials Research Society 2004, Symposium L. InN, GaN, AlN and Related Materials, their Heterostructures and Devices.

Acknowledgements

Firstly, I would like to impress that this work was supported by the EU under the Grant agreement N^o: 213238, Initial training network RAINBOW of the 7 RTD Frameworks.
Special thanks to my scientific supervisor Professor Dr. Michael Heuken for accepting me as his Ph.D. student and for his encouragement and suggestions during this work.
I would acknowledge too many other people for their support, valuable discussions and help in brief by saying THANK YOU to:
Dr. Christoph Giesen for great help and discussions of the scientific results as well as correction of scientific manuscripts and this thesis.
Dr. Kai Christiansen for his trust and great help to come over the problems in the lab. and providing me any kind of opportunities to go further with my scientific research.
Dr. Holger Kalisch for numerous discussions and corrections of several manuscripts.
Prof. Dr. Andrei Vescan for scientific discussions during group meetings.
Researchers and technicians working at GaN device technology group for helping and gorgeous friendship.
Engineers working at AIXTRON SE for amazing time in the Laboratuary and for valuable scientific discussions.
Dr. Wolfgang Michael for material characterizations and discussions values experience about life.
Mrs. Gabriele Freund, Mrs. Brigitte Hampejs and Mrs. Birgit Brunne for their assistance for any kind of needs.
The group of Prof. Dr. G. P. Yablonskii at the National Science Academy of Belarus in Minsk for their persistent help with optical characterization and its interpretation.
The group of Prof. Dr. K. Jarasinas from the Institute of Materials Science and Applied Research in Vilnius for their differential transmission measurements and interpretation of the results.
The group of Prof. A. Hoffmann from the Technique University of Berlin Institute of Physics for Raman spectroscopy measurements and interpretations of the results.

The group of Prof. H. Morkoc from the Virginia Commonwealth University for optical characterizations and interpretations of the results.
All my colleagues from the RAINBOW project, Arantxa Vilalta-Clemente, Geeta Rani Mutta, Duc Van Dinh, Daria Skurid-ina, Tommaso Brazzini, Steven Albert, Albert Minj, Saurabh Pandey, Piero Gamarra, Simon Kraeusel, Naresh Gunasekar, Rui Yang, Egidijus Sakalauskas, Nils Kaufmann, Francesco Ivaldi and Christian Rauch for their nice collaborations and friendship.
Last but not least I would like to express a special thanks for my family for their support and encouragement.

List of publications

1. O. Tuna, H. Behmenburg, C. Giesen, H. Kalisch, R. H. Jansen, G. P. Yablonskii and M. Heuken. Phys. Stat. Sol. C. 8 (2011) 2044. Dependence of InN properties on MOCVD growth parameters.

2. O. Tuna, W. M. Linhart, E. V. Lutsenko, M. V. Rzheutski, T. D. Veal, C. F. McConville, A. Vescan, C. Giesen, H. Kalisch, G. P. Yablonskii and M. Heuken. Journal of Crystal Growth 358, 51 (2012) Structural, Electrical and Optical characterization of MOCVD grown In-rich InGaN Layers.

3. O. Tuna, H. Hahn, E. V. Lutsenko, M. V. Rzheutski, V. N. Pavlovskii, A. Vescan, C. Giesen, H. Kalisch, G. P. Yablonskii and M. Heuken. Journal of Crystal Growth 370, (2013) 2âĂŞ6 MOVPE Growth and Characterization of Thick Mg-Doped InGaN.

4. C. Rauch, O. Tuna, C. Giesen, M. Heuken and F. Tuomisto. Phys. Stat. Sol. A. 209 (2012) 87. Point defect evolution in low-temperature MOCVD growth of InN.

5. W. M. Linhart, O. Tuna, T. D. Veal, J. J. Mudd, C. Giesen, M. Heuken and C. F. McConville. Phys. Stat. Sol. C. 9 (2012) 662. Surface electronic properties of In-rich InGaN alloys grown by MOCVD.

6. E. Sakalauskas, O. Tuna, A. Kraus, H. Bremen, U. Rossow, C. Giesen, M. Heuken, A. Hangleiter and G. Gobsch, and R. Goldhahn. Phys. Stat. Sol. B. 249 (2012) 485. Dielectric function and bowing parameters of InGaN alloys.

7. C. Mauder, O. Tuna, B. Gutrath, V. Valmes, H. Behmenburg, M. V. Rzheutskii, E. V. Lutsenko, G. P. Yablonskii, M. Noyung, U. Simon, C. Giesen, M. Heuken, H. Kalisch and A. Vescan. Phys. Stat. Sol. C. 3 (2012) 964. Highly n-type doped InGaN Films for efficient direct solar Hydrogen Generation.

8. Kestutis Jarasiunas, Saulius Nargelas, Ramunas Aleksiejunas, Saulius

Miasojedovas, Mikas Vengris, Serdal Okur, Umit OzgÃijr, Hadis Morkoc, Christoph Giesen, Ocal Tuna, and Michael Heuken. J. Appl. Phys. 113, 103701 (2013); doi: 10.1063/1.4793637 Spectral distribution of excitation-dependent recombination rate in InGaN.